CANADIAN THESES ON MICROFICHE

THÈSES CANADIENNES SUR MICROFICHE

National Library of Canada
Collections Development Branch

Canadian Theses on
Microfiche Service

Ottawa, Canada
K1A 0N4

Bibliothèque nationale du Canada
Direction du développement des collections

Service des thèses canadiennes
sur microfiche

NOTICE

The quality of this microfiche is heavily dependent upon the quality of the original thesis submitted for microfilming. Every effort has been made to ensure the highest quality of reproduction possible.

If pages are missing, contact the university which granted the degree.

Some pages may have indistinct print especially if the original pages were typed with a poor typewriter ribbon or if the university sent us an inferior photocopy.

Previously copyrighted materials (journal articles, published tests, etc.) are not filmed.

Reproduction in full or in part of this film is governed by the Canadian Copyright Act, R.S.C. 1970, c. C-30. Please read the authorization forms which accompany this thesis.

AVIS

La qualité de cette microfiche dépend grandement de la qualité de la thèse soumise au microfilmage. Nous avons tout fait pour assurer une qualité supérieure de reproduction.

S'il manque des pages, veuillez communiquer avec l'université qui a conféré le grade.

La qualité d'impression de certaines pages peut laisser à désirer, surtout si les pages originales ont été dactylographiées à l'aide d'un ruban usé ou si l'université nous a fait parvenir une photocopie de qualité inférieure.

Les documents qui font déjà l'objet d'un droit d'auteur (articles de revue, examens publiés, etc.) ne sont pas microfilmés.

La reproduction, même partielle, de ce microfilm est soumise à la Loi canadienne sur le droit d'auteur, SRC 1970, c. C-30. Veuillez prendre connaissance des formules d'autorisation qui accompagnent cette thèse.

THIS DISSERTATION
HAS BEEN MICROFILMED
EXACTLY AS RECEIVED

LA THÈSE A ÉTÉ
MICROFILMÉE TELLE QUE
NOUS L'AVONS REÇUE

Canada

NL 339 (r. 85/09)

0-315-19494-4

National Library of Canada | Bibliothèque nationale du Canada

Canadian Theses Division | Division des thèses canadiennes

Ottawa, Canada
K1A 0N4

67402

PERMISSION TO MICROFILM — AUTORISATION DE MICROFILMER

• Please print or type — Écrire en lettres moulées ou dactylographier

Full Name of Author — Nom complet de l'auteur

JOSE THOMAS THEKKUMTHALA

Date of Birth — Date de naissance	Country of Birth — Lieu de naissance
26-01-51	INDIA

Permanent Address — Résidence fixe

PHYSICS DEPT., UNIV. OF ALBERTA, EDMONTON, ALBERTA, CANADA
T6G 2J1

Title of Thesis — Titre de la thèse

AN EXPERIMENTAL STUDY OF THE REACTION $pT \rightarrow d\gamma$
AT INTERMEDIATE ENERGIES

University — Université

UNIVERSITY OF ALBERTA

Degree for which thesis was presented — Grade pour lequel cette thèse fut présentée

Ph. D.

Year this degree conferred — Année d'obtention de ce grade	Name of Supervisor — Nom du directeur de thèse
1984	Dr. J.M. CAMERON

Permission is hereby granted to the NATIONAL LIBRARY OF CANADA to microfilm this thesis and to lend or sell copies of the film.

The author reserves other publication rights, and neither the thesis nor extensive extracts from it may be printed or otherwise reproduced without the author's written permission.

L'autorisation est, par la présente, accordée à la BIBLIOTHÈQUE NATIONALE DU CANADA de microfilmer cette thèse et de prêter ou de vendre des exemplaires du film.

L'auteur se réserve les autres droits de publication; ni la thèse ni de longs extraits de celle-ci ne doivent être imprimés ou autrement reproduits sans l'autorisation écrite de l'auteur.

Date	Signature
~~12-10-84~~ 12-10-84	(Jose Thekkumthala)

NL-91 (4/77)

THE UNIVERSITY OF ALBERTA

AN EXPERIMENTAL STUDY OF THE REACTION PT → αγ AT INTERMEDIATE ENERGIES

by

© JOSE THOMAS THEKKUMTHALA

A THESIS

SUBMITTED TO THE FACULTY OF GRADUATE STUDIES AND RESEARCH

IN PARTIAL FULFILMENT OF THE REQUIREMENTS FOR THE DEGREE

OF DOCTOR OF PHILOSOPHY

in

NUCLEAR PHYSICS

DEPARTMENT OF PHYSICS

EDMONTON, ALBERTA

FALL, 1984

THE UNIVERISITY OF ALBERTA

RELEASE FORM

NAME OF AUTHOR: JOSE THOMAS THEKKUMTHALA

TITLE OF THESIS: AN EXPERIMENTAL STUDY OF THE REACTION PT + $\alpha\gamma$ AT INTERMEDIATE ENERGIES.

DEGREE FOR WHICH THESIS WAS PRESENTED: DOCTOR OF PHILOSOPHY

YEAR THIS DEGREE GRANTED: 1984

Permission is hereby granted to THE UNIVERSITY OF ALBERTA LIBRARY to reproduce single copies of this thesis and to lend or sell such copies for private, scholarly or scientific research purposes only.

The author reserves other publication rights, and neither the thesis nor extensive extracts from it may be printed or otherwise reproduced without the author's written permission.

(Signed) (Jose Thekkumthala)

PERMANENT ADDRESS:

NUCLEAR RESEARCH CENTRE

UNIVERSITY OF ALBERTA

EDMONTON, ALBERTA T6G 2N5

DATED 10 October 1984

THE UNIVERSITY OF ALBERTA

FACULTY OF GRADUATE STUDIES AND RESEARCH

The undersigned certify that they have read, and recommend to the Faculty of Graduate Studies and Research, for acceptance, a thesis entitled "AN EXPERIMENTAL STUDY OF THE REACTION PT + $\alpha\gamma$ AT INTERMEDIATE ENERGIES" submitted by JOSE THOMAS THEKKUMTHALA in partial fulfilment of the requirements for the degree of Doctor of Philosophy in Nuclear Physics.

John M. Cameron
Supervisor

.....

.....

P. Kitching

D.G. Hughes

W.E. Dawson
External Examiner

DATE 24th September, 1984

ABSTRACT

The experimental study of the radiative capture of protons by tritium was performed at proton energies of 227 MeV, 300 MeV and 375 MeV. A polarized beam was used and measurements were done at a number of angles. The cross section and the analyzing power of the reaction were obtained.

The study of the reaction beyond meson production threshold enabled the Meson Exchange effects to be seen explicitly. These ME effects are implicitly included in the low energy region through electric dipole operators by means of the Siegert's Theorem. First order correction through Gauge invariance gives rise to the seagull term which shows up as a $NN\pi\gamma$ four-point vertex term. The other factors contributing to the cross-section are the $\Delta(1232)$ and short-range correlations generating from the high momentum transfer characteristic of the (p,γ) process.

Phenomenological models like the Distorted Wave Impulse Approximation (DWIA) are quite successful in describing the (p,γ) process. DWIA is an extension of the Quasideuteron model introduced by Levinger. The interaction vertex is replaced by the experimentally known cross section of $p+n \rightarrow d\gamma$. The additional factors coming into the expression for the cross section are a form factor which is the fourier transform of the overlap of the wavefunctions with respect to the momentum transfer, a spin factor and a kinematical factor.

Another equally important motivation in studying the reaction was to check the validity of the Time Reversal Invariance (TRI) in the electromagnetic interaction of the hadrons. The principle of detailed balance relates the cross section for the forward reaction to that of the inverse reaction on the assumption of TRI. Comparison of the cross section values obtained in the present experiment with the inverse reaction data provided a check for the validity of TRI.

Comparison of the results with the theoretical predictions by Gari and Heback revealed the significance of the $\Delta(1232)$ contribution. The DWIA calculation agrees with the results very well except at high energies and backward angles. This points towards the multi-step processes which become important at high energies and backward angles. Comparison of the data with the inverse reaction data reveals very good agreement between them, both in the magnitude of the cross sections and the shape of the angular distributions, confirming the validity of TRI in the electromagnetic interaction of the hadrons.

ACKNOWLEDGEMENTS

I wish to express my thanks to Dr. J.M. Cameron for being a very fine supervisor. His commendable guidance through all phases of this work is gratefully acknowledged. My tribute to his patience and understanding. The financial assistance received from his research grant is also gratefully acknowledged.

I would also like to thank Dr. P. Kitching, my acting supervisor, and Dr. H.S. Sherif, my adviser for the initial period of my graduate program. My thanks go to all members of my supervisory committee.

Let me take this opportunity to thank all members of the Experiment 131 group, including the technical staff.

I would like to express my gratitude to Dr. H.W. Fearing for illuminating me on various theoretical aspects of this thesis project. I also thank him for letting me use his DWIA code.

A wide range of theoretical discussions with Dr. Tim Cooper during his short stay this summer were quite useful. My thanks go to Tim.

The availability of the VAX-11/780 for data analysis was extremely helpful. I would like to thank Dr. P.W. Green for explaining all you wanted to know about VAX (but afraid to ask).

I would like to thank Jim Easton for various useful discussions on programming and his help with plotting. I also wish to thank Jim Pasos for help with programming and plotting.

The financial assistance received in the form of the University of Alberta Graduate Research Assistantship and Teaching Assistantship is gratefully acknowledged. The financial assistance received from TRIUMF and UBC is also gratefully acknowledged.

Finally, I would like to thank Ms. Maureen Lavoie for typing this thesis with speed and efficiency. Thanks also go to Ms. Llanca Letelier for taking care of the equations. Their combined effort to meet the dealine was commendable. Thanks again!

October, 1984.

TABLE OF CONTENTS

CHAPTER		PAGE
1.	INTRODUCTION	1
	1.1 The Significance of the Reaction	1
	1.2 Variation of Photodisintegration Cross Section as a Function of Energy	2
	1.3 Meson Exchange Theories	7
	1.4 Quasideuteron and Other Phenomenological Models	21
	1.5 Testing the Time Reversal Invariance	27
2.	THE EXPERIMENT	34
	2.1 The Cyclotron	34
	2.2 Preparatory Calculation	34
	2.3 The Experimental Set-Up	36
	2.4 The Scattering Chamber	39
	2.5 The Target	40
	2.6 The Helium Bag	41
	2.7 The δ-Ray Magnet	41
	2.8 The Polarimeter	41
	2.9 The Detectors	47
	2.9.1 Counter Telescope	47
	2.9.2 Multi-Wire Proportional Chamber	48
	2.9.3 The Veto Detector	49
	2.9.4 The Cherenkov Counter	49
	2.10 The Electronics	52
	2.11 The Camac	65

3. THE DATA ANALYSIS.....73

3.1 The Data Acquisition.....73

3.2 The Data Event Structure.....73

3.3 The Data Re-Organization.....76

3.4 Various Stages of Data Analysis.....79

3.4.1 Recoil Angle Calculation.....79

3.4.2 Combining E and E.....83

3.4.3 Identification of (p,γ) Events.....87

3.5 The Cross Section Evaluation.....112

3.5.1 The (p,γ) Events.....112

3.5.2 The Total Beam Current.....118

3.5.3 The Target Thickness.....118

3.5.4 The Solid Angle.....118

3.5.5 The Wire Chamber Efficiency 119

3.5.6 The Cherenkov Counter Efficiency.....119

3.5.7 The System Live-Time.....119

3.5.8 The 'TI' Run Parameters.....120

3.5.9 Extraction of Events Due to Tritium and Cross Section Calculations.....121

3.6 The Statistical Uncertanty in the Cross Section Values.....121

3.7 The Analyzing Power Evaluation.....122

4. RESULTS AND CONCLUSIONS.....124

4.1 Experimental Results.....124

4.2 Distorted Wave Impulse Approximation (DWIA).....139

4.3 Salient Features of Fearing's DWIA Model.....142

4.4 The Wavefunctions for d, t and α.....145

4.5 Data for the Reaction p+n → d+γ.....147

4.6 $|M|^2$ Versus t Representation of the Result.....151

4.7 Conclusions.....154

REFERENCES.....163

APPENDIX A. TARGET THICKNESS EVALUATION THROUGH P-T ELASTIC SCATTERING EXPERIMENT.....166

A.1 The Medium Resolution Spectrometer.....166

A.2 The Experimental Procedure.....167

A.3 The Momentum Analysis.....170

A.4 The Target Thickness Evaluation.....170

A.4.1 The Solid Angle.....170

A.4.2 The Wire-Chamber Efficiency.....182

A.4.3 The System Live-Time.....182

A.4.4 Beam Current.....183

A.5 Correction for the Radioactive Decay.....184

APPENDIX B. δ-RAYS.....186

B.1 The Energy of the δ-Rays.....186

B.2 δ-Ray Production Probability.....189

APPENDIX C. CHERENKOV COUNTER CALIBRATION AND EFFICIENCY DETERMINATION.....192

C.1 M20 Stopped π/μ Channel.....192

C.2 The Experimental Details.....195

C.3 The Results.....196

C.4 Monte-Carlo Calculation for Photon Detection Efficiency.....197

APPENDIX D. STUDY OF THE REACTION $p+d \rightarrow {}^3He+\gamma$.....206

D.1 The Experimental Set-Up.....206

D.2 The Data Analysis.....207

D.3 The Results.....207

LIST OF TABLES

Table		Page
3.1	Scalers	74
3.2	The Event Structure	75
3.3	DCR Bit Pattern	77
3.4	Rewritten Event Structure	82
3.5a	Off-Line Analysis Output -- Polarimeter Counts	115
3.5b	Off-Line Analysis Output -- MWPC and Pulser Information	116
3.5c	Off-Line Analysis Output -- (p,γ) Events	117
4.1	Experimental Results for Cross Section and the Analyzing Power	125
4.2	Cross Section Values Converted Using Detailed Balance	126
4.3	Coefficients of the Polynomial	152
4.4	"C" Parameters of Equations 4.17-4.20	153
A.1	PT Elastic Scattering Data Summary	171
A.2	The Tritium Content in the Target	185
C.1	Photon Detection Efficiency of Lead-Glass Cherenkov Counter	203
D.1	$p+d \rightarrow {}^3He+\gamma$ Data Summary; (p,γ) Events	210
D.2	Cross Section and Analyzing Power for the Reaction $p+d \rightarrow {}^3He+\gamma$ at T = 300 MeV	216

LIST OF FIGURES

Figure		Page
1.1a	One-Body Interaction Diagrams	17
1.1b	Meson Exchange Diagrams	17
1.2	Δ Isobar Diagram	18
1.3	Proton-Pole, Triton-Pole and N'(1470) Diagrams	22
1.4	Quasideuteron and Δ Isobar Diagrams	25
2.1	Target-Detector Assembly	38
2.2	Polarimeter Target-Detector Assembly	43
2.3	Polarimeter Electronics	46
2.4	Cherenkov Counter Assembly	51
2.5	Left Side Fast Electronics	54
2.6	Right Side Fast Electronics	56
2.7	Pre-Event Latch and MWPC Electronics	58
2.8	Pulser, Polarimeter, Left-Slow and Right-Slow Electronics	62
2.9	ADC Gate, TDC Start, Stop,ADC,TDC Clear, Master Gate Electronics	64
2.10	Crate No. 1	67
2.11	Crate No. 2	69
2.12	Crate No. 3	71
3.1	Recoil Angle Determination Geometry	81
3.2	Scatter-Plot of ΔE Plastic Pulse-Height Versus E Plastic Pulse-Height for Protons	85

3.3 (p, γ) Identification Flow-Chart.....89

3.4 ΔE Versus E Spectrum for Protons and Alphas.....92

3.5 ΔE Versus E Spectrum for Alphas.....94

3.6 Time-of-Flight Versus Energy Spectrum for Alphas....96

3.7 Pulse-Height Histogram of Cherenkov Counter for the Reals;Target:TiT.....98

3.8 Pulse-Height Histogram of Cherenkov Counter for the Accidentals;Target:TiT.....100

3.8a Pulse-Height Histogram of Cherenkov Counter for the Reals;Target:Ti.....103

3.8b Pulse-Height Histogram of Cherenkov Counter for the Accidentals;Target:Ti.....105

3.9 Pulse-Height Histogram of Cherenkov Counter for the Reals in the Reaction p+d → ^{3}He+γ.....107

3.10 Recoil Energy Versus Recoil Angle Spectrum.....109

3.11 Three-Dimensional Spectrum for the Recoil Energy Versus Recoil Angle.....111

3.12 Kinematics of pt → αγ and pt → απ°.....114

4.1 Angular Distribution of Cross Section at T_p = 300 MeV.....128

4.2 Comparison of Excitation Functions for Radiative Capture and its Inverse Reaction.....130

4.2a Comparison of Excitation Function at 60° C.M. with the DWIA Calculation.....132

4.2b Comparison of Excitation Function at 90° C.M. with the DWIA Calculation.....134

4.3 Analyzing Power Distribution for the Reaction p+t → α+γ at T_p = 300 MeV.....136

4.3a Comparison of Excitation Function at 60° C.M. with Gari and Hebach's Calculation.....138

4.4 Angular Distribution of Cross Section for γ+d → p+n at Various γ Energies.....150

4.5 $|M|^2$ Versus t Representation of the Result.....156

4.6 Comparison of Analyzing Powers for the Reactions $pn \to d\gamma$, $pd \to {}^3He\,\gamma$ and $pT \to \alpha\gamma$.....160

A.1 Energy Versus Angle Graphs for Proton Elastically Scattered from ^3H, Ti and Cu.....169

A.2 YO versus XFK Spectrum for Elastically Scattered Protons from Ti, Cu, C, ^3H and ^4H.....173

A.3 XFK Histogram for Elastically Scattered Protons at $\theta_p = 18.04$.....175

A.4 XFK Histogram for Elastically Scattered Protons at $\theta_p = 22.01$.....177

A.5 XFK Histogram for Elastically Scattered Protons at $\theta_p = 25.99$.....179

A.6 XFK Spectrum for Elastically Scattered Protons from Ti Target.....181

B.1 Diagrammatic Representation of Collision Between Proton and Atomic Electron in the Lab Frame.....188

C.1 Electronic Set-Up Used in Cherekov Counter Calibration Experiment.....194

C.2 Cherenkov Counter Efficiencies at Various Counter Distances and Various γ Energies.....205

D.1 Locus Spectrum for the Reaction $p+d \to {}^3He+\gamma$.....209

D.2 Angular Distribution of the Cross Section for the Reaction $p+d \to {}^3He+\gamma$.....213

D.3 Angular Distribution of the Analyzing Power for the Reaction $p+d \to {}^3He+\gamma$.....215

CHAPTER 1

INTRODUCTION

This thesis reports an experimental study of the reaction $P + T \rightarrow {}^4He + \gamma$ at proton energies of 227 MeV, 300 MeV and 375 MeV. The experiment was done at a number of scattering angles to study the angular distribution of the cross-section. Polarized proton beam was used, thus providing us with the analyzing power of the reaction as well.

The study forms part of a larger program of using the electromagnetic probe to look at light nuclei such as ^2H, ^3H and ^4He. This has been motivated by the desire to gain information on the nuclear structure as well as the reaction mechanism. Furthermore, comparison of the reaction with the existing inverse reaction data (Pic-70, Kie-73, Arg-75, Are-70, Sch-83) allows a test of one of the fundamental symmetries of nature, Time Reversal Invariance (TRI), in electromagnetic interaction of hadrons.

1.1 THE SIGNIFICANCE OF THE REACTION

The electromagnetic nature of the interaction provided an excellent tool to probe the nucleus. As it is a weak interaction compared to the nuclear strong interaction, it acts as a perturbation to the nuclear system. Moreover, the electromagnetic interaction, unlike the strong interaction, is well understood through quantum electrodynamics. The (p,γ) reaction is characterized by high momentum transfer to the residual nucleus. This means high momentum components of the nuclear wavefunction are

sampled. We get an opportunity to look at the exotic degrees of freedom of the nuclear wavefunction like short-range correlations. As we go up in the energy scale, various reaction mechanisms make themselves visible in varying orders of significance. The Direct knockout term also known as the Born term or Direct reaction term, dominant at lower energies, becomes less important at high energies. As the energy is increased, the Two Nucleon Model (TNM) term, also known as the two step mechanism, phenomenologically described under Quasideuteron model, becomes important. Even though at lower energies this effect is buried in the electric dipole transition through Siegert's theorem, as the energy increases it becomes necessary to include it explicitly through meson exchange currents. Mesonic and isobaric degrees of freedom become apparent. As described in Gar-81, the dominant mechanisms are described by the Shell-Model term, the Meson Exchange Current (MEC) term, the Correlation term, and the Δ isobar production term. In addition to looking at various reaction mechanisms, we also get an opportunity to look at the nuclear structure aspects of the nuclei ^{3}H and ^{4}He.

Since the reaction is related to $\gamma + {}^{4}He \rightarrow P + T$ through the principle of detailed balance, we need to discuss only one of the reactions. In the following discussions we will be concentrating on the reaction $\gamma + {}^{4}He \rightarrow P + T$.

1.2 VARIATION OF PHOTODISINTEGRATION CROSS SECTION AS A FUNCTION OF ENERGY

The total cross section for the photodisintegration is characterized by a peak at the incident γ energy between the threshold and 40 MeV. This peak is due to giant resonance. The

integrated absorption cross section in this peak is a large fraction of the value expected from the total nuclear dipole oscillator strength. Beyond the giant resonance region, the cross section falls off monotonically. Around 300 MeV, the cross section increases due to the Δ isobar. This is a nucleon excitation with a free width of about 115 MeV. Meson exchange currents play an important role in this energy region.

The low energy cross section may be expressed in terms of multipole contributions, without being concerned with the meson exchange current or isobar production. The total Hamiltonian is expressed as the sum of contributions from the nucleus, from the radiation field and from the interaction between them. Using the time-dependent perturbation theory, the probability of transition from the eigenstates of the uncoupled system to the eigenstates of the coupled system is found. For a quantum system the interaction of the radiation is given as the scalar product of two operators, one refering to the radiation field and the other to the nucleus. The Hamiltonian of the radiation field is given by:

$$H_\gamma = \sum_{k\lambda} \hbar \omega_k a^\dagger_{k\lambda} a_{k\lambda} \qquad (1.1)$$

where $a^\dagger_{k\lambda}$ and $a_{k\lambda}$ are the creation and annihilation operators for photons with wavevector k and circular polarization $\lambda = (\pm 1)$, respectively. $a^\dagger_{k\lambda} a_{k\lambda}$ gives the number of photons of type (k, λ). The radiation field is characterized by a vector potential $\vec{A}$ given by:

$$\vec{A} = \sum_{k,\lambda} \sqrt{\frac{2\pi\hbar c}{Vk}} \left(a_{k\lambda}\, \vec{e}_{k\lambda}\, e^{i\vec{k}\cdot\vec{r}} + \text{h.c.}\right) \tag{1.2}$$

where V is the normalization volume and $\vec{e}_{k\lambda}$ the polarization vector.

The interaction Hamiltonian is given in terms of the vector potential $\vec{A}$, nuclear current density $\vec{j}$ and nuclear magnetization $\vec{\mu}$ in the following fashion.

$$H_i = -\int \left(\frac{1}{c}\vec{j}\cdot\vec{A} + \vec{\mu}\cdot\vec{\nabla}\times\vec{A}\right) d^3r \tag{1.3}$$

The total Hamiltonian for the electromagnetic interaction is represented by H:

$$H = H_n + H_r + H_i \tag{1.4}$$

where H_n represents the Hamiltonian of the nucleus. The unperturbed system Hamiltonian is represented by H_o which equals $H_n + H_r$. Let the uncoupled system eigenstates be represented by $|N\rangle$. The interaction H_i is turned on at t = to and the eigenstates $|N\rangle$ develop into eigenstates $|\Psi_N(t)\rangle$ of the total system. This is expressed in the following expansion of Ψ_N along the basis $|N'\rangle$ with time dependent expansion coefficients $a_{N'N}(t)$:

$$|\Psi_N(t)\rangle = \sum_{N'} |N'\rangle a_{N'N}(t) \exp\left(-\frac{E_{N'}}{\hbar}t\right) \tag{1.5}$$

The probability per unit time, $W_{N'N}$ for the transition from N to N' is expressed in terms of $a_{N'N}$ and the density of final states $\rho(E_{N'})$:

$$W_{N'N} = \frac{d}{dt} \int |a_{N'N}(t)|^2 \rho(E_{N'}) \, dE_{N'} \tag{1.6}$$

Using eqn. (1.5) in the time-dependent Schrödinger equation, we solve for $a_{N'N}$. This is substituted in eqn. (1.6) to yield the transition probability:

$$W_{N'N} = \frac{2\pi}{\hbar} \left| - \langle N'|H_i|N\rangle + \frac{1}{\hbar} \sum_{N''} \frac{1}{W_{N''N}} \langle N'|H_i|N''\rangle \right.$$

$$\left. \langle N''|H_i|N\rangle \right|^2 \rho(E_{N'}) \tag{1.7}$$

The interaction Hamiltonian H_i may be expressed in terms of the angular momentum transferred to the nucleus. The nucleus may be described in terms of the projection of nuclear spin on the quantization axis (quantization axis standing for the propagation vector of the incident photon beam).

$$H_e^{\ell} = e \int \Psi_i^* \, z^{\ell} \, \Psi_e \, d^3r \tag{1.8}$$

$$H_m^{\ell} = e \int \Psi_i^* \, \vec{\sigma}_{\ell} \, \Psi_e \, d^3r \tag{1.9}$$

where H_e^{ℓ} is the matrix element for the transition between the

initial state, Ψ_i, and the final state, Ψ_e. The suffix ℓ stands for the electric multipole transition ℓ. The matrix element for the magnetic multiple transition is H_m^{ℓ}.

The first extensive calculation for the transition probability in terms of various multipoles was done by Partovi (Par-64) in the context of photodisintegration of deuterium. Partovi applied nonrelativistic phenomenological Schrödinger theory to calculate the transition probability. Approximations made are the neglect of nucleon structure, pion exchange currents and multipoles higher than the octupole. The nucleons were assumed to interact through a semiphenomenological potential developed by Hamada and Johnston (Ham-62) given in the following form:

$$V = V_c + V_T S_{12} + V_{LS} (\vec{L} \cdot \vec{S}) + V_{LL} L_{12} \tag{1.10}$$

where V_c is the central potential, V_T the tensor potential, V_{LS} the spin-orbit potential, and V_{LL} the quadratic spin orbit potential. The vector potential of the radiation field was expanded in plane waves of circular polarization.

$$\vec{A}(\vec{x}) = \frac{1}{\sqrt{\Omega}} \sum_{\omega} \sum_{\mu=\pm 1} \left(\frac{2\pi}{\omega}\right)^{1/2} \left[a_{\omega_\mu} \vec{\varepsilon}_\mu e^{i\vec{\omega}\cdot\vec{x}} - a^{\dagger}_{\omega_\mu} \vec{\varepsilon}_{-\mu} e^{-i\vec{\omega}\cdot\vec{x}} \right] \tag{1.11}$$

where a_{ω_μ} is the annihilation operator for a photon of momentum ω and polarization μ. The interaction Hamiltonian is H'.

$$H' = - \int \vec{J} \cdot \vec{A} \, d^3\tau \tag{1.12}$$

where $\vec{J}$ is the current density operator of the n-p system. The final state is characterized by total spin S and projection m^s of the n-p system and the initial state by the photon polarization μ and the deuteron projection quantum number m^d. The transition probability between these states was found using the interaction Hamiltonian given by eqn. (1.12).

Partovi's calculation covered energy regions up to 140 MeV. In this region the photodisintegration cross section may be fitted with a polynomial of the form given below:

$$\frac{d\sigma}{d\Omega} = a \sin^2\theta \, (1 + b \cos\theta + c \cos^2\theta + d \cos^3\theta + e \cos^4\theta) \quad (1.13)$$

where θ is the proton cm angle. Eqn. (1.13) is an electric multipole expansion including E1, E2 and E3 transitions. The electric dipole term is dominated by the transition $^3S - {}^3p$.

1.3 MESON EXCHANGE THEORIES

The experimental results of higher energies could not be explained if multipole transitions alone were taken into account. Explicit inclusion of meson exchange current along with the one-body current (or convection current) is necessary to take care of the total nuclear current. The total current thus obtained modified the interaction Hamiltonian which yields additional terms in the transition matrix. Furthermore, imposition of the gauge invariance condition yields additional terms in the transition matrix. In the low energy situation, meson exchange effects are taken into account

to first order implicitly through an electric dipole term applying current conservation. This is done by Siegert's theorem. We first take a look at Siegert's theorem.

The total nucleon current $\vec{J}$ is given in terms of the convection current $\vec{J}_N$ and the meson current $\vec{J}_M$.

$$\vec{J} = \vec{J}_N + \vec{J}_M \tag{1.13a}$$

This is substituted in eqn. (1.12) to get the interaction Hamiltonian. The vector potential $\vec{A}$ is substituted in terms of the polarization vector $\vec{\varepsilon}$ and the wave vector $\vec{k}$. We get:

$$H_{int} = \int \vec{J} \cdot \vec{\varepsilon}\, e^{i\vec{k}\cdot\vec{r}}\, d\vec{r} \tag{1.14}$$

$$\vec{\varepsilon}\, e^{i\vec{k}\cdot\vec{r}} = \nabla (\vec{\varepsilon}\cdot\vec{r}\, e^{i\vec{k}\cdot\vec{r}}) - i\vec{k}\, (\vec{\varepsilon}\cdot\vec{r})\, e^{i\vec{k}\cdot\vec{r}} \tag{1.15}$$

In the long wavelength limit, the second term in eqn. (1.15) vanishes and we get:

$$H_{int} \sim \int \vec{J} \cdot \nabla (\vec{\varepsilon}\cdot\vec{r}\, e^{i\vec{k}\cdot\vec{r}})\, d\vec{r} \tag{1.16}$$

Performing the integration by parts and assuming $\vec{J}(\vec{r})$ goes to zero for large r, we get:

$$H_{int} \sim - \int (\nabla\cdot\vec{J})\, (\vec{\varepsilon}\cdot\vec{r})\, e^{i\vec{k}\cdot\vec{r}}\, d\vec{r} \tag{1.17}$$

Now we invoke the equation of current conservation:

$$\vec{\nabla}\cdot\vec{J} + \frac{\partial \rho}{\partial t} = 0 \tag{1.18}$$

where ρ is the charge density contributed both by the nucleon field and the meson field. Rewriting the above equation, we get:

$$H_{int} \sim \int \frac{\partial \rho}{\partial t} (\vec{\varepsilon}\cdot\vec{r})\, e^{i\vec{k}\cdot\vec{r}}\, d\vec{r} \tag{1.19}$$

Now making use of Heisenberg's equation of motion:

$$\frac{\partial \rho}{\partial t} = \frac{i}{\hbar} [H, \rho] \tag{1.20}$$

Using the above two equations and the fact that the initial state $|i\rangle$ and the final state $|f\rangle$ are eigenstates of H with eigenvalues E_i and E_f, we get:

$$\langle f|H_{int}|i\rangle = \frac{i}{\hbar} (E_f - E_i) \langle f|\rho_o \vec{\varepsilon}\cdot\vec{r}\, e^{i\vec{k}\cdot\vec{r}}|i\rangle \tag{1.21}$$

where ρ_o is the expectation value of ρ. Comparing eqns. (1.14) and (1.21), we see that:

$$\vec{J} \cdot \vec{\varepsilon} = \frac{i}{\hbar} (E_f - E_i) \rho_o \, \vec{\varepsilon} \cdot \vec{r} \tag{1.22}$$

This means that in the long wavelength limit, the matrix element of the interaction Hamiltonian is proportional to the matrix

element of the electric dipole moment $\rho_o r$. This is known as Siegert's theorem. Note that this applies in the long wavelength limit or low energy region.

Because Siegert's theorem is valid to first order only, it cannot take care of the reaction mechanism at higher energies. Explicit inclusion of the resonant and non-resonant meson exchange current terms is necessitated at higher energies. Calculations in this regard have been done (Lon-76, Fin-76, Lon-79, Gar-81, Aren-82). Described below are the salient features of the MEC theory.

We start with the time-dependent Schrödinger equation and see how the gauge transformation for the vector potential, scalar potential and the wavefunction yields the perturbation expansion for the interaction Hamiltonian.

$$i\hbar \frac{\partial \Psi}{\partial t} = \left[-\frac{\hbar^2}{2m} \left(\vec{\nabla} - \frac{ie}{h} \vec{A} \right)^2 + e\phi + v \right] \Psi \qquad (1.23)$$

the above is the time-dependent Schrödinger equation in the presence of the electromagnetic field characterized by the vector potential $\vec{A}$ and scalar potential ϕ. Now we apply gauge transformation as follows:

$$\vec{A} \rightarrow \vec{A} + \vec{\nabla}\chi \qquad (1.24)$$

$$\phi \rightarrow \phi - \frac{1}{c} \frac{\partial}{\partial t} \chi \qquad (1.25)$$

$$\Psi \rightarrow e^{\frac{ie}{\hbar c}\chi}\Psi \tag{1.26}$$

Substitution of eqns. (1.24), (1.25) and (1.26) into (1.23) should retain the form of the Schrödinger equation intact in order for gauge invariance to hold good. This yields the following equation for the Hamiltonian:

$$H(\zeta,x) = e^{\frac{ie}{\hbar c}\chi} H(\zeta)\, e^{-\frac{ie}{\hbar c}\chi} \tag{1.27}$$

where H is the Hamiltonain and ζ are internal operators. We see the RHS of eqn. (1.27) may be expanded in the following fashion:

$$H(\zeta,\chi) = H(\zeta) + H'(\zeta,\chi) + \ldots \tag{1.28}$$

where H is the unperturbed Hamiltonian and H' etc. are corrections imposed by the gauge invariance. We may also observe the following equation from eqn. (1.27):

$$H'(\zeta,\chi) = [\chi,H] \tag{1.29}$$

The total nuclear current is given as a sum of one-body current and exchange current:

$$J_T = J_o + J_E \tag{1.30}$$

where:

$$J_o = \sum_i \left[\frac{e_i}{2m} P_i + \frac{\mu_i}{2m} \nabla x \ \sigma_i \right] \qquad (1.31)$$

which is the one-body current. The first term refers to the convection current and the second term to the magnetization or spin current. The meson exchange current J_E stands for two, three, etc. body currents. In the approach by Gari and Heback (Gar-81) the nuclear Hamiltonian H is split into a one-body operator T and two-body operator V.

$$H = T + V \qquad (1.32)$$

The requirement of current conservation for the total current J_T yields two relationships, one for the one-body current J_0 and the other for the exchange current J_E.

$$\vec{\nabla} \cdot \vec{J}_o = -\frac{i}{\hbar} [T, \rho] \qquad (1.33)$$

$$\vec{\nabla} \cdot \vec{J}_E = -\frac{i}{\hbar} [V, \rho] \qquad (1.34)$$

where ρ is the charge density. The form of H in eqn. (1.32) is replaced by another form as shown below.

$$H = (T + U) + (V - U) = H^{SM} + R \qquad (1.35)$$

where U is the single particle potential, H^{SM} the shell-model Hamiltonian and R the residual interaction. U is taken to be of the Wood-Saxon type:

$$U = \frac{-U_o}{1 + \exp\left((r-r_o)/a\right)} \tag{1.36}$$

where U_o = 58.5 MeV, r_o = 2.77 fm and a = 0.5 fm for ^{4}He.

The nuclear states $|\chi\rangle$ are expanded in terms of shell-model eigenstates $|\phi\rangle$.

$$|\chi_f^{\pm}\rangle = |\phi_f^{\pm}\rangle + \frac{R}{E_f - H + i\varepsilon}\,|\phi_f^{\pm}\rangle \tag{1.37}$$

$$|\chi_i\rangle = |\phi_i\rangle + \frac{PR}{E_i - H^{SM}}\,|\chi_i\rangle \tag{1.38}$$

where:

$$P = 1 - |\phi_i\rangle\langle\phi_i| \tag{1.39}$$

Now it is possible to express the transition matrix between the nuclear states in terms of shell-model states. The transition matrix is represented by M.

$$M_{fi} = \langle\chi_f| - \frac{1}{c}\int \vec{A}(\vec{x}) \cdot \vec{J}_T(\vec{x})\, d^3x |\chi_i\rangle \tag{1.40}$$

Substituting eqns. (1.37), (1.38) and (1.39) in the above

equation, Gari-Heback find that:

$$M_{fi} = \langle \phi_f^- | \Omega | \phi_i \rangle + \langle \phi_f^- | \frac{R}{E_f - H + i\varepsilon} \Omega | \phi_i \rangle + \langle \phi_f^- | \Omega \frac{PR}{E_i - H^{SM}} | \chi_i \rangle$$

$$+ \langle \phi_f^- | \frac{R}{E_f - H + i\varepsilon} \Omega \frac{PR}{E_i - H^{SM}} | \phi_i \rangle \qquad (1.41)$$

where:

$$\Omega = -\frac{1}{c} \int \vec{A}(\vec{x}) \cdot \vec{J}_T(\vec{x}) \, d^3x$$

$$\Omega = \Omega_o + \Omega_{exc} \qquad (1.42)$$

where Ω_o is the one-body contribution and Ω_{exc} is the exchange contribution.

Ω_o is contributed by the one-body convection current and one-body spin current as shown below:

$$\Omega_o = -\frac{1}{c} \sqrt{\frac{2\pi\hbar c}{k_\gamma}} \sum_{\alpha=1}^{A} \left[e_\alpha \vec{\varepsilon}_\lambda \cdot \frac{\vec{p}_\alpha}{M} - \frac{i\hbar}{2M} \mu_\alpha \vec{\sigma}_\alpha \cdot (\vec{\varepsilon}_\lambda \times \vec{k}_\gamma) \right] e^{i\vec{k}_\gamma \cdot \vec{r}_\alpha}$$

(1.43)

Let us take a look at each term in (1.41). The first term is split into two terms through eqn. (1.42), one of them standing for

the shell-model term and the other one standing for the exchange current term. Note that in the long wavelength limit the exchange current term becomes the Siegert term we saw earlier.

$$\Omega_{exc} = [V,Q] \tag{1.44}$$

where Q is the sum of all the electric multipole operators Q^L_λ.

$$Q = \sum_{L=1}^{\infty} Q^L_\lambda = \left[\sum_{L=1}^{\infty} \frac{2\pi\hbar c}{\sqrt{k_\gamma}} \left(\frac{2L+1}{L(L+1)}\right)^{1/2} \right.$$

$$\left. \frac{e}{k_\gamma} \left(1 + r \frac{d}{dr}\right) j_L (k_\gamma r)\, Y_{L\lambda}(r) \right] \tag{1.45}$$

The two-body potential V related to the exchange current through current conservation is given by the following expression:

$$V = - V_o \frac{e^{-\mu_\pi r}}{r} [a_0 + a_1 \sigma_1 \cdot \sigma_2 + a_\tau \tau_1 \cdot \tau_2 + a_{\sigma\tau} (\sigma_1 \cdot \sigma_2)(\tau_1 \cdot \tau_2)] \tag{1.46}$$

where V_o = 95 MeV, $a_0 = a_\sigma = -0.0025$, $a_\tau = -0.1025$, and $a_{\sigma\tau} = -0.2325$, for ^{4}He.

The second and third terms in eqn. (1.41) are known as correlation terms, arising from the residual interaction. These are described by giant resonances of L=1 and L=2 for ^{4}He. The last term

does not contribute in the first order.

The Δ(1232) resonance was introduced as part of two-body current:

$$J_2^{N\Delta} = \left[- A_o \left(\frac{E_\Delta^{Res}}{E_\gamma - E_\Delta^{Res}} \right) \frac{e^{-\mu_\pi r}}{\mu_\pi r} (\tau_1 x \tau_2)^3 \left(\vec{k}_\gamma \times (\vec{\sigma}_1 x \vec{\sigma}_2) \right) \right] \quad (1.47)$$

The terms mentioned so far are pictorially represented as in fig. 1.1a and fig. 1.1b. Fig. 1.1a gives the one-body interaction term and fig. 1.1b gives the exchange current terms. The first term in the exchange current contribution is the meson exchange current (MEC) term, the second the seagull term, and the third the Δ isobar term.

Gari-Heback found that with ^{4}He there is a considerable contribution from exchange currents in the energy region 40-400 MeV. The correlation contribution was found to decrease as energy increased. The shell model term showed no structure at 30° whereas it has a minimum at 120 MeV for 90°.

The Δ isobar contribution was calculated in detail by Londergan et al. (Lon-76) in the general case of a nucleus with A nucleons. They considered the diagram in fig. 1.2 for Δ formation.

The S matrix for the reaction was given by:

$$S = (2\pi)^4 \, \delta^4 (k_A + k_\gamma - k_N - k_{A-1}) \, M \quad (1.48)$$

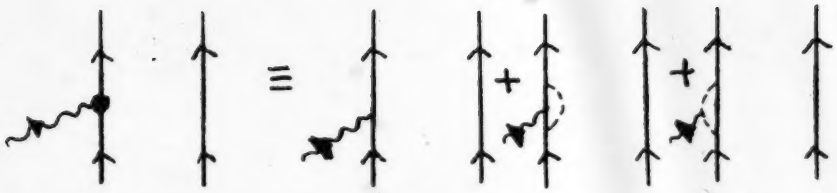

FIGURE 1.1a

ONE-BODY INTERACTION DIAGRAMS

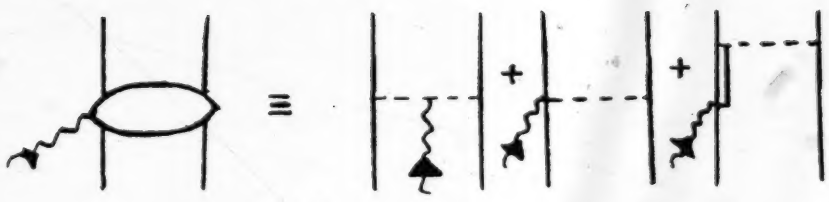

FIGURE 1.1b

MESON EXCHANGE DIAGRAMS

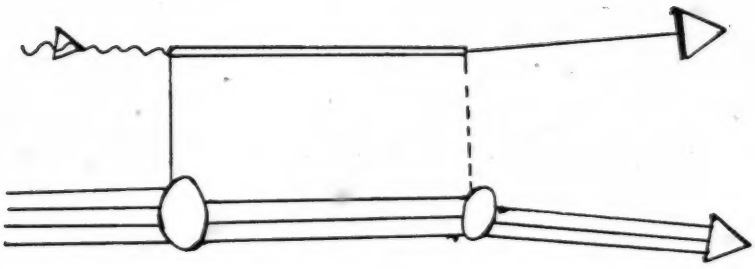

FIGURE 1.2

Δ ISOBAR DIAGRAM

where k's are various momenta and M the amplitude for transition. M was calculated by taking into account the contributions at the vertices $\pi N\Delta$, πNN and $\Delta\gamma N$. The following expression was obtained for the transition amplitude.

$$M = \sum_{\substack{\text{intermediate} \\ \text{states}}} \frac{dP_\Delta d\omega_\Delta}{i(2\pi)^4} \left[\frac{\langle A-1|H_{NN\pi}|(A-1)^*\pi\rangle\langle P\pi|H_{N\Delta\pi}|\Delta\rangle}{[E_N(P_\Delta-P_\gamma)-\omega_\Delta-E_\gamma-i\eta][E_\Delta(P_\Delta)-\omega_\Delta-i\eta]} \right.$$

$$\left. \frac{\langle\Delta|H_{\gamma N\Delta}|N\gamma\rangle\langle N(A-1)^*|H_N|A\rangle}{[E_{(A-1)^*}(k_\gamma-P_\Delta)+\omega_\Delta-E-i\eta][E_\pi(P_\Delta-k_\gamma)^2-\omega_\Delta-E_N(k_N)^2-i\eta]} \right] \tag{1.49}$$

where E_γ is the γ energy, and E(P) is the total energy corresponding to the momentum P. The term $(A-1)^*$ refers to the intermediate state. The nuclear wavefunctions were taken as the harmonic oscillator ones. Photon-nucleon vertex was calculated using both convection and magnetic moment contributions. The $N\Delta\gamma$ vertex was computed using the quark model of N and Δ as well as QED. The $\Delta N\pi$ vertex was described by Ψ_μ, the spin-3/2 Rarita-Schwinger field, Ψ the nucleon field, and ϕ the pion field.

$$H_{\Delta N\pi} = -i\left(\frac{f^*}{m_\pi}\right)\bar{\Psi}\,T\,\Psi_\mu\,\partial_\mu\,\phi \tag{1.50}$$

where T is the baryon isospin operator and $f^* = 2.097$ determined

from Δ decay width. Pion absorption was taken into account by summing $NN\pi$ vertices over the nucleons in (A-1) and A:

$$H_{NN\pi} = -i \left(\frac{2m_N f}{m_\pi} \right) \bar{\Psi} \gamma_5 \tau \Psi \cdot \phi \qquad (1.51)$$

where f = 1.009.

The form factors were included at the πNN and $\pi N\Delta$ vertices as shown below:

$$f(t) = f\left(\frac{\lambda^2 - m_\pi^2}{\lambda^2 - t} \right)^2 \qquad (1.52)$$

where $\lambda_{NN\pi} = 6.8\ m_\pi$, $\lambda_{\Delta N\pi} = 6.9\ m_\pi$.

More recently Arenhovel (Are-82) calculated the contribution of meson currents and isobar propagation. Exchange current contributions to various electromagnetic processes in nuclei, mostly to magnetic transition M1, were studied.

The inclusion of N'(1470) in the ground state of ^{4}He was found to be useful in getting the photodisintegration cross section at $E_\gamma < 400$ MeV (Lag-75). This study was motivated by the fact that even though Δ(1232) photoexcitation is the dominant process in the reactions $d(\gamma,p)n$ and $^4He(\gamma,p)^3H$, the cross section for the former is about 40 times that for the latter for $E_\gamma = 280$ MeV at $\theta_p = 90°$. The cross section was expressed in the following fashion:

$$\frac{d\sigma}{d\Omega} \alpha \left| \sqrt{1-\beta^2}\,(A+B) + \beta C \right|^2$$

where:

$$\Psi_{^4He} = \sqrt{1-\beta^2}\ \Psi_N + \beta\ \Psi_{N'}$$

where β^2 is the probability of finding a N'(1470) in the ^{4}He nucleus. Terms A, B and C are represented by the diagram in fig. 1.3 Laget found that a 3% admixture of N'(1470) in the ground state of ^{4}He reproduced the cross section at medium angles.

Arends (Are-78) notes that contrary to photodisintegration of the deuteron, but similar to the reaction ^{3}He(γ,p)^{2}H, there is no obvious evidence for a Δ(1236) resonance contribution to the reaction ^{4}He(γ,p)^{3}H. Theoretical investigation of the resonant and non-resonant pion exchange effects was done by Finjord (Fin-76). Calculations were done for the energy region 165 MeV to 330 MeV. Only the s-parts of the wavefunctions were considered and the final-state interactions between the proton and nucleus were neglected. Finjord found that non-resonant pion exchange contributions are dominant. However his results are strongly dependent upon the asymptotic form of the momentum space wavefunction.

1.4 QUASIDEUTERON AND OTHER PHENOMENOLGICAL MODELS

Levinger (Lev-51) proposed the quasideuteron model to explain

FIGURE 1.3
PROTON POLE, TRITON POLE, N'(1470) DIAGRAMS

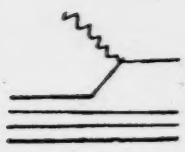

TERM A : PROTON POLE

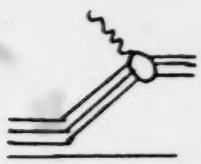

TERM B : TRITON POLE

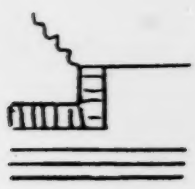

TERM C : N'(1470)

the cross section of nuclei with A > 3. He expressed the nuclear wavefunction in terms of the deuteron wavefunction on the assumption that two very close nucleons inside the nucleus constitute a quasideuteron. The wavefunction of the nucleus was expressed as a product of the deuteron wavefunction and the wavefunction for the remaining nucleons which provide a potential well in which the quasideuteron moves. The quasideuteron wavefunction is represented by $\Psi_k(r)$ given by the following expression:

$$\Psi_k(r) = \frac{(4\pi)^{1/2}\left[\frac{\sin(kr+\delta)}{\sin\delta} - \chi\right]}{(\alpha^2+k^2)^{1/2}\, v^{1/2} r} \qquad (1.53)$$

where χ is a function depending upon the shape of the potential, v the volume of the nucleus, and k the wavenumber corresponding to the relative motion of the proton and neutron of the quasideuteron.

$$k = |\vec{k}_1 - \vec{k}_2|$$

The phase shift δ is given by:

$$\cos\delta = -\frac{\alpha}{k}$$

where α^{-1} is scattering length. The ratio of the cross section for the photodisintegration of the quasideuteron to the photodisintegration of the free deuteron is given by the following

expression:

$$\frac{\sigma_{qd}}{\sigma_d} = \left(\frac{\psi_k}{\psi_d} \right)^2 = \frac{2\pi (1-\alpha r_o)}{\alpha(\alpha^2+k^2)v} \qquad (1.54)$$

where r_o is the effective range. The cross section for the photodisintegration of the nucleus is given by σ:

$$\sigma = 6.4 \frac{NZ}{A} \sigma_d \qquad (1.55)$$

where the factor 6.4 is known as the Levinger factor.

This model of the quasideuteron was essentially a forerunner for the Two-Nucleon-Mechanism (TNM) or the Siegert term in the electromagnetic interaction. The TNM proposed considered the momentum transferred to the nucleus by the incoming particle as being shared by two nucleons either by the formation of a quasideuteron or by Δ isobar production. These two terms are diagramatically represented in fig. 1.4.

The TNM is less sensitive to the high momentum components of the wavefunction since the momentum is shared by the nucleons of the p-n pair. The Single-Nucleon-Model (SNM) which could be called the direct knockout term, on the other hand, is more sensitive to the high momentum components of the wavefunction, since the momentum transferred is taken up by a single nucleon in the reaction, say, P + T $\rightarrow$ ^{4}He + γ. The one-body current term given by eqn. (1.43) stands for the SN mechanism. The differential cross section in the

FIGURE 1.4

QUASI-DEUTERON AND Δ-ISOBAR DIAGRAMS

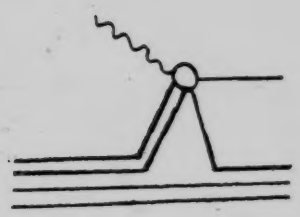

TERM A : QUASIDEUTERON

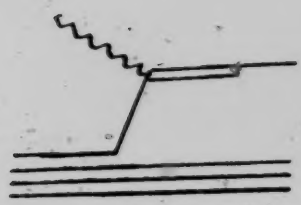

TERM B : Δ-ISOBAR

SNM is proportional to the square of the momentum space wavefunction of the bound proton.

$$\frac{d\sigma}{d\Omega}(E_p, \theta) = C(E_p, \theta)\left|\Phi_{J,L,m_J}(\vec{q})\right|^2 \qquad (1.56)$$

where C is the kinematic factor and Φ_{J,L,m_J} is the momentum space wavefunction of the nucleon with momentum $\vec{q}$ and specified by the quantum numbers J, L and m_J. The high momentum component of the nuclear wavefunction corresponds to the short range correlation of the nucleons, dominated by the exchange of heavier mesons ρ, ω.

Ruderman (Rud-52) took up the quasideuteron model and got an improved expression for the cross section (see Chapter 4). He expressed the nuclear wavefunction in terms of the wavefunction for the quasideuteron and the wavefunction for the remaining nucleons. He evaluated the cross section for $Pd \rightarrow t\pi^+$ in terms of the cross section for $PP \rightarrow d\pi^+$ on the assumption that the neutron in the triton does not participate in the interaction and that the incoming proton, after emitting a π^+ forms a quasideuteron with the proton in the deuterium.

This model was once more improved by Fearing (Fea-75a) (again see Chapter 4) to include distortion in the incoming channel and the outgoing channel. He also used improved wavefunctions for the nuclei. The nuclear cross section was expressed in terms of the cross section for $pp \rightarrow d\pi^+$, a form factor (which is the fourier transform of the overlap of the wavefunctions with respect to

momentum transfer), a spin factor and a kinematic factor. The form factor contained in it the distortion functions which were derived by integrating the distorting potential over the projectile path. The distorting potential, in turn, was obtained in a Glauber formalism where NN total cross section data and forward scattering amplitude data were used. The distortion reflected itself by giving normalization to the cross section whereas the form factor changed the shape of the angular distribution of the cross section. This is again because the form factor is a function of the momentum transfer which is a function of the scattering angle. The model is known as Distorted Wave Impulse Approximation (DWIA).

The comparison of the experimental results of this work with a DWIA model calculation may be seen in Chapter 4.

1.5 TESTING TIME REVERSAL INVARIANCE

This reaction provides a possible check on Time Reversal Invariance (TRI) in the electromagnetic interaction of hadrons. The principle of detailed balance (described later) relates the cross sections for the forward and the inverse reactions in terms of the momenta and spin multiplicities of various participants of the reaction. By comparing the results of the experiment with the inverse reaction data (Arg-75, Pic-70, Are-79, Sch-83, Kie-73) we could determine the validity of the time reversal principle. Described below are some of the aspects of TRI in the strong, electromagnetic and weak interactions.

The discovery of parity violation in weak interactions in 1957

(Hil-58) triggered the search for possible violations in strong, e-m and weak interactions. Combined CP non-conservation was observed in the decay pattern of the long-lived neutral K meson in 1964 by Christenson et al. (Chr-64). The ratio of weak decay of the K_L^0 into two pions to the sum of PC conserving decay rates was found to be close to 0.2%. The overall conservation of CPT is expected to hold, however, to a very high precision. This follows from invariance under relativistic transformations in local field theory. It relates properties of particles and anti-particles. The best experimental verification is the measured mass difference of K^0 and $\overline{K}^0$ where TCP is found to hold at a level of 1 in 10^{14}. Thus we conclude that CP invariance violation is associated T violation. K_L^0 decay therefore provides an indirect verification for the TRI in weak interaction. This indirect T violation encouraged everybody to look for a direct case of T violation in weak, e-m and strong interactions. The frontiers of investigation are: checking the principle of detailed balance, looking for T-odd terms in particle and nuclei decay, polarisation-analyzing power study for elastic and inelastic scattering and the electric dipole moment for the neutron. Described below are the details of these aspects.

It may be noted that the T operator is expressed as the product of a unitary operator and a complex conjugation operator. That is, T is antiunitary. This means that there is no conserved quantity associated with T unlike the case of parity operator.

T invariance can be tested in particles and nuclei by looking for T-odd terms which are known as T violating phases. Let us

consider the decay $n \rightarrow p + e^- + \vec{\nu}$. If σ is the neutron spin and p_1 and p_2 are the neutrino and electron momenta, then the terms $\vec{\sigma}\cdot(\vec{p}_1 x \vec{p}_2)$ is odd under time reversal. A non-zero expectation value of this term is an indication of T violation.

A number of tests of T invariance in nuclear gamma decays have been performed (Gim-79). Gimlett et al. looked at the 129 keV gamma transition in ^{191}Ir. The linear polarization of the 129 keV gamma ray was measured directly with a Compton polarimeter and making use of the Mossbauer effect. The correlation term $(\vec{J}\cdot\vec{k}x\vec{e})(\vec{J}\cdot\vec{k})(\vec{J}\cdot\vec{e})$ was looked for. Here $\vec{J}$ is the spin vector of the initial nuclear state, $\vec{k}$ the photon momentum and $\vec{e}$ the photon polarization vector. This term, as we may see, changes sign under T and so must have zero expectation value in the absence of final state effects.

The absence of electric dipole moment for any elementary particle is a consequence of TRI. In general, TRI prohibits all odd electric and even magnetic moments of the elementary particles. The measurement of electric dipole moment (Ram-81) yields a value of $|d_n| < 3 \times 10^{-24}$ cm, where d_n is the dipole moment per unit charge. This may be expressed as the product of a parity-violating coupling strength g_p, a T-violating coupling g_T and a hadronic length (Compton wavelength) λ_c. For the neutron this product is $10^{-20}\, g_T$ cm.

$$d_n = g_p g_T \lambda_c \approx 5 \times 10^{-7} \times 2 \times 10^{-14}\, g_T \text{ cm}$$
$$= 10^{-20}\, g_T \text{ cm}$$

where $g_T < 4 \times 10^{-5}$, which represents the most stringent limit for T-violation in nuclear physics.

For the elastic scattering of spin 1/2 particles by a target of arbitrary spin, polarization equals analyzing power, $P = A_y$. This was proved by Wolfenstein and Ashkin (Wol-52). This is a consequence of the invariance of the interaction under time-reversal. The P-A theorem states equality between the analyzing power in the direct reaction and polarization in the inverse reaction (Sat-58) for inelastic scattering. This is also a consequence of TRI. Note that a non-zero spin target is necessary, otherwise parity conservation alone dictates P=A. The term P-A for elastic scattering can be expressed in terms of the product of two amplitudes, one of which violates TRI while the other is T-invariant. Measurements of P and A for 180 MeV protons (Hil-58) scattered from lithium, beryllium and aluminum confirmed P=A to a few percent level. Comparisons of P and A for p-p elastic scattering (HUA-60) have shown P=A to a few percent level.

Let us now take a look at one other important aspect of TRI, namely the principle of detailed balance. The transition probability from state $|i\rangle$ to state $|f\rangle$ is related to the S-matrix in the following way:

$$W_{i \to f} \alpha |\langle f|s|i\rangle|^2 \rho_f \qquad (1.57)$$

where ρ_f is the density of final states. The invariance of the Hamiltonian H under T dictates the following equation:

$$S_T = T\ S\ T^{-1} = s^{\dagger} \tag{1.58}$$

where S_T is the time-reversed S-matrix. We get:

$$\langle f|s|i\rangle = \langle i_T|s|f_T\rangle \tag{1.59}$$

where i_T and f_T are the time-reversed states, that is, where spins and angular momenta are reversed. The relation gives rise to the following:

$$\frac{W_{i\to f}}{W_{f_T\to i_T}} = \frac{\rho_f}{\rho_{i_T}} \tag{1.60}$$

This equation yields, under the assumptions of parity conservation, absence of initial state polarization and no final state polarization detection, the following.

$$\frac{W_{i\to f}}{\rho_f} = \frac{W_{f\to i}}{\rho_i} \tag{1.61}$$

This equation is known as the principle of detailed balance. The reciprocity relation (1.60) holds good for individual spin states. Detailed balance is obeyed when all spin states are equally populated.

Let us consider the reactions a + b ↔ c + d. We can convert

eqn. (1.61) to an equation involving $\frac{d\sigma}{d\Omega}$, spin factors and centre of mass momenta, by summing over final spin states, averaging over the initial spin states, introducing the phase-space factors and dividing by the incident particle flux. We get the following relationship connecting the differential cross sections for the forward and the inverse reactions.

$$\frac{\frac{d\sigma}{d\Omega}(a + b \to c + d)}{\frac{d\sigma}{d\Omega}(c + d \to a + b)} = \frac{(2S_c + 1)(2S_d + 1)}{(2S_a + 1)(2S_b + 1)} \left[\frac{p_{cd}}{p_{ab}}\right]^2 \quad (1.62)$$

where $(2S_a + 1)$ etc. are the spin multiplicities, p_{cd} and p_{ab} are the CM momenta. This is also known under the name principle of detailed balance.

Non-observance of the above equation is an indication of TRI violation whereas the observance of the equation need not necessarily imply that TRI is holding good. This is because the reciprocity relation is guaranteed by the hermiticity of the Hamiltonian when the transition probability is given by Fermi's golden rule in the first-order perturbation theory.

By examining eqn. (1.62) it may be seen that the cross section for the forward reaction is equal to the cross section for the inverse reaction times a factor which is independent of the angle. This means that the shape of the angular distribution for the forward reaction is the same as the one for the inverse reaction.

A check of detailed balance was made for the reaction

$d + {}^{25}Mg \leftrightarrow p + {}^{25}Mg$ (Wei-68). It was found to be good within 0.3%. Accurate measurements of the cross sections for the forward and inverse reactions (Dri-79) have shown that detailed balance is generally good to 0.3%.

Let us now take a look at the detailed balance situation for the electromagnetic interactions. Bernstein et al. (Ber-65) suggested that the reactions of the form $\gamma + A \leftrightarrow B + C$ as a possible test for TRI. It may be noted that γ-N-N vertex, hermiticity and current conservation obscure any T-violation that may be present. Hence the above reactions must be conducted at resonance energies so that $\Delta(1232)$ production replaces the γ-N-N vertex by the γ-N-Δ vertex.

Investigation in this regard has been done for the reaction $p + d \leftrightarrow {}^{3}He + \gamma$ (Cam-82, Cam-83) and it is found that there is a very good agreement in the results which leads one to believe that TRI is holding good in the e-m interaction of the hadrons. It is worthwhile and interesting to make another attempt in this respect by studying the reaction $p + T \rightarrow {}^{4}He + \gamma$ and comparing that reaction to the existing inverse reaction data. This has been one of the motives behind undertaking to study this reaction.

CHAPTER 2

THE EXPERIMENT

2.1 THE CYCLOTRON

The experiment was performed at the 4BT1 station of the TRIUMF Cyclotron facility situated in Vancouver. This is a six-sector, sector-focussed negative-ion cyclotron. The beam extraction is done by inserting a carbon foil to strip off two electrons from the H^- ion. The beam is continuously variable in energy from 180 to 520 MeV, with an intensity of 100 μA at 500 MeV. Polarized and unpolarized proton beams are available with typical extracted intensities of 300 nA and 120 μA respectively. To avoid beam loss by gas stripping, a vacuum of 10^{-7} torr is maintained. The unpolarized ion source is of Ehlers type, giving 1-2 mA of H^- ions at 12 keV. The Lamb Shift polarized ion source (Don-71) is capable of giving 1 μA of 75-80% polarized beam at injection. The accelerating system consists of two rows of quarter-wavelength cavities operating at 23.055 MHz. This provides a 5 ns pulse every 43 ns.

2.2 PREPARATORY CALCULATION

It was important to have an estimate, before the start of the experiment, of various things such as the singles and coincidence count rates, multiple scattering, positioning of various detectors etc. It was also decided to check the working of the detectors and the electronics by measuring the cross section of $p + d \rightarrow {}^3He + \gamma$ (Appendix D), which had been measured earlier and therefore was well known. These consistency checks would then be a direct proof of the

correct functioning of the entire set-up.

The target used was TiT, therefore the singles count rate was dominantly determined by the differential cross-section for the proton to be scattered off Ti. The data was available for the cross sections - both elastic and inelastic - for the Ca target (Wal-66, Cha-56), which is close to that for Ti. The singles count rate is given by:

$$\text{count}_{\text{sin}} = IN \frac{d\sigma}{d\Omega} \Delta\Omega \qquad 2.2.1$$

where I is the beam intensity, N the number of Ti atoms per cm^2 of the target, $\frac{d\sigma}{d\Omega}$ the cross section value at the angle considered and $\Delta\Omega$ the solid angle subtended by the wire plane at the target. A typical value of the singles count rate was found to be 3×10^5/s at an angle of 15° for 300 MeV protons with an intensity of 10 nA.

The coincidence count rate was estimated using the inverse reaction data $\gamma + {}^4He \rightarrow P + T$ (Are-79). Equating the total CM energy for the forward and backward reactions gave the proton energy corresponding to the γ energy. The corresponding cross-section for $P + T \rightarrow \gamma + {}^4He$ was obtained using the principle of Detailed Balance assuming Time Reversal Invariance. A typical value of the coincidence count rate for 300 MeV protons with a 10 nA current was found to be ~92/hr for $\theta_\gamma^{CM} = 60°$ and ~1/hr for $\theta_\gamma^{CM} = 150°$.

The angular spreading of ^4He was calculated from the knowledge of beam spreading and multiple scattering. This calculation was

important in determining the distances of the front detectors from the target by making sure that the ^{4}He spreading did not exceed the boundaries of the Cherenkov counter image on the wire plane.

2.3 EXPERIMENTAL SET-UP

The experiment was carried out in a two-arm coincidence mode. The recoil ^{4}He's were detected in coincidence with the corresponding γ on the opposite side. The detectors were arranged on either side of the beam so that we had two-fold coincidence measurement (Fig. 2.1). By convention, the side was determined looking downstream from the target.

The cross section and the analyzing power were studied at three different proton energies; 227 MeV, 300 MeV and 375 MeV. The measurements were made at $\theta_\gamma^{CM} = 90°$ for 227 MeV, $\theta_\gamma^{CM} = 54°$, 65°, 78°, 90°, 99°, 118° for 300 MeV, and $\theta_\gamma^{CM} = 60°$, 91° for 375 MeV. These provided enough data to compare with the inverse reaction, thereby enabling us to draw conclusions on the validity of Time Reversal Invariance. The overall integrated charge at 300 MeV for $\theta_\gamma^{CM} = 65°$, 90°, 118° was roughly 415 μc for the target run and 230 μc for the background run. A total of 2.2 M events were recorded, 17,000 due to the pulser. The events due to (p,γ) were found to be 1502 at $\theta_\gamma^{CM} = 65°$, 441 at 90°, 287 at 118°, counts included for both sides. The corresponding numbers for the background run were 0.1 M, the pulser contributing 20,000. For the same energy at $\theta_\gamma^{CM} = 54°$, 78°, 99° the integrated charge was 875 μc

FIGURE 2.1

TARGET-DETECTOR ASSEMBLY

T	TARGET
WCL(R)	LEFT (RIGHT) WIRE CHAMBER
ΔEL(R)	LEFT (RIGHT) ΔE PLASTIC SCINTILLATOR
EL(R)	LEFT (RIGHT) E PLASTIC SCINTILLATOR
VL(R)	LEFT (RIGHT) VETO PLASTIC SCINTILLATOR
CL(R)	LEFT (RIGHT) CHERENKOV COUNTER

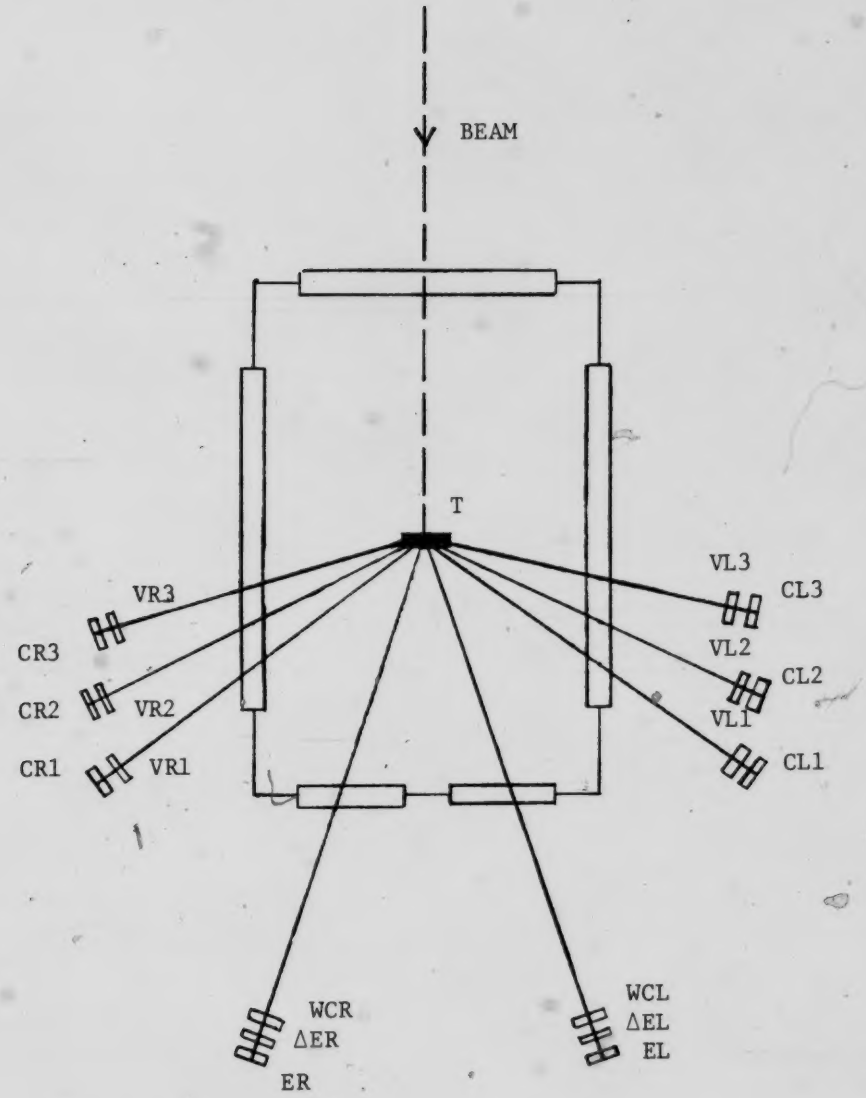
BEAM
T
VR3
CR3
CR2
VR2
CR1
VR1
VL3
CL3
VL2
CL2
VL1
CL1
WCR
ΔER
ER
WCL
ΔEL
EL

(1.1 M events, 0.2 M pulser events) for the target run and 446 μc (0.6 M events, 60,000 pulser) for the background run. The (p,γ) events were 3601 at 54°, 1770 at 78° and 860 at 99°. A total of 350 μc was collected for 227 MeV, corresponding to 0.5 M events and 22,000 pulser. The background run had 97 μc corresponding to 0.1 M events and 2400 pulser events. 560 events corresponded to (p,γ) at 90°CM. The integrated charges at 375 MeV were 206 μc (0.6 M events, 16,000 pulser) and 63 μc (0.1 M events, 5000 pulser) for the target run and the background run respectively. (p,γ) events were 816 at 60° and 285 at 91°.

It may be noted that the finite angular acceptance provided by the recoil particle detector made it possible to detect γ's at three different angles simultaneously. A typical value of the angular acceptance of the front detector was ±4°. At 300 MeV, an angular coverage of 10.8° to 18.8° enabled measurements of γ at angles (lab frame) 50° to 60°, 73° to 83° and 102° to 112°, which corresponded to 254-262 MeV, 234-243 MeV and 213-219 MeV γ's. The Cherenkov counters themselves had an angular acceptance of ±5°.

The entire experiment involving the above mentioned measurements along with one run for $p + d \rightarrow {}^3He + \gamma$ took up 74 runs spanned over a period of 10 days.

2.4 THE SCATTERING CHAMBER

A rectangular evacuated chamber of dimensions 33" x 23 1/2" x 19" was used to house the target. The chamber had two front windows separated by 3 1/4". Each window was of dimensions 9 1/4" x 3". The side windows, one on either side of the chamber, were of

dimensions 32" x 5". The back windows, separated by 3 1/4", were of dimensions 9 1/4" x 3". Kapton of thickness 127 μm was used for the windows. The dimensions of the front windows provided an angular sweep of approximately 5.5° to 33° on either side for the recoil particle. The side window dimension allowed an angular sweep of 36° to 144° for photons on either side. The back windows allowed measurements up to 174°.

2.5 THE TARGET

Tritiated titanium foil with a copper backing was used as the target. Background counts were obtained by using an identical nontritiated foil. The target, supplied by ORNL, was made by absorbing tritium into the crystalline structure of titanium evaporated onto a copper backing. When in use the target was placed in an aluminum enclosure maintained at a vacuum of 100 μ torr. 2" x 2" tantalum squares sandwiched the titanium foil. A 0.78" diameter hole at the center of the tantalum square exposed the tritiated region. This was held at the center of the aluminum enclosure by means of foam rubber spacers at the corners compressed between two window frames. A Kapton window of 1 mil thickness was glued onto the inside surface of each window frame. The frame was sealed onto the body of the enclosure by means of "O" rings.

To determine the tritium content, the cross section for (P,T) elastic scattering was measured using the MRS (Appendix A). Taking into account the decay loss, the thickness was deduced to be 1.28 mg/cm^2 at the time the experiment was done. The other constituents of the target were Ti (19.4 mg/cm^2) and Cu (5 mg/cm^2).

The targets mounted on the target ladder were tritiated titanium foil, nontritiated titanium foil, a ZnS screen and a CD_2 target. The ZnS helped locate and center the beam.

2.6 THE HELIUM BAG

The space between the scattering chamber front window and the wire chamber plane was filled by a plastic bag holding helium at atmospheric pressure. This helped reduce the multiple scattering of the recoil particles on the way to the detector.

2.7 THE δ-RAY MAGNET

A description of δ-rays is given in Appendix B. It was important to prevent δ-rays from getting into the front detectors. A magnet of 5 kG field strength was used to deflect away the δ-rays. The field was vertical so that δ-rays were deflected towards the right. The presence of the magnet was taken into account and the angles of the wire chambers were reset so that they would again be centered on the recoil particles scattered at the kinematically correct angles. An offset of approximately 1° was required for each wire plane.

2.8 THE POLARIMETER

The beam current and polarization were measured by an in-beam polarimeter situated at a distance of 250 cm upstream from the target. A detailed description appears elsewhere (Gre-79). Fig. 2.2 shows the polarimeter set up. The target used was a CH_2 foil of thickness 5.57 mg/cm^2. The polarimeter monitored the pp elastic scattering and the incident proton flux was elucidated from

FIGURE 2.2

POLARIMETER TARGET-DETECTOR ASSEMBLY

L1,2,3 LEFT SIDE 1,2,3 PLASTIC SCINTILLATOR

R1,2,3 RIGHT SIDE 1,2,3 PLASTIC SCINTILLATOR

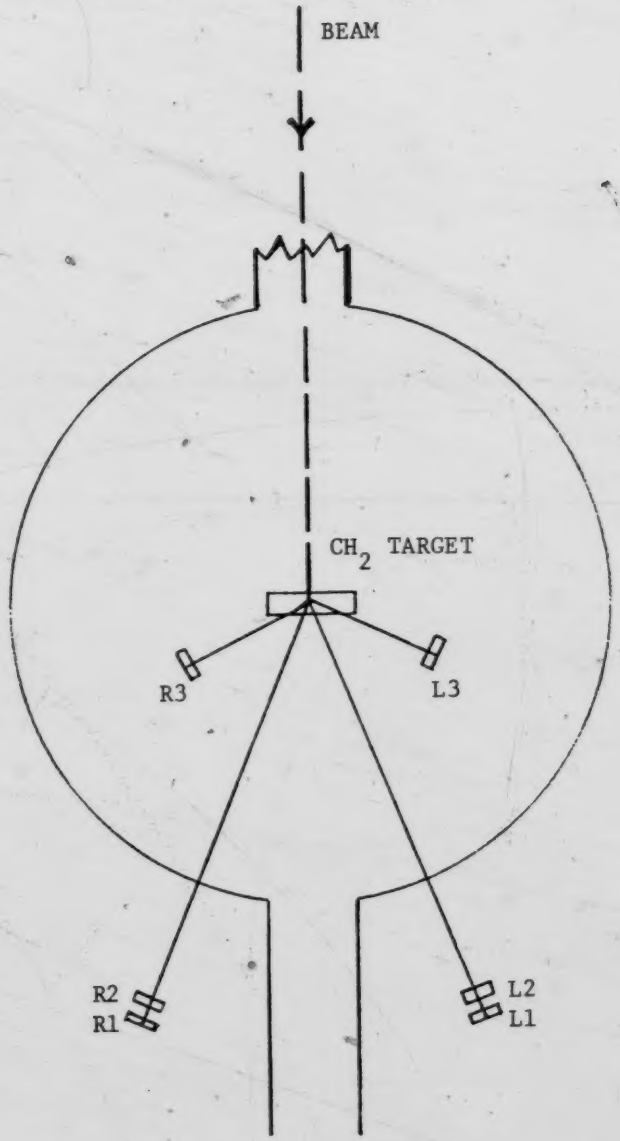
BEAM
CH_2 TARGET
R3
L3
R2
R1
L2
L1

the known cross section at $\theta_{lab} = 17°$. Beam polarization was determined from the p-p analyzing power, which is also well known. The value of the analyzing power at $\theta_{lab} = 17°$ is 0.414 at 300 MeV incident proton energy.

Plastic scintillator detectors L1, L2 and R1, R2 were placed at a lab angle of 17°. The corresponding recoil protons were detected by the scintillators R3 and L3. Because of the low energy of the recoil protons, backward detectors were situated inside the polarimeter scattering chamber. L1 and R1 determined the solid angle. These forward angle defining detectors were rotated such that normals drawn from their centers coincided at a point on the beam downstream from the polarimeter target. This positioning helped minimize differences in the left and right solid angles due to non-centering of the beam on the target. The effect was to increase (decrease) the solid angle at larger (smaller) scattering angles so that the count rate remained the same.

Fig. 2.3 shows the coincidence circuit associated with the polarimeter. The event was determined by L1·L2·R3 (left) and by R1·R2·L3 (right). Background from carbon was independently determined using a carbon target. L1·L2·R3 gave the contribution due to reals and accidentals for the left side. The accidental contribution alone was determined by a coincidence rate of R3 with L1·L2 delayed by 43 ns (the separation between consecutive beam bursts).

$$\text{No. of incident protons} = \left(\frac{P_{\ell} - P_{\ell acc} - P_{r} + P_{racc}}{F} \right) \qquad (2.8.1)$$

FIGURE 2.3

POLARIMETER ELECTRONICS

DISCRIMINATOR

AND GATE

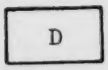

DELAY (43 ns)

SCALER

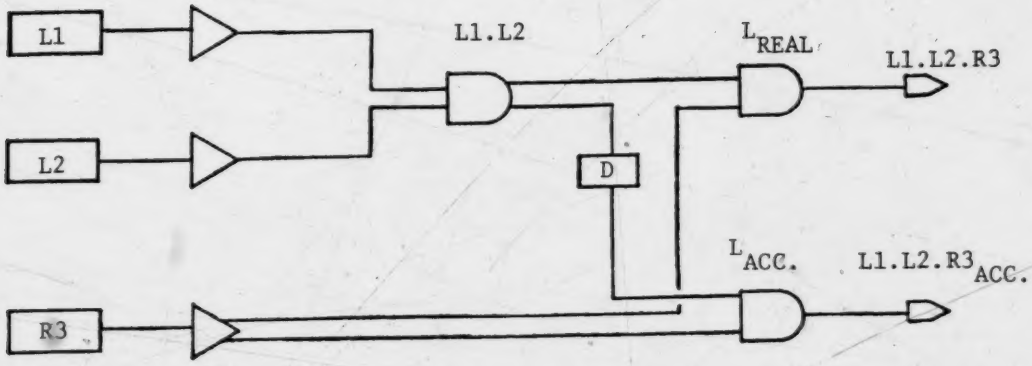
L1
L2
R3
L1.L2
D
L_{REAL}
L1.L2.R3
$L_{ACC.}$
$L1.L2.R3_{ACC.}$

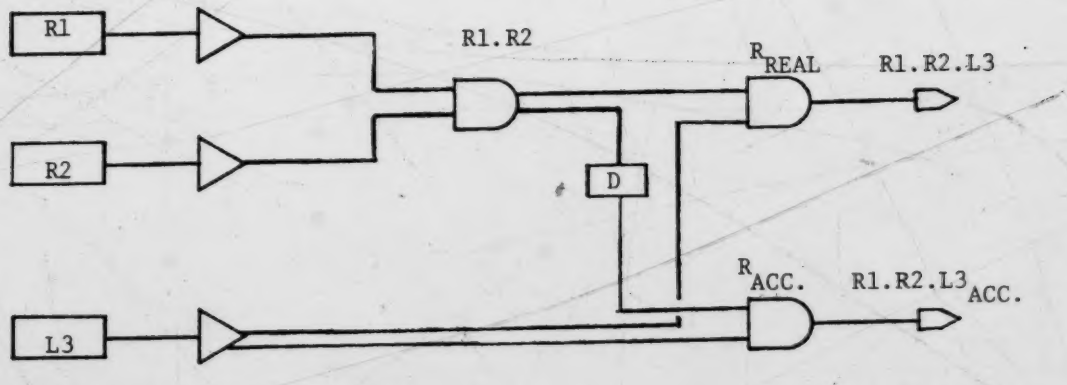
R1
R2
L3
R1.R2
D
R_{REAL}
R1.R2.L3
$R_{ACC.}$
$R1.R2.L3_{ACC.}$

where P_ℓ, $P_{\ell acc}$ refer to the total counts and accidental counts respectively for the left side: F is the polarimeter factor which stands for counts per nanocoulomb.

$$\text{Beam polarization} = \frac{1}{A}\left(\frac{P_\ell - P_{\ell acc} - P_r + P'_{racc}}{P_\ell - P_{\ell acc} + P_r - P_{racc}}\right) \qquad (2.8.2)$$

where A is the polarimeter analyzing power. The contribution to the analyzing power from C(p,2p) was accounted for by using the carbon target.

2.9 THE DETECTORS

The α particles were detected in an E-ΔE counter telescope. Looking downstream, this counter assembly followed a multiwire proportional chamber. The γ rays were detected in lead glass Cherenkov counters. These were preceded by a veto counter to discard events arising from charged particles (pions or electrons) getting into the Cherenkov counter. A detailed description of various detectors follows.

2.9.1 Charged Particle Counter Telescope

The ΔE detector was a plastic scintillator with dimensions 1/25" x 5" x 5". This was coupled to an RCA 8575 photomultiplier tube through a light pipe. The E detector was a plastic scintillator with dimensions 1/2" x 5" x 5", again coupled to an RCA 8575 photomultiplier tube through a light pipe. The scintillator material was NE110 plastic. The plastic was chosen to give

reasonable energy resolution and to accommodate the high count rate expected in these detectors (see Sec. 2.2). NE110 has good light transmission and a decay time of 3.3 ns.

2.9.2 Multiwire Proportional Chamber

Multiwire proportional chambers were used to obtain positional information on the recoil particles. Each chamber was 5" x 5" having an x plane and a y plane of 64 wires. Details of these MWPC are described elsewhere (Cai-75). The chambers had a -5 kV high voltage plane, an x sense plane, another high voltage plane, a y sense plane and yet another high voltage plane. The high voltage wires were 102 μm in diameter and were spaced 1 mm apart. The sense plane wires had separations of 2 mm and were 16 μm in diameter. The sense plane wires were of gold-plated tungsten whereas the HV plane wires were of beryllium and copper. The chambers had 25 μm thick kapton windows. A magic gas mixture was circulated through the chamber. The constitution of the magic gas mixture was 75% Ar (which was bubbled through methylal $CH_2(OCH_3)_2$ at 0°C), 24.5% isobutane C_4H_{10}, and 0.5% freon - 13B1 ($CBrF_3$). For details refer to (Cha-72). Argon provides the amplification, isobutane absorbs uv radiation (thus extending the proportional region allowing higher amplification), freon captures electrons (thus providing heavy negative ions near the positive ions and avoiding space-charge effects). It also avoids avalances. Methylal eliminates the degradation of MWPC's with integrated particle fluxes. The wire chamber readout system was of the amplifier per wire type (Cai-75).

2.9.3 The Cherenkov VETO Detector

A plastic scintillator (NE110), 6" x 6" x 1/8", was used as a veto counter before each Cherenkov. This was coupled to an RCA 8575 photomultiplier tube through a light pipe. Charged particles entering the Cherenkov counter which could cause false events were eliminated using signals from the veto's.

2.9.4 The Cherenkov Counter

Lead glass Cherenkov counters 7" long x 5" in diameter were used to detect γ's (see fig. 2.4). These were coupled to an RCA 8854 photomultiplier tube with RTV 602 silicon cement. The composition of lead glass by weight was: Pb, 51%; O, 26%; Si, 18%, K, 3%; and Na, 1.5%. The γ's in the lead glass undergo two dominant mechanisms: pair production and compton scattering. At higher energies (a typical value in the present situation, for the γ energy is 270 MeV for 300 Mev proton energy) pair production dominates. The resulting electromagnetic cascade shower yielded enough light to be seen by the photomultiplier tube.

Since the plastic scintillator had enough resolution (6%) to separate the α's corresponding to (p, π°) and (p, γ) reactions, it was not necessary to have a high resolution γ detector. The lead glass detectors gave γ detection with high efficiency (~90%).

The efficiency of the Cherenkov counters was estimated using a

FIGURE 2.4

CHERENKOV COUNTER ASSEMBLY

A	NYLON RING
B	LEAD GLASS
C	RTV 602 SILICON CEMENT
D	HOLLOW LUCITE CYLINDER
E	HOLLOW ALUMINUM CYLINDER
F	OUTER METALLIC CASING
G	PHOTOMULTIPLIER TUBE
H	NYLON RING
I	ALUMINUM RING ATTACHED TO PM TUBE HEAD
J	PM TUBE HEAD

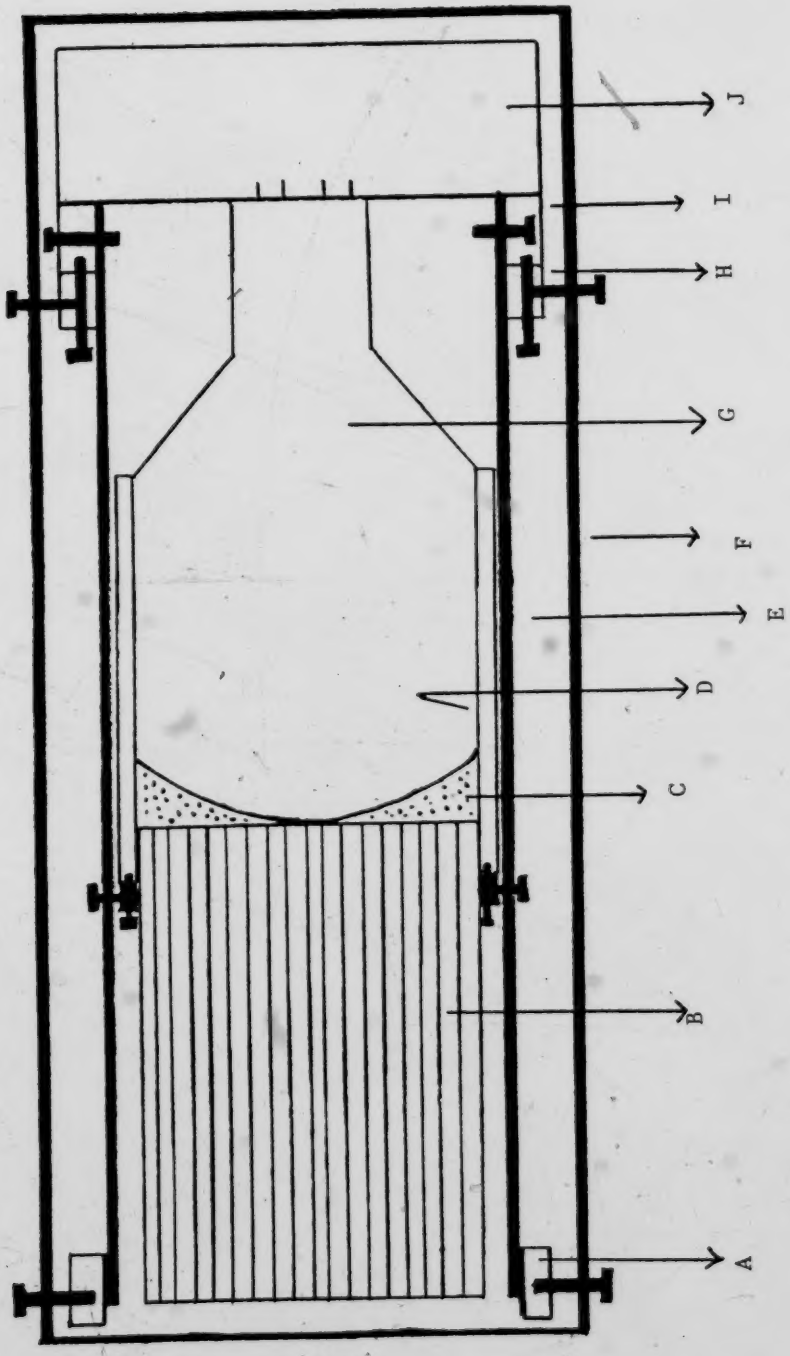
J
I
H
G
F
E
D
C
B
A

Monte-Carlo technique based on the one described by Sober (Sob-73). Electron calibration data (Appendix C) was used in this calculation to determine Cherenkov counter efficiency to detect γ's.

Fast signals from the E, ΔE and C detectors were used to form a trigger. The Multiwire Proportional Chamber (MWPC) provided the positional information for ^{4}He without participating in the event defining logic.

2.10 THE ELECTRONICS

The fast electronics used to form the trigger (figs. 2.5, 2.6, 2.7) were located in the experimental hall. This part of the electronics was used in the event formation and multiwire information processing. Fig. 2.5 gives the left-hand-side fast electronics. The photomultiplier signal pulse was split into two portions. One portion was fed into the Analogue to Digital Converter (ADC). The ADC unit used was LRS CAMAC model 2249. This is a high resolution (0.1%), multi-input (12-fold) ADC of charge integrating type. Input sensitivity is 0.25 pc/count. This has a dynamic range of 1024 channels. The other portion of the signal was fed into a discriminator. A constant fraction discriminator CFD 934 (EG & G ORTEC 934) was attached to E, ΔE and C detectors whereas the LRS NIM Model 621 was attached to the veto. CFD 934 is a quad discriminator with a double-pulse resolution of < 10 ns and threshold varying from -30 to -1000 mV. This module splits the input signal into two, delays one portion, and subtracts that from a constant fraction of the undelayed signal. The resulting signal has

FIGURE 2.5

LEFT SIDE FAST ELECTRONICS

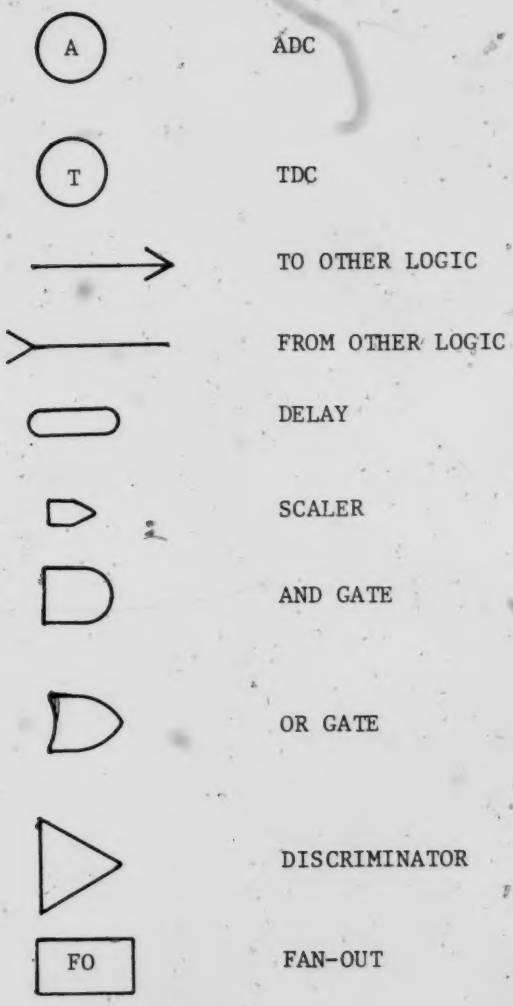

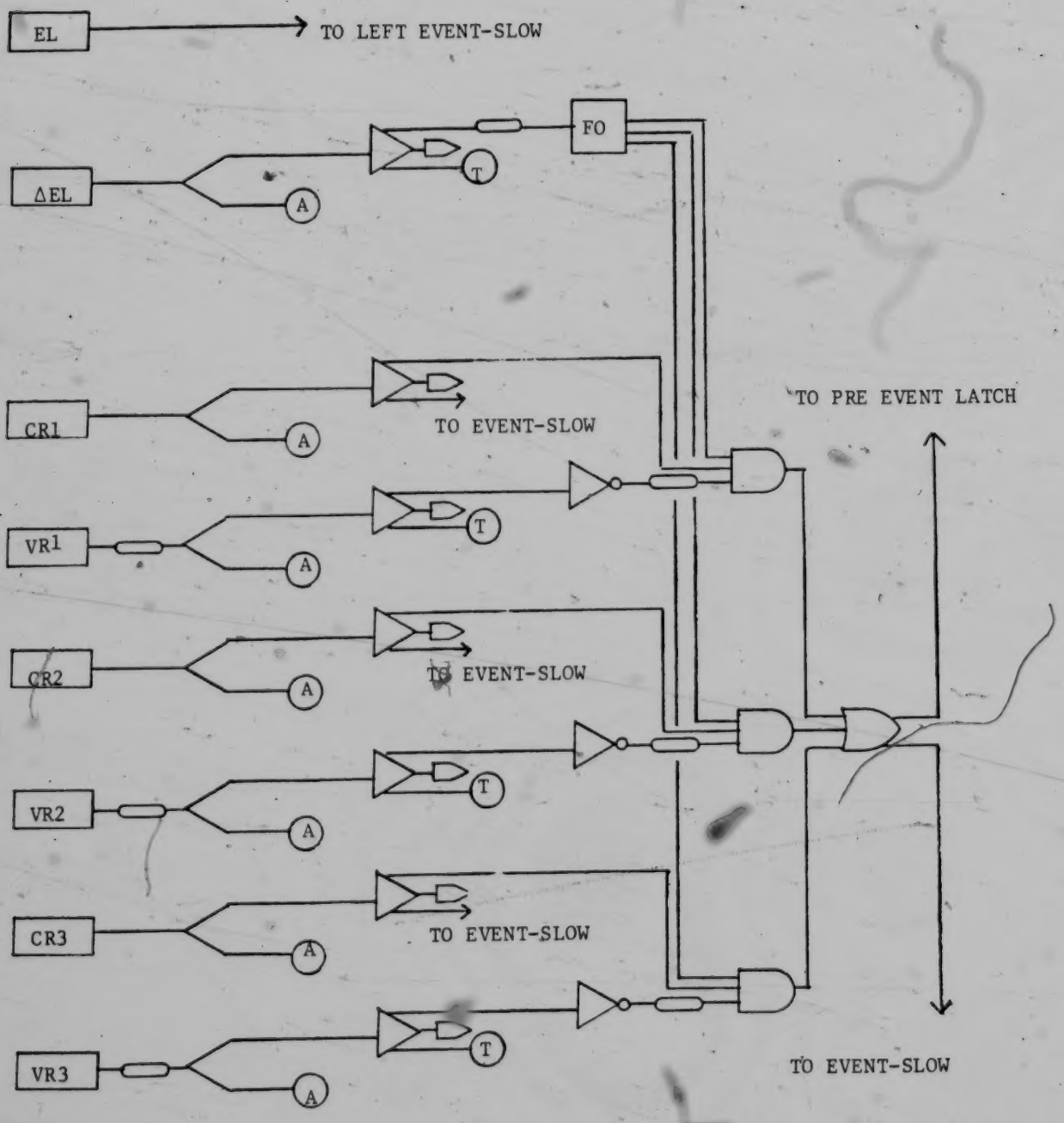
EL
TO LEFT EVENT-SLOW
FO
ΔEL
T
A
CR1
TO EVENT-SLOW
TO PRE EVENT LATCH
VR1
CR2
TO EVENT-SLOW
VR2
CR3
TO EVENT-SLOW
VR3
TO EVENT-SLOW

FIGURE 2.6

RIGHT SIDE FAST ELECTRONICS

DESCRIPTION IDENTICAL TO THE ONE FOR LEFT SIDE

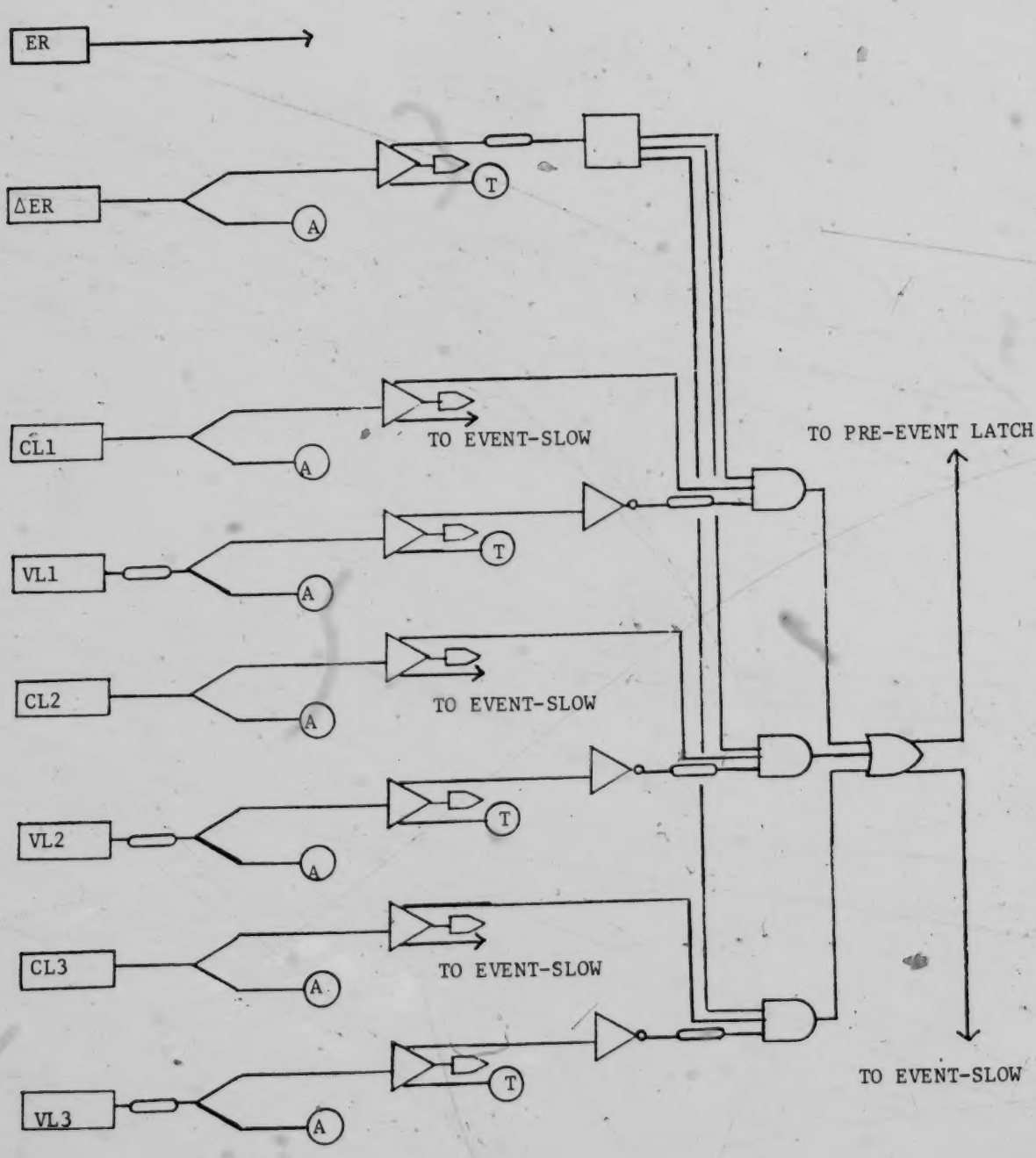
ER
ΔER
T
A
CL1
TO EVENT-SLOW
TO PRE-EVENT LATCH
VL1
CL2
TO EVENT-SLOW
VL2
CL3
TO EVENT-SLOW
VL3
TO EVENT-SLOW

FIGURE 2.7

PRE-EVENT LATCH AND MWPC ELECTRONICS

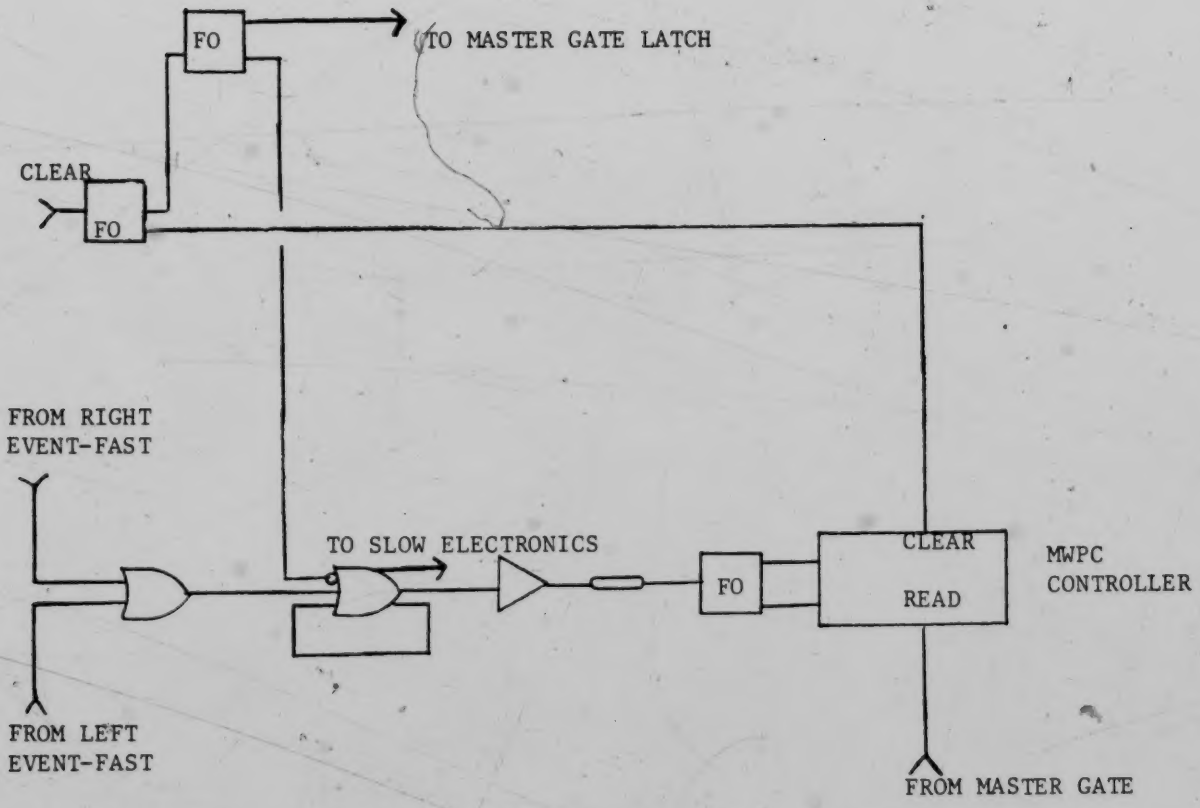
FO
TO MASTER GATE LATCH
CLEAR
FO
FROM RIGHT
EVENT-FAST
TO SLOW ELECTRONICS
FO
CLEAR
READ
MWPC
CONTROLLER
FROM LEFT
EVENT-FAST
FROM MASTER GATE

a baseline crossover independent of the input signal amplitude. This zero-crossing line is used to provide a precisely timed logic pulse. The output pulse is of width 6 ns to 150 ns with an amplitude of -800 mV. LRS 621 is a quad discriminator with a threshold of -30 mV to -1 V and an output of -700 mV to -800 mV with a minimum width of 5 ns. The maximum pulse rate that can be handled is 110 MHz.

One of the outputs from the discriminator is fed into a coincidence unit (LRS NIM Model 365). The other output goes to a Time to Digital Converter (TDC) (LeCroy CAMAC Model 2228A). The third output goes to a scaler (LRS CAMAC Model 84). Coincidence unit 365 has a double pulse resolution of 5 ns. The LeCroy 2228A is an octal TDC with an 11 bit resolution out of 2048 channels. This measures the time from the leading edge of the common start pulse to the leading edge of the individual stop pulse. This had 100, 200, and 500 ns full-scale time ranges and provides 50, 100 and 250 ps/count resolution respectively. Each channel disregards stop signals received before start signals and accepts only one stop for one start. The LRS Model 84 scaler provides 24 bits of data storage which may be stored at a rate of 100 MHz. Maximum capacity is approximately 17 M counts.

The outputs from the three AND gates were fed into an OR gate and its output defined EVENT FAST for that side. The outputs from the two sides were fed into an OR gate and its output was fed into the LATCH (LeCroy NIM Model 364) preceding the MWPC controller. LATCH caused the wire chamber information to be held until the slow electronics determined whether the event was good. The MASTER GATE

(MG) signal (fig. 2.9), among other things, caused the wire chamber information to be read into the computer memory. The data was read in via the CAMAC INPUT REGISTER (CAMAC Model IR-1). Once the information was read the controller was reset with a CLEAR signal, initiated by an 'EVENT-DONE' signal generated by the computer through OUTPUT REGISTER 5 (Fig. 2.9). This CLEAR signal also unlocked the LATCH imposed by EVENT FAST, thereby readying the LATCH for another event.

Fig. 2.8 shows one section of the SLOW ELECTRONICS. The LEFT EVENT FAST was set in coincidence with the signal from LEFT E. Similarly the RIGHT EVENT FAST was set in coincidence with the signal from RIGHT E. The outputs were fed into an OR gate (LRS Model 428) and subsequently fed into the MG. Note that LEFT EVENT FAST as well as RIGHT EVENT FAST were set into coincidence with the PULSER signal generated by the LRS Model 8010 PULSE GENERATOR. This was so that the MG would accept the PULSER events also, thus making it available for dead-time determination. One output of the pulser fan-out was fed into the digital coincidence register (DCR) (CAMAC C212 Unit) which generated a 24-bit word, each bit representing the status of an input.

Fig. 2.9 gives the final phase of the electronics. The PRE-EVENT started the LEFT TDC and RIGHT TDC. This also gated the FRONT ADC. The output signal of a Cherenkov counter in coincidence with the PRE-EVENT gated the BACK ADC. The PRE-EVENT also served as input to the MG. Output from the MG initiated storage of the event structure into the memory. This also strobed the DCR. Once the

FIGURE 2.8

PULSER, POLARIMETER, LEFT-SLOW
AND RIGHT-SLOW ELECTRONICS

(A) ADC

(T) TDC

(D) DCR

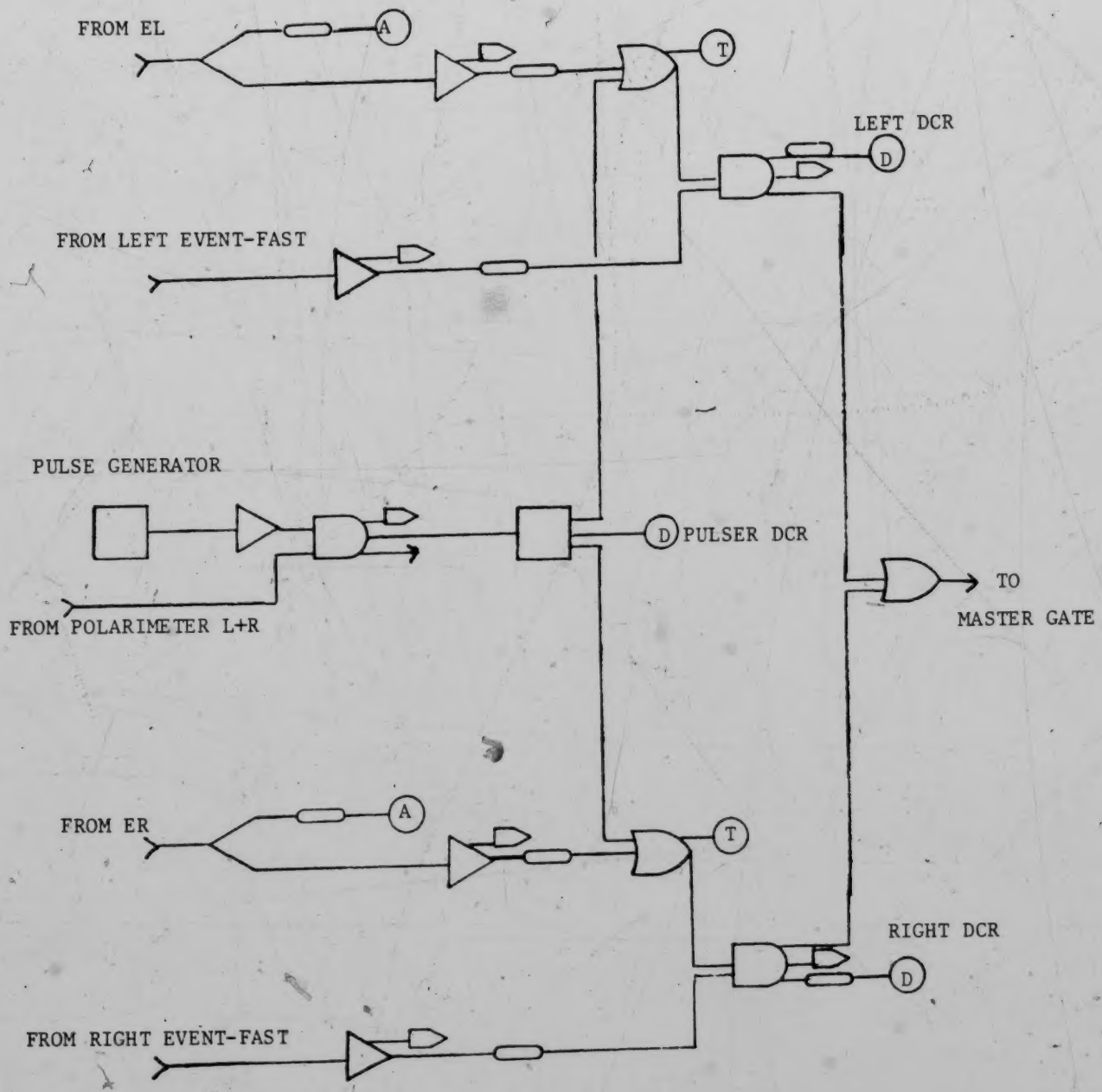
FROM EL
A
T
LEFT DCR
D
FROM LEFT EVENT-FAST
PULSE GENERATOR
D
PULSER DCR
TO
MASTER GATE
FROM POLARIMETER L+R
FROM ER
A
T
RIGHT DCR
D
FROM RIGHT EVENT-FAST

FIGURE 2.9

ADC GATE, TDC START STOP,

ADC, TDC CLEAR, MASTER GATE ELECTRONICS

OR	OUTPUT REGISTER
MG	MASTER GATE

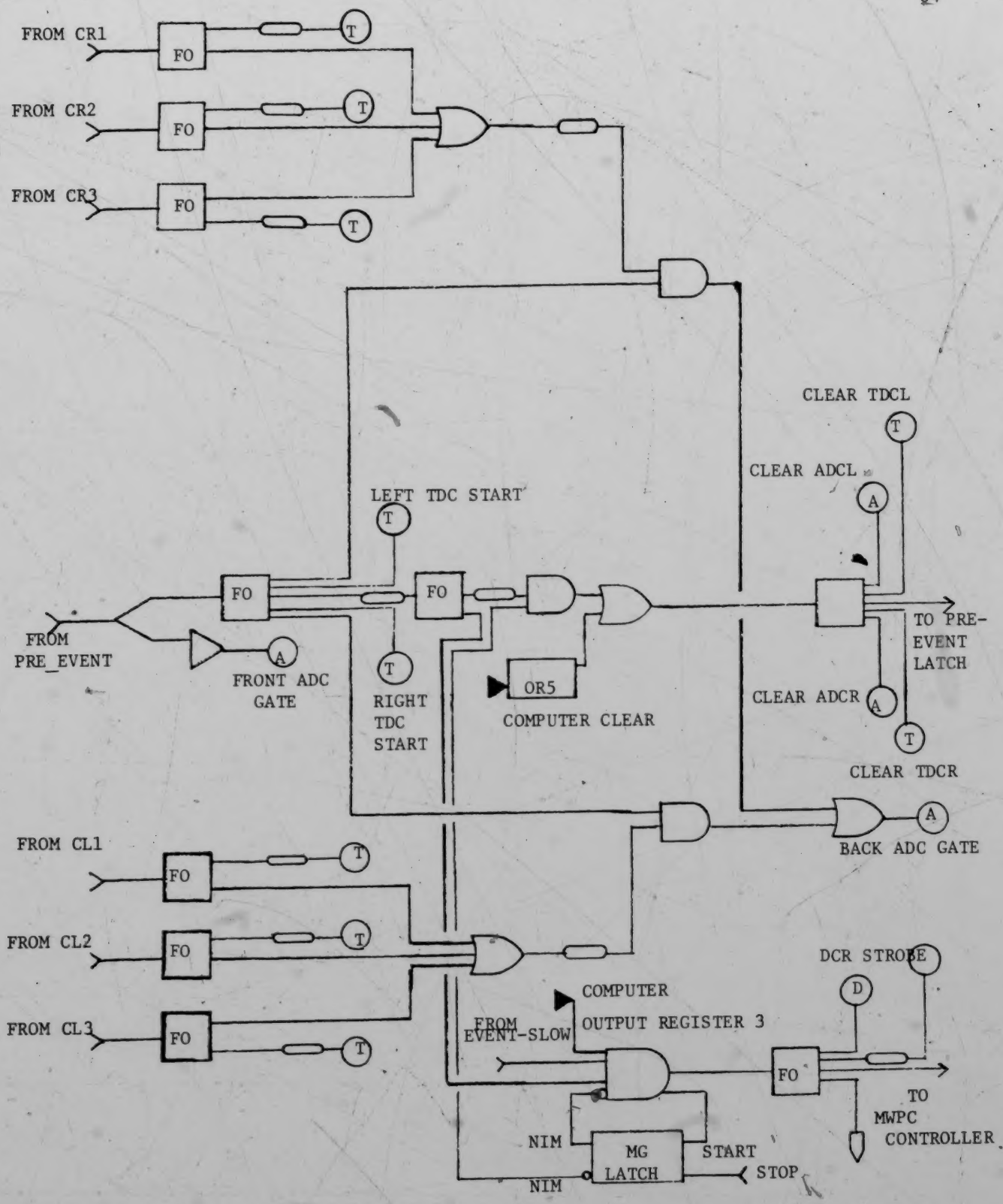
FROM CR1
FO
T
FROM CR2
FO
T
FROM CR3
FO
T
CLEAR TDCL
T
CLEAR ADCL
A
LEFT TDC START
T
FO
FO
FROM
PRE_EVENT
A
FRONT ADC
GATE
T
RIGHT
TDC
START
OR5
COMPUTER CLEAR
TO PRE-
EVENT
LATCH
CLEAR ADCR
A
T
CLEAR TDCR
A
BACK ADC GATE
FROM CL1
FO
T
FROM CL2
FO
T
FROM CL3
FO
T
DCR STROBE
D
COMPUTER
OUTPUT REGISTER 3
FROM
EVENT-SLOW
FO
TO
MWPC
CONTROLLER
NIM
MG
LATCH
START
STOP
NIM

event was written, the computer would issue a CLEAR signal through OUTPUT REGISTER 5. This reset the CAMAC units ADC, TDC, DCR and also cleared the LATCH attached to the MWPC controller. While the computer was busy, the MG was latched so that no other signal could form a MG during that time.

The LATCH is associated with the MWPC controller and the MG accounted for the electronic dead-time of the system. The rest of the dead-time was taken up by the computer processing the events. The dead-time of the system was inferred from the pulser, presented to the system (known from the pulser scaler), and the pulser accepted by the system (known from DCR information).

2.11 THE CAMAC

The CAMAC, standing for Computer Automated Measurement and Control, is an instrumentation system developed to accommodate digital circuits. A multiwire printed circuit board is mounted at the rear of the power crate. This provides interconnections between the modules and is known as CAMAC DATAWAY. CAMAC DATAWAY allows bidirectional communication between modules and computer or between modules. The crate used in the experiment had 25 stations (slots) to accommodate the CAMAC modules. Each slot had an 86 pair card-edge connector by which the modules gained access to the wiring of the crate (dataway). Control of modules within the crate was provided by the standard type-A crate controller which accepts external commands from the branch highway (path between crates and computer). The rightmost slots, i.e. the 24th and 25th slots were

FIGURE 2.10

CRATE NO. 1

A	C212 COINCIDENCE BUFFER (DCR UNIT)
B	LRS 2228 8 CHAN ADC
C	LECROY 2249 12 CHAN ADC
D	MODEL 85A QUAD SCALER
E	3615 HEX SCALER
F	MODEL 41 OUTPUT REGISTER
G	GEČ-ELLIOTT DBE 6501 DIFFERENTIAL BRANCH DRIVER
H	3900 TYPE A-1 CONTROLLER

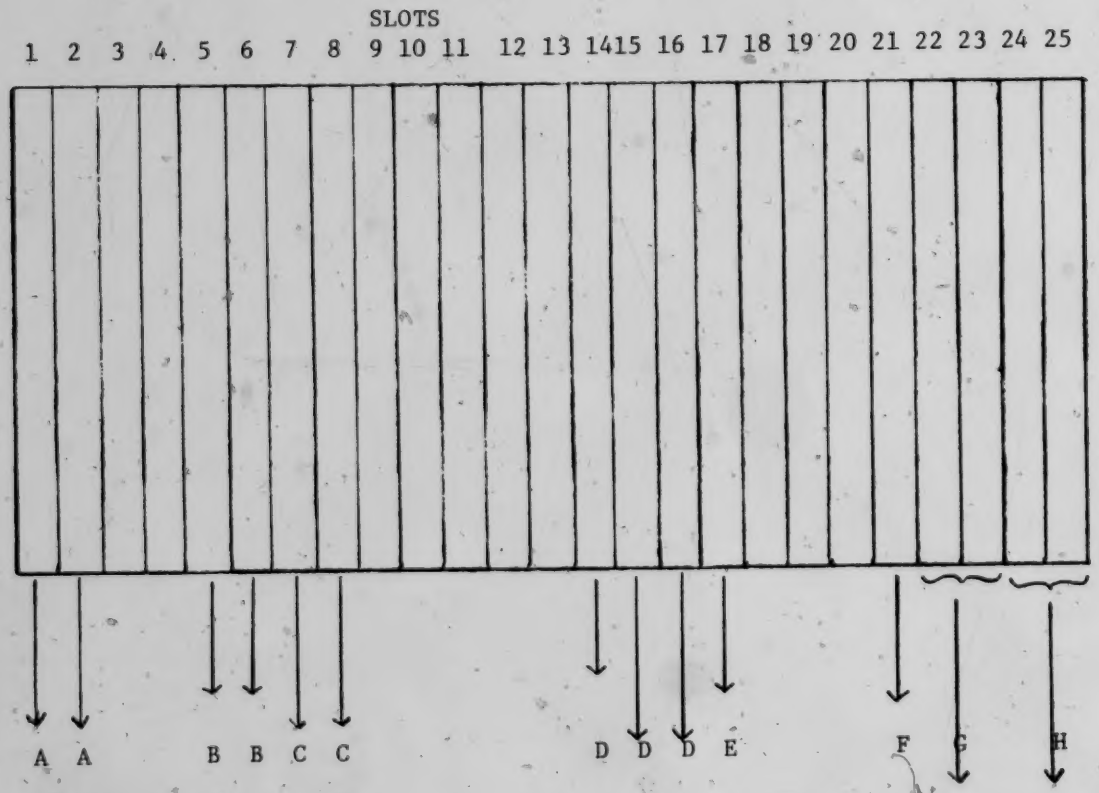
SLOTS
1 2 3 4 5 6 7 8 9 10 11 12 13 14 15 16 17 18 19 20 21 22 23 24 25
A A B B C C D D D E F G H

FIGURE 2.11

CRATE NO. 2

A	3655 TIMING PULSE GENERATOR
B	3615 HEX SCALER
C	3900 TYPE A-1 CONTROLLER

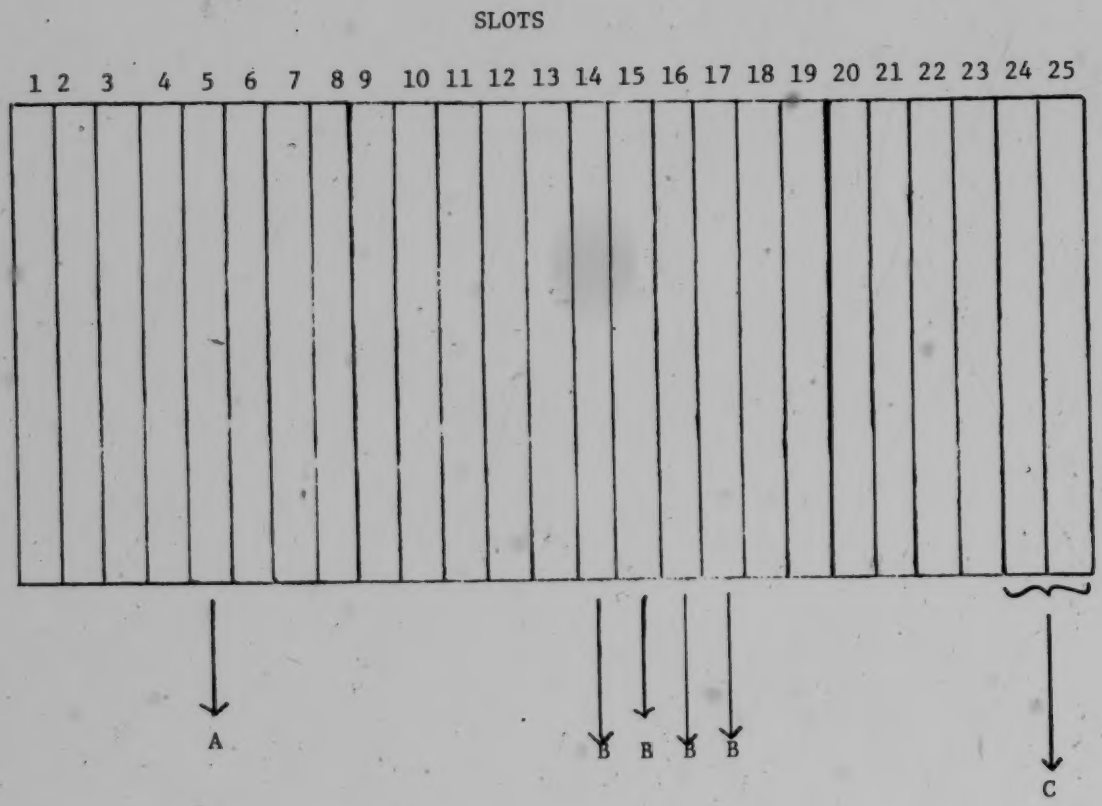
SLOTS
1 2 3 4 5 6 7 8 9 10 11 12 13 14 15 16 17 18 19 20 21 22 23 24 25
A
B B B B
C

FIGURE 2.12

CRATE NO. 3

A	MODEL 84 QUAD SCALER
B	IN/OUT REGISTER MODEL IR-1
C	GEC-ELLIOTT BRANCH DRIVER
D	3900 TYPE A-1 CONTROLLER

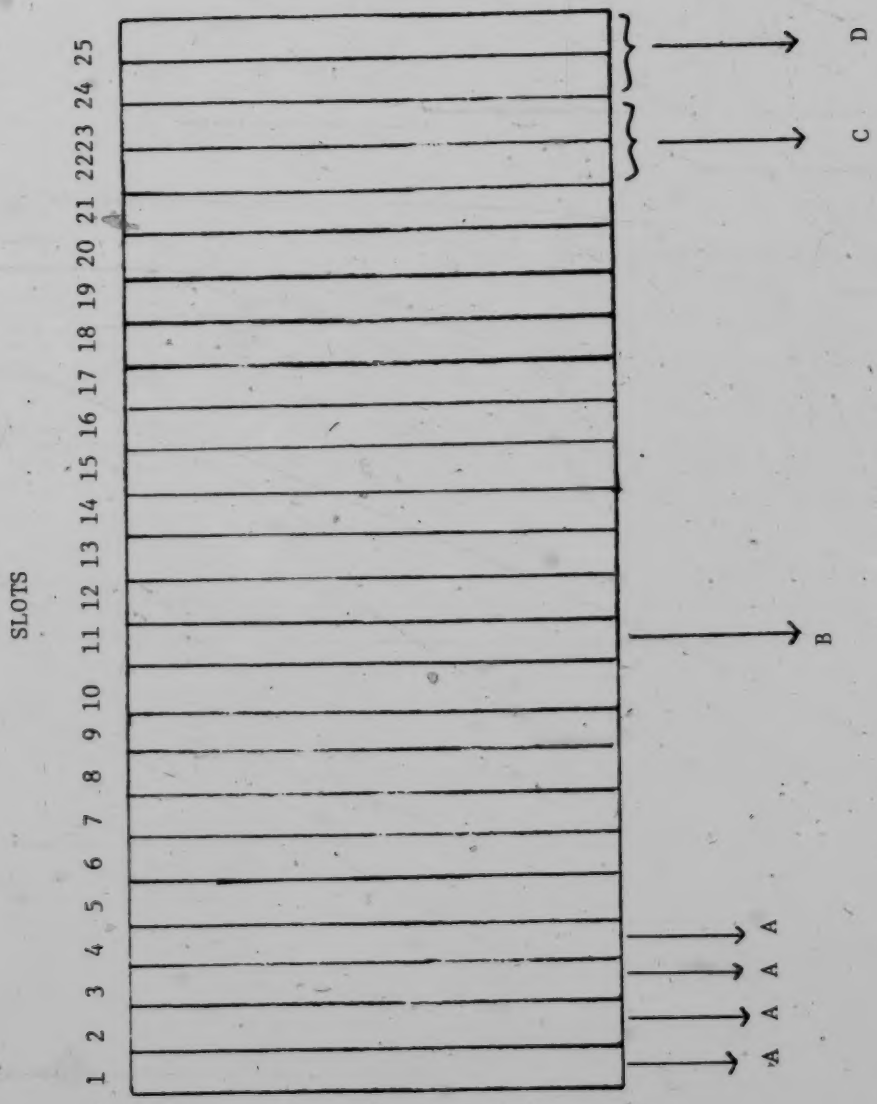
SLOTS
1 2 3 4 5 6 7 8 9 10 11 12 13 14 15 16 17 18 19 20 21 2223 24 25
A A A A
B
C D

occupied by a 3900 type-A crate controller. The rest of the slots were occupied by CAMAC units such as the ADC, TDC, DCR, etc.

Figs. 2.10, 2.11 and 2.12 show the allocation of various slots for the CAMAC modules used in the experiment. These modules were spread over three crates.

CHAPTER 3: THE DATA ANALYSIS

3.1 THE DATA ACQUISITION

The data was collected on magnetic tape, using a Honeywell 316 computer, on an event by event basis. The data contained the good events and the pulser events. The acquisition program, 'HONDA', is described in detail in Hut-81. The program 'HONDA' controlled the 3-crate CAMAC branch by means of a Daresbury DNPL-EC321A interface. In addition to writing the data onto the tape, the program also stored selected events in the computer memory, thus facilitating the display of various spectra on the printer or storage scope. Events to be written on tape could be subjected to certain criteria and software cuts determined from the displayed spectra.

3.2 THE DATA STRUCTURE

The data was written onto the tape in blocks of length 516 words, each word made up of 16 bits (Rog-77, Hut-81). The first 4 words contained information used in rereading of the tapes and the remaining 512 words contained the data. Each run recorded had a beginning block and an end block, giving information on the various parameters scaled during the run. These two blocks sandwiched a variable number of blocks each containing a variable number of records, a record representing the various parameters such as ADC, TDC, DCR and wire chamber co-ordinates, pertaining to a particular event. Table 3.1 lists the scalers relevant to a run. Table 3.2 lists parameters representing an event. Since the number of wires

TABLE 3.1

SCALERS

No.	Scaler
1	MASTER GATE
2	CR1 + CR2 + CR3
3	CL1 + CL2 + CL3
4	LF • RB
5	RF • LB
6	EL
7	ER
8	EL • LF • RB
9	ER • RF • LB
10	PULSER
11	SECONDARY EMISSION MONITOR
12	POLARIMETER LEFT
13	POLARIMETER LEFT ACCIDENTALS
14	POLARIMETER RIGHT
15	POLARIMETER RIGHT ACCIDENTALS
16	ΔEL
17	ΔER
18	CL1
19	CL2
20	CL3
21	CR1
22	CR2
23	CR3
24	VL1
25	VL2
26	VL3
27	VR1
28	VR2
29	VR3
30	THE ELAPSED TIME

LEGEND

CR1: Cherenkov Right 1
CL1: Cherenkov Left 1
LF•RB: Left Front • Right Back
RF•LB: Right Front • Left Back
EL: Left E
ΔEL: Left ΔE
ER: Right E
ΔER: Right ΔE
VL1: Veto Left 1
VR1: Veto Right 1

TABLE 3.2

THE EVENT STRUCTURE

Word No.	Parameter	
0	EVENT LENGTH	
1	FLAG	
2	LAM PATTERN	
3-4	DCR	
5	EL	TDC LEFT
6	CR1	
7	CR2	
8	CR3	
9	VR1	
10	VR2	
11	VR3	
12	ER	TDC RIGHT
13	CL1	
14	CL2	
15	CL3	
16	VL1	
17	VL2	
18	VL3	
19	ΔEL	ADC FRONT
20	EL	
21	ΔER	
22	ER	
23	CL1	ADC BACK
24	CL2	
25	CL3	
26	CR1	
27	CR2	
28	CR3	
29	VL1	
30	VL2	
31	VL3	
32	VR1	
33	VR2	
34	VR3	
35	MWPC DATA	
.		
.		
.		

hit is quite arbitrary, the event length is a variable. The 'FLAG' in the event structure is to indicate whether it is the last event or not. The 'LAM PATTERN' is the CAMAC 'look-at-me' signal issued by each CAMAC module when it needed the attention of the computer. 'DCR' stands for Digital Coincidence Register. This is a 24-bit word of which only 8 bits were used in the experiment. Each bit represents a characteristic of the event. Table 3.3 gives the DCR bit pattern.

3.3 THE DATA RE-ORGANIZATION

The total data collected during the experiment was recorded on 65 tapes each of 2400', at 800 bpi. This was quite an intimidating size and to facilitate the analysis it was decided to reorganize the data to make it more compact. The criteria used to achieve this are described below.

The information on the BUSY state of the beam, available from the ion source spin indicator, was used to reject events for which the beam spin was not clearly defined. These events, nevertheless, were recorded on the tape. They were discarded when the data was rewritten.

The MWPC data was of variable length, comprised of each wire with a detectable charge collected for both the planes. Only the centroid of the wires hit was important in the recoil angle calculation and so, the words standing for the addresses of the wires hit were reduced to a single word representing the centroid of the wires hit. Another word indicating whether there was a 'miss'

TABLE 3.3
DCR BIT-PATTERN

DCR Bit	Parameter
0	LF • RB • LE (LEFT EVENT)
1	RF • LB • RE (RIGHT EVENT)
2	LF • RB (LEFT EVENT; E not in trigger)
3	RF • LB (RIGHT EVENT; E not in trigger)
-	
-	
6	PULSER
7	BEAM SPIN UP
8	BEAM SPIN DOWN
9	BEAM SPIN OFF

or a 'multiple' was also included. A 'miss' occurred when no wire was hit. A 'multiple' occurred when the separation between the consecutively hit wires was greater than or equal to 3. Events characterized by a 'miss' or 'multiple', denoted by 'MM', were discarded when scatter plots or histograms were generated. They thus represented an inefficiency in the system and an appropriate correction was applied. To sum up, wire chamber data took up 4 words, 2 for each plane on the rewritten tapes.

The large flux of elastically scattered protons which infiltrated the recoil particle detector assembly caused spurious events which took up a good portion of the tape. A hardware attempt was made to cut these down to a manageable level by boosting the threshold of a Constant Fraction Discriminator attached to the ΔE detector. Some of the remaining protons were tracked down through a software cut involving the sum of the pulse heights in the ΔE plastic and E plastic. These protons, however, left the leading four words of the event structure on the tape. These events, called 'BAD' on-line, were discarded while the data was rewritten.

As may be seen from table 3.2, the event structure contained possible information from three different gamma detectors which was the general case. A particular event would however contain only data from one detector at a time. This meant it was possible to discard the words for the two non-struck detectors which were present in the original data sructure. This could be achieved if it was known which gamma detector gave rise to the coincidence. A cut on the Cherenkov counter TDC was imposed to make such an

identification. By examining the TDC spectrum, it was found that an event falling between TDC channels 15 and 645, which correspond roughly to 135 ns, would represent a signal in that detector. This identification was called time-of-flight test (TOF test). We thus ended up with ten words per event, as shown in table 3.4. TOF TEST WORD = 1, 2, 3, 6, 11, 12, 13 stood for CR1, CR2, CR3, pulser, CL1, CL2 and CL3 events respectively. Y MM = 1 stood for the fact that the y plane had a 'multiple' or 'miss'. X MM = 1 was the corresponding word for the x plane. Identification of the event this way had an additional advantage, since the most forward Cherenkov counters situated at $\theta_{c.m.}$ = 54° and 65° in two different configurations, corresponded to 57 MeV and 65 MeV α's (for E_p = 300 MeV) which stopped either in the ΔE plastic or in the wrappings between ΔE plastic and E plastic and hence the corresponding event could not be categorized LEFT or RIGHT since the LEFT or RIGHT DCR bit was defined with E in coincidence. Note also that the original DCR word was retained in order to identify beam polarization as well as to retain information on LEFT or RIGHT, if necessary.

The data was summarized into eleven 2400', 1600 bpi tapes, enabling an accelerated pace in further data analysis.

3.4 VARIOUS STAGES OF DATA ANALYSIS

3.4.1 Recoil Angle Calculation

The recoil angle was calculated from the x-plane centroid x and the y-plane centroid y. Fig. 3.1 shows the wire plane ABMD situated at a distance 'd' from the target T. The line TO represents the

FIGURE 3.1

RECOIL ANGLE DETERMINATION GEOMETRY

T	TARGET
TO	BEAM
ABMD	MWPC PLANE
C	CENTER OF MWPC PLANE
OC	NORMAL TO TC
$\theta = \angle OTC$	MWPC ANGLE WITH RESPECT TO BEAM
P	ARBITRARY POINT ON MWPC PLANE
PX	NORMAL TO OC FROM P
δ	RECOIL ANGLE

O
B
A
P
C
X
M
D
θ
δ
T
BEAM

TABLE 3.4

REWRITTEN EVENT STRUCTURE

Word No.	Parameter	
1	ORIGINAL DCR WORD	
2	TOF TEST WORD	
3	CHERENKOV COUNTER TDC	
4	CHERENKOV COUNTER ADC	
5	ΔE PULSE HEIGHT	
6	E PULSE HEIGHT	
7	Y MM	MWPC Information
8	Y CENTROID	
9	X MM	
10	X CENTROID	

beam line. C is the center of the wire plane and OC is the normal drawn to line TC, along the wire plane $\angle OTC = \theta$, the angle at which the wire plane is placed. The angle made to the beam line by the line joining the target T and any point on the wire plane, P is denoted by δ. PX is the normal erected from P to OC.

$$\delta = \cos^{-1}\left[\frac{OT^2 + TP^2 - OP^2}{2 \cdot OT \cdot TP}\right] \qquad 3.4.1.1$$

where $OT = d \sec\theta$

$$TP = \{d^2 + (x-x_c)^2 f^2 + (y-y_c)^2 f^2\}^{1/2}$$

$$OP = [\{d \tan\theta + (x-x_c)f\}^2 + (y-y_c)^2 f^2]^{1/2}$$

where x_c and y_c stand for wire numbers at point c, and f the interwire distance (2 mm).

3.4.2 Combining E and ΔE

The problem of the α's corresponding to the most forward Cherenkov counter stopping in the ΔE scintillator necessitated combining of the pulse height ΔP in the ΔE plastic and the pulse height P in the E plastic with appropriate weights to obtain the total energy ETOT of the α. The relative gains of the E detector and the ΔE detector were necessary to add P and ΔP. This was obtained by looking at the ΔP v/s P scatterplot of the passing protons (fig. 3.2) and also by knowing the thicknesses of the E and the ΔE detectors. Passing protons are represented by the straight

FIGURE 3.2

SCATTER PLOT OF ΔE PLASTIC PULSE HEIGHT VERSUS E

PLASTIC PULSE HEIGHT FOR PROTONS

A	REPRESENTS A COUNT OF 10
B	A COUNT OF 11
C	A COUNT OF 12
	AND SO ON
'+'	REPRESENTS A COUNT OF 36 OR HIGHER

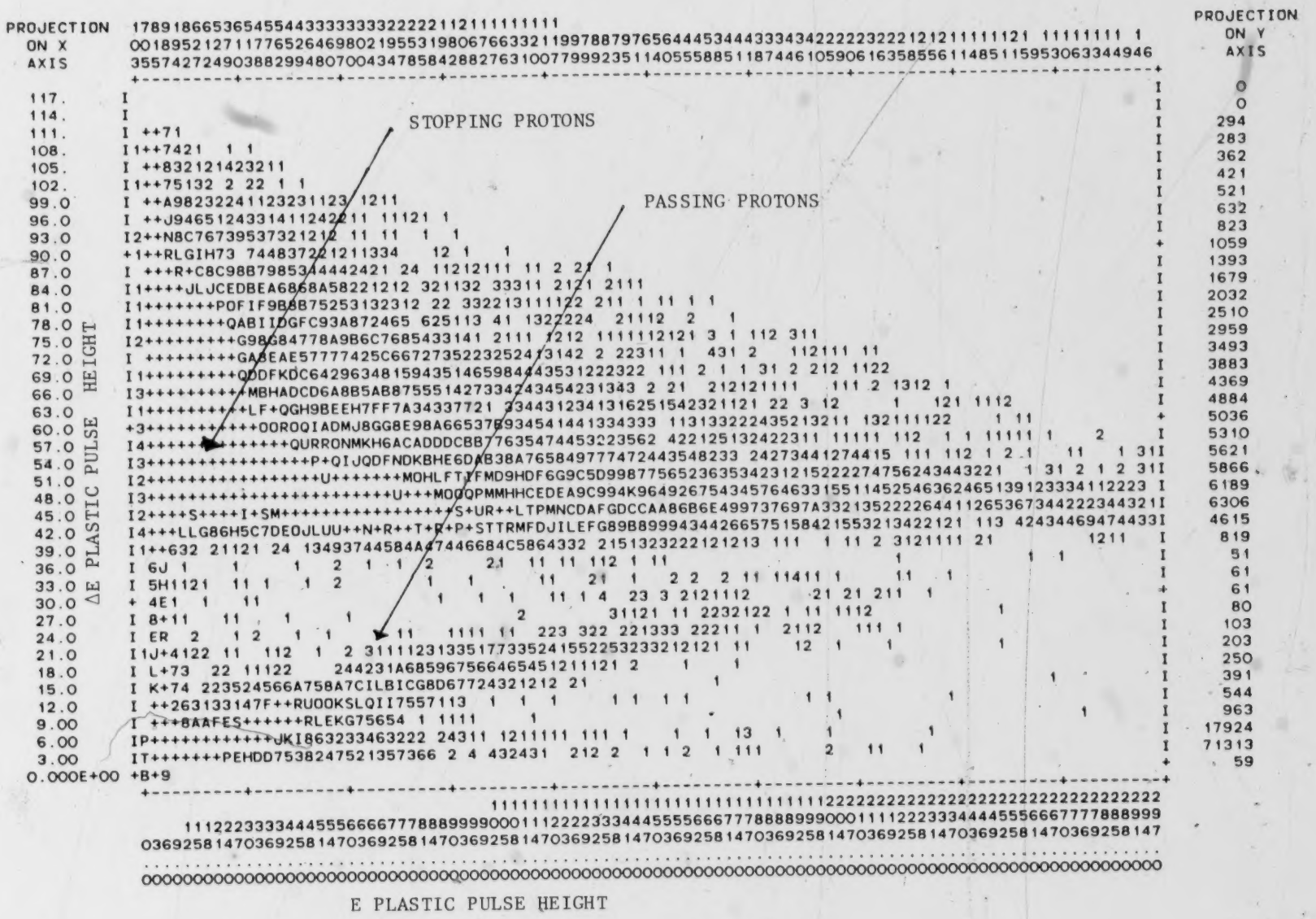
PROJECTION ON X AXIS
PROJECTION ON Y AXIS
STOPPING PROTONS
PASSING PROTONS
ΔE PLASTIC PULSE HEIGHT
E PLASTIC PULSE HEIGHT

line portion. The energy loss for these, to a good approximation, is directly proportional to the thickness of the plastic. Let ΔE and E represent the energy loss in the ΔE detector and in the E detector respectively.

$$\frac{\Delta E}{E} = \frac{\Delta t}{t} \qquad 3.4.2.1$$

where Δt and t are the thicknesses of the respective plastics.

$$\Delta E = a\ \Delta P \qquad 3.4.2.2$$

$$E = b\ P \qquad 3.4.2.3$$

where $\frac{1}{a}$ and $\frac{1}{b}$ are the gains of the ΔE detector and the E detector. Substituting these equations in eq. 3.4.2.1 we have:

$$\delta\ (= \frac{a}{b}) = \frac{P}{\Delta P}\ \frac{\Delta t}{t} \qquad 3.4.2.4$$

The absolute gains could be fixed arbitrarily as $\frac{a+b}{a}$ and $\frac{a+b}{b}$ for ΔE and E, or equivalently as $\frac{\delta+1}{\delta}$ and $(\delta+1)$ respectively.

$$ETOT = \frac{\delta}{\delta+1}\ \Delta P + \frac{1}{\delta+1}\ P$$

The normalization for this energy was determined by using the

ETOT v/s θ_{recoil} plot for (p,π°) and knowing the energy of the bending point from the kinematics.

The empirical relations thus arrived at are:

$$ETOT\ (LEFT) = 0.45 \cdot PE + 0.22 \cdot \Delta PE \qquad 3.4.2.5$$

$$ETOT\ (RIGHT) = 0.48 \cdot PE + 0.18 \cdot \Delta PE \qquad 3.4.2.6$$

3.4.3 Identification of (p,γ) Events

The off-line analysis was done using a DEC VAX-11/780 computer with a VAX/VMS operating system. The analysis program used, 'KIOWA', is described in detail in Ste-81a. The program was modified and adapted for the VAX-11/780. This program read a set of control cards representing the software cuts, imposed these cuts on the data read, chose the appropriate values of ADC, TDC, MWPC co-ordinates and other user defined parameters based upon the cuts, and generated one-dimensional and two-dimensional plots. In addition, it kept track of user defined scalers which were essential in evaluating the cross section. User defined scalers included (p,γ) events for three angles, split into contributions from spin up, spin down and spin off.

Fig. 3.3 gives the flowchart underlying the analysis program.

By convention, side was determined by α's. L1 refers to the LEFT 1 event, which in turn, refers to the most forward γ on the RIGHT side. L2 refers to the middle-angle γ, and L3 to the most backward γ on the RIGHT side.

The pulser events were first scaled and then eliminated from

FIGURE 3.3

(p,γ) IDENTIFICATION FLOWCHART

EVENT OR PULSER; E EVENT, P PULSER

SCALE

RETURN

SPIN UP (↑) EVENT OR SPIN DOWN (↓) EVENT
OR SPIN OFF (O) EVENT

LEFT EVENT (L) OR RIGHT EVENT (R)

MULTIPLE OR MISS

L1 EVENT OR L_2 EVENT OR L3 EVENT

DOES THE EVENT SATISFY E-ΔE CONDITION FOR CHARGE-2 PARTICLES?

REALS

DOES THE EVENT LIE ABOVE CHERENKOV PULSE HEIGHT CUT?

DOES THE EVENT LIE INSIDE THE p,γ CUT IN LOCUS SPECTRUM?

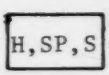

PLOT HISTOGRAMS, SCATTER PLOTS AND PRINT USER-DEFINED SCALERS

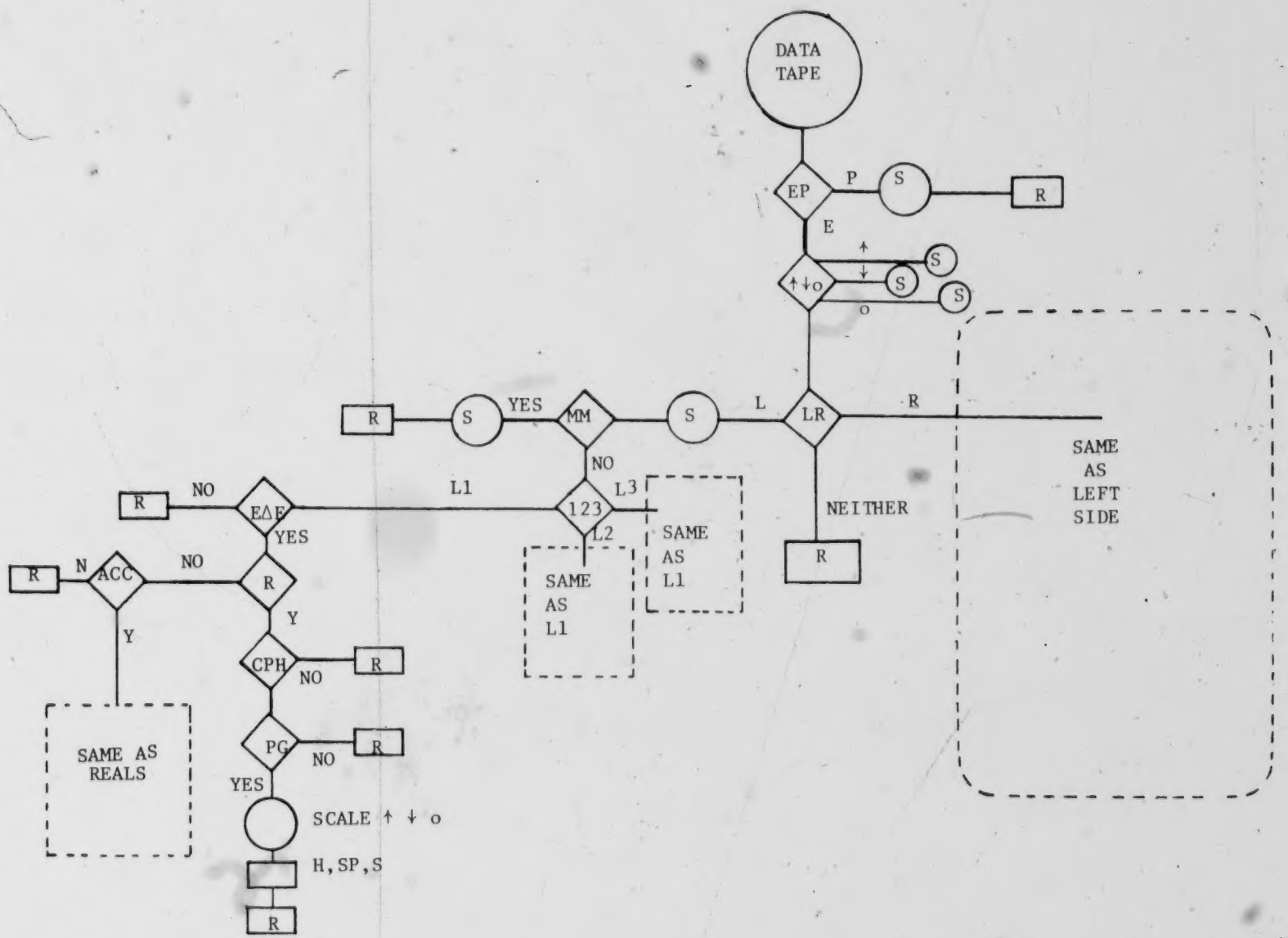
DATA TAPE
EP
P
S
R
E
↑↓o
S
S
S
o
R
S
YES
MM
S
L
LR
R
NO
L1
123
L3
L2
SAME AS L1
SAME AS L1
NEITHER
R
SAME AS LEFT SIDE
R
NO
EΔE
YES
R
N
ACC
NO
R
Y
Y
CPH
NO
R
PG
NO
R
YES
SCALE ↑ ↓ o
H,SP,S
R
SAME AS REALS

the main course of analysis. The rest of the events were separated into spin up, spin down, and spin off, and scaled. The next check was to determine whether it was a LEFT or RIGHT event. If the event belonged to neither, it was discarded. The analysis of LEFT and RIGHT took the following identical steps.

The events labelled 'MM' (described earlier) were scaled and eliminated. A check was made to see whether the event was L1, L2 or L3 (R1, R2, R3 for RIGHT side). Once this was established, the following identical steps were taken for L1, L2, and L3 (R1, R2, R3).

The scatterplot of ΔE vs ETOT was formed which helped separate charge-1 particles from charge-2 particles. The clear separation achieved between protons and α's may be seen in Fig. 3.4. The unwanted protons were eliminated with ΔE-ETOT cut. Fig. 3.5 gives the spectrum after eliminating the protons.

The next step was to generate the scatterplot of ETOT vs time-of-flight for the α-particles (Fig. 3.6). Of the two distinct peaks, the prominant one represented the REALS and the other the ACCIDENTALS. The term ACCIDENTALS refers to the accidental coincidence between $\alpha(\gamma)$ from a beam burst and the $\gamma(\alpha)$ from another beam burst. The ACCIDENTAL contribution, when subtracted from the REALS gave the TRUE number of coincidences in one beam burst.

The next step was to generate the Cherenkov pulse height histogram corresponding to REALS (Fig. 3.7) and ACCIDENTALS (Fig. 3.8. These two histograms helped elucidate the fact that the prominant peak in the beginning channels of the Cherenkov pulse

FIGURE 3.4

ΔE VERSUS E SPECTRUM FOR PROTONS AND ALPHAS

REACTION $P + T \rightarrow \alpha + \gamma$

$T_P = 300$ MeV

$\theta_\alpha^{Lab} = 15.3°$

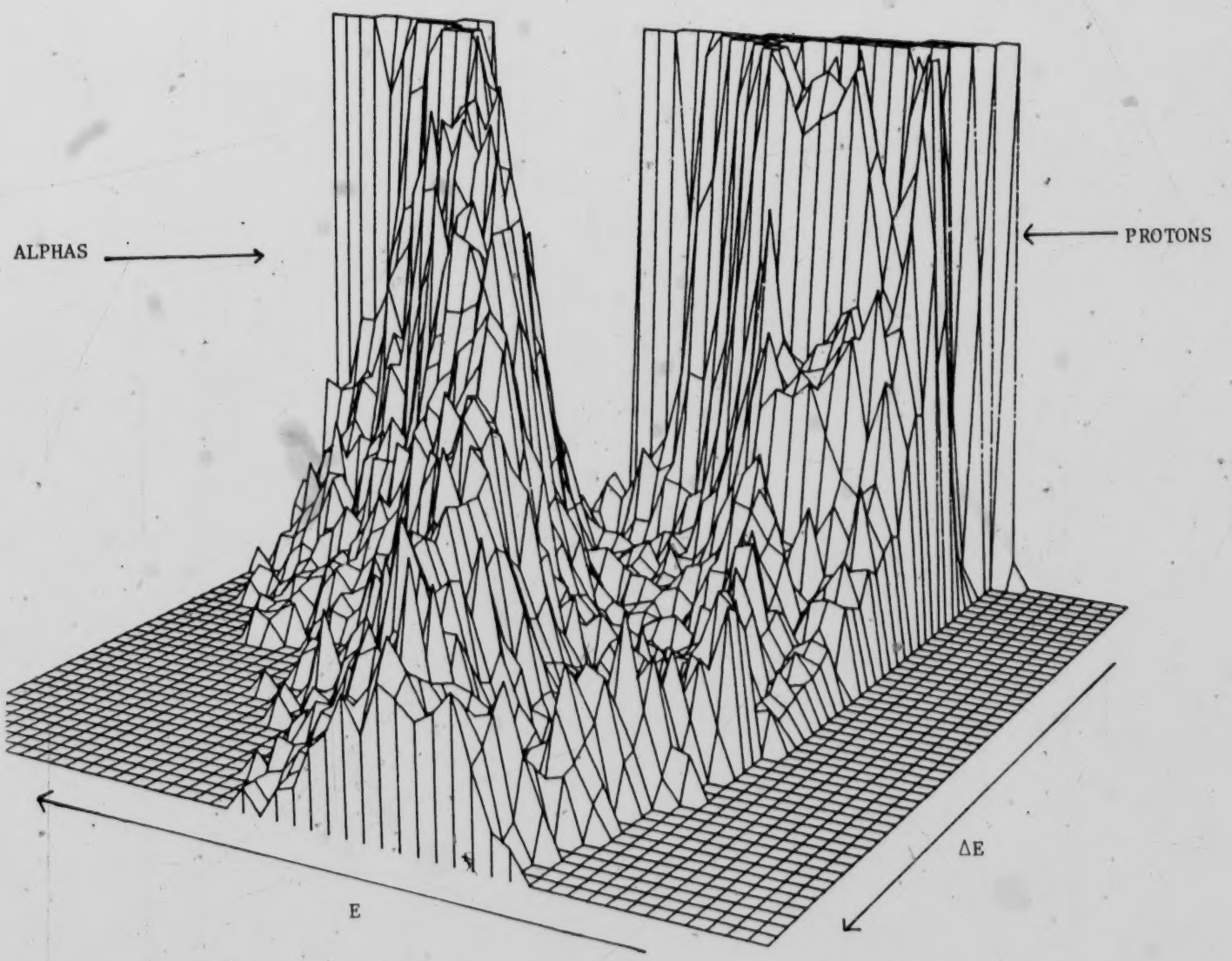
ALPHAS
PROTONS
E
ΔE

FIGURE 3.5

ΔE VERSUS E SPECTRUM FOR α'S

REACTION P + T → α + γ

T_p = 300 MeV

θ_α^{Lab} = 15.3°

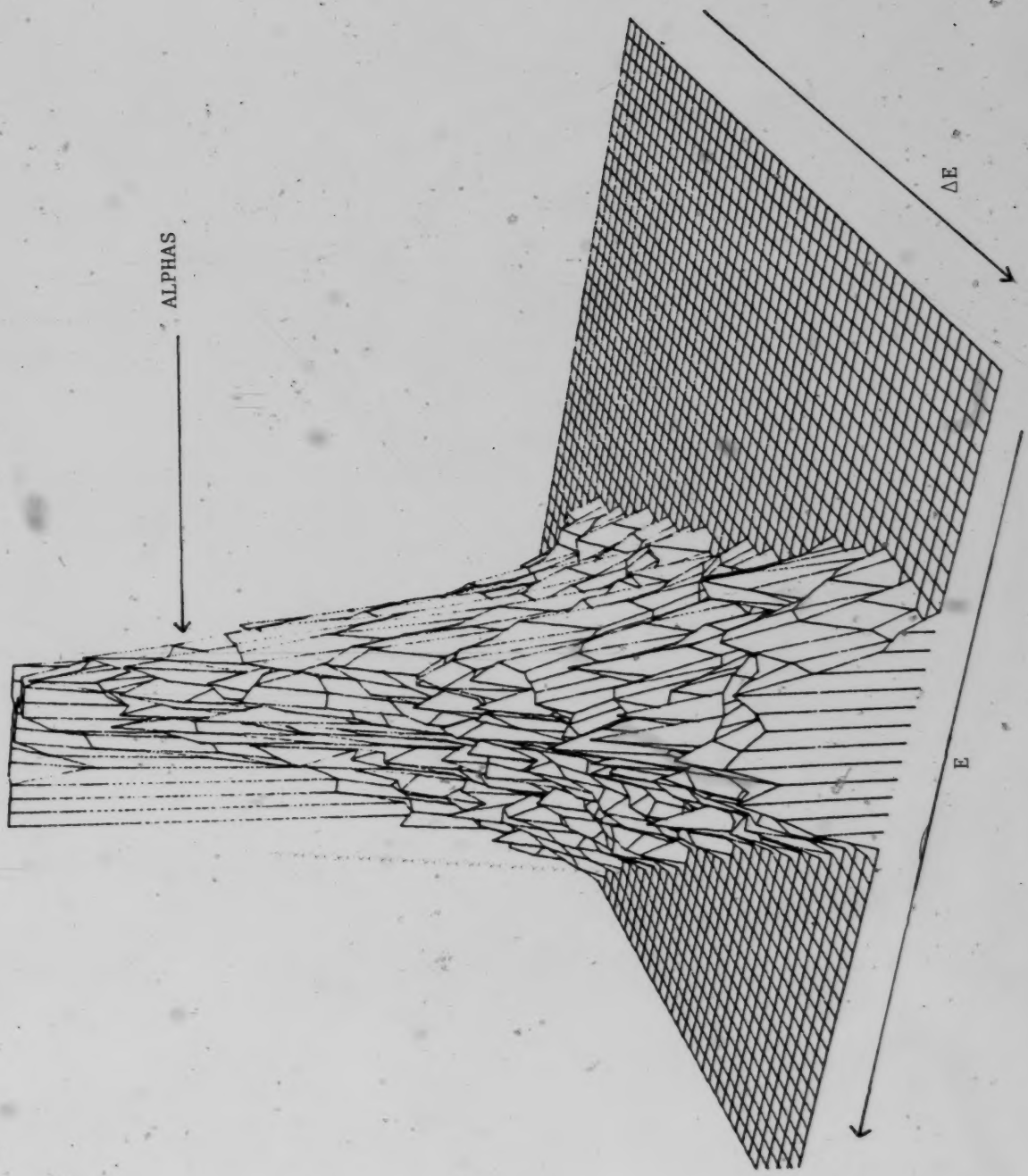
ALPHAS
ΔE
E

FIGURE 3.6

TIME OF FLIGHT VERSUS ENERGY SPECTRUM FOR α'S

REACTION $P + T \rightarrow \alpha + \gamma$

$T_P = 300$ MeV

$\theta_\alpha^{Lab} = 15.3°$

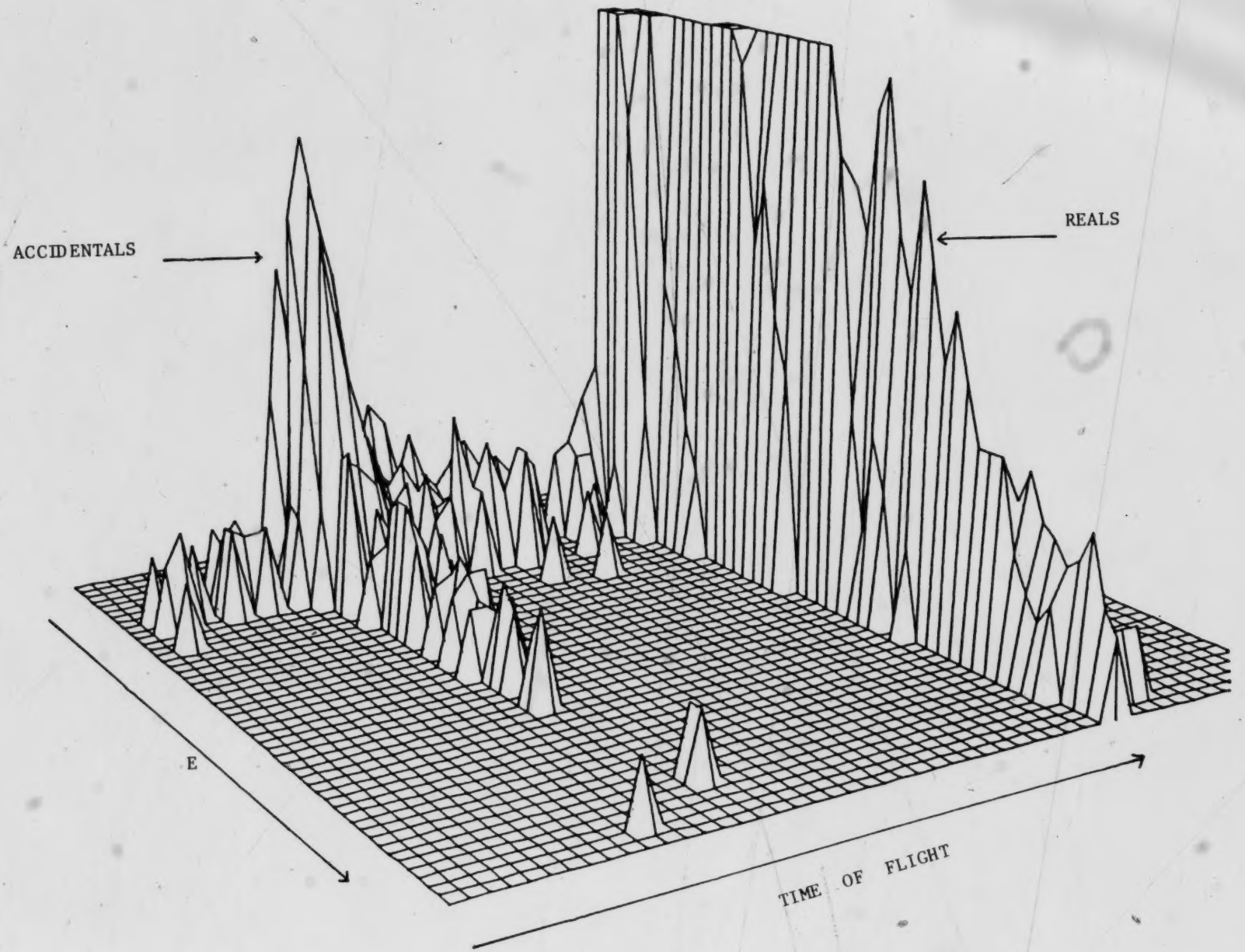
ACCIDENTALS
REALS
E
TIME OF FLIGHT

FIGURE 3.7

PULSE HEIGHT HISTOGRAM OF CHERENKOV COUNTER FOR THE REALS

REACTION $P + T \rightarrow \alpha + \gamma$

$T_P = 300$ MeV

$\theta_\gamma^{Lab} = 78°$

TARGET: TiT

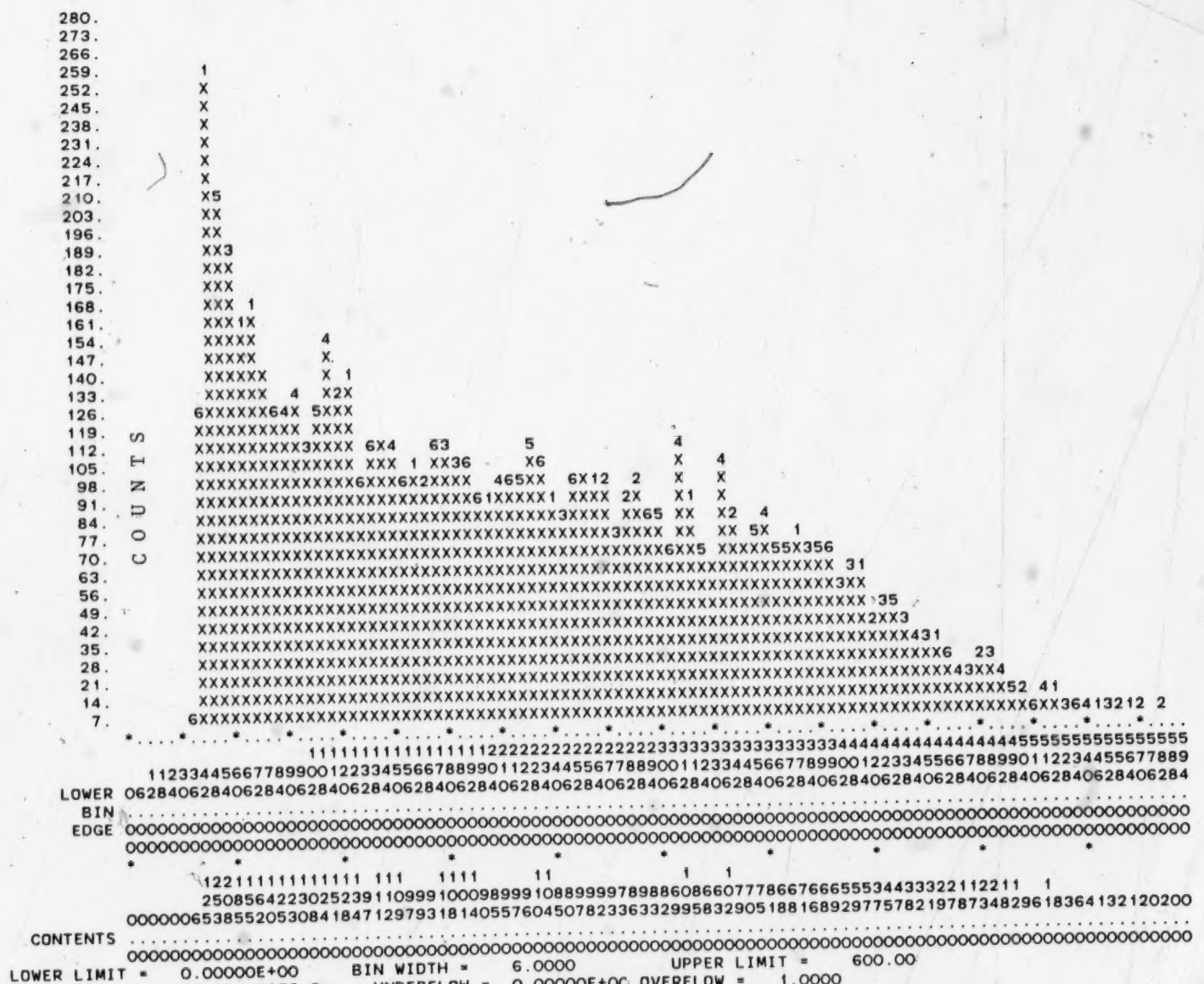
280.
273.
266.
259.
252.
245.
238.
231.
224.
217.
210.
203.
196.
189.
182.
175.
168.
161.
154.
147.
140.
133.
126.
119.
112.
105.
98.
91.
84.
77.
70.
63.
56.
49.
42.
35.
28.
21.
14.
7.
COUNTS
LOWER
BIN
EDGE
CONTENTS
LOWER LIMIT = 0.00000E+00
BIN WIDTH = 6.0000
UPPER LIMIT = 600.00
TOTAL BIN CONTENTS = 6873.0
UNDERFLOW = 0.00000E+00
OVERFLOW = 1.0000
PULSE HEIGHT

FIGURE 3.8

PULSE HEIGHT HISTOGRAM OF CHERENKOV COUNTER FOR THE ACCIDENTALS

REACTION $P + T \rightarrow \alpha + \gamma$

$T_P = 300$ MeV

$\theta_\gamma^{Lab} = 78°$

TARGET: TiT

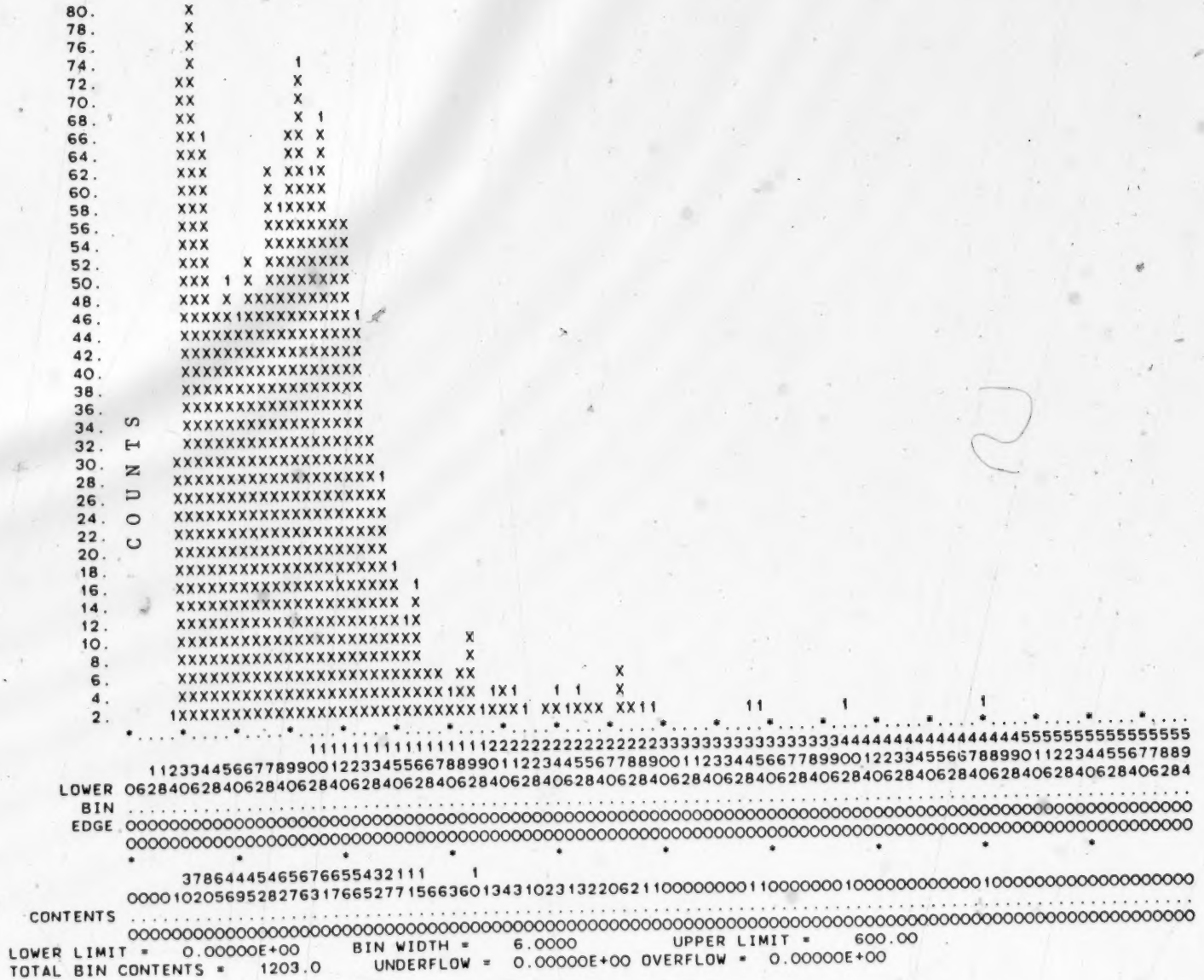
80.
78.
76.
74.
72.
70.
68.
66.
64.
62.
60.
58.
56.
54.
52.
50.
48.
46.
44.
42.
40.
38.
36.
34.
32.
30.
28.
26.
24.
22.
20.
18.
16.
14.
12.
10.
8.
6.
4.
2.
COUNTS
LOWER
BIN
EDGE
CONTENTS
LOWER LIMIT = 0.00000E+00
BIN WIDTH = 6.0000
UPPER LIMIT = 600.00
TOTAL BIN CONTENTS = 1203.0
UNDERFLOW = 0.00000E+00
OVERFLOW = 0.00000E+00
PULSE HEIGHT

height spectrum was accidentals due to general background from the titanium and copper. This was cross-checked by obtaining the corresponding spectra for the titanium run (figs. 3.8a and 3.8b). Consequently, the counts from the initial channels of the Cherenkov pulse height histogram were eliminated so as to obtain clear spectra of ETOT vs scattering angle. This in turn necessitated re-evaluating the Cherenkov counter efficiency because of the change in the threshold. This was done by determining the change in the efficiency due to the software cut on the Cherenkov PH histogram for $d(p,\gamma)^3He$ which we did along with the tritium runs (Appendix D). Fig. 3.9 gives the Cherenkov PH histogram in the case of deuterium at $\theta_\gamma^{CM} = 90°$. The cross section in this case is larger and the counts are more numerous, which helped evaluate the efficiency factor with good statistical precision. Note also that this histogram was obtained with the (p,γ) cut in the energy vs scattering angle histogram and therefore the events were due to γ's only. The vertical line in the histogram represents the pulse height cut made for the tritium case. If N_1 represents the events to the left of the line and N the total events, the efficiency factor involved, η is given by:

$$\eta = \frac{N - N_1}{N} \qquad 3.4.3.1$$

The final step in the analysis was to generate the locus spectrum (ETOT vs recoil angle). Figs. 3.10 and 3.11 represent the

FIGURE 3.8A

PULSE HEIGHT HISTOGRAM OF CHERENKOV COUNTER FOR THE REALS

T_p = 300 MeV

θ_γ^{Lab} = 78°

TARGET: Ti

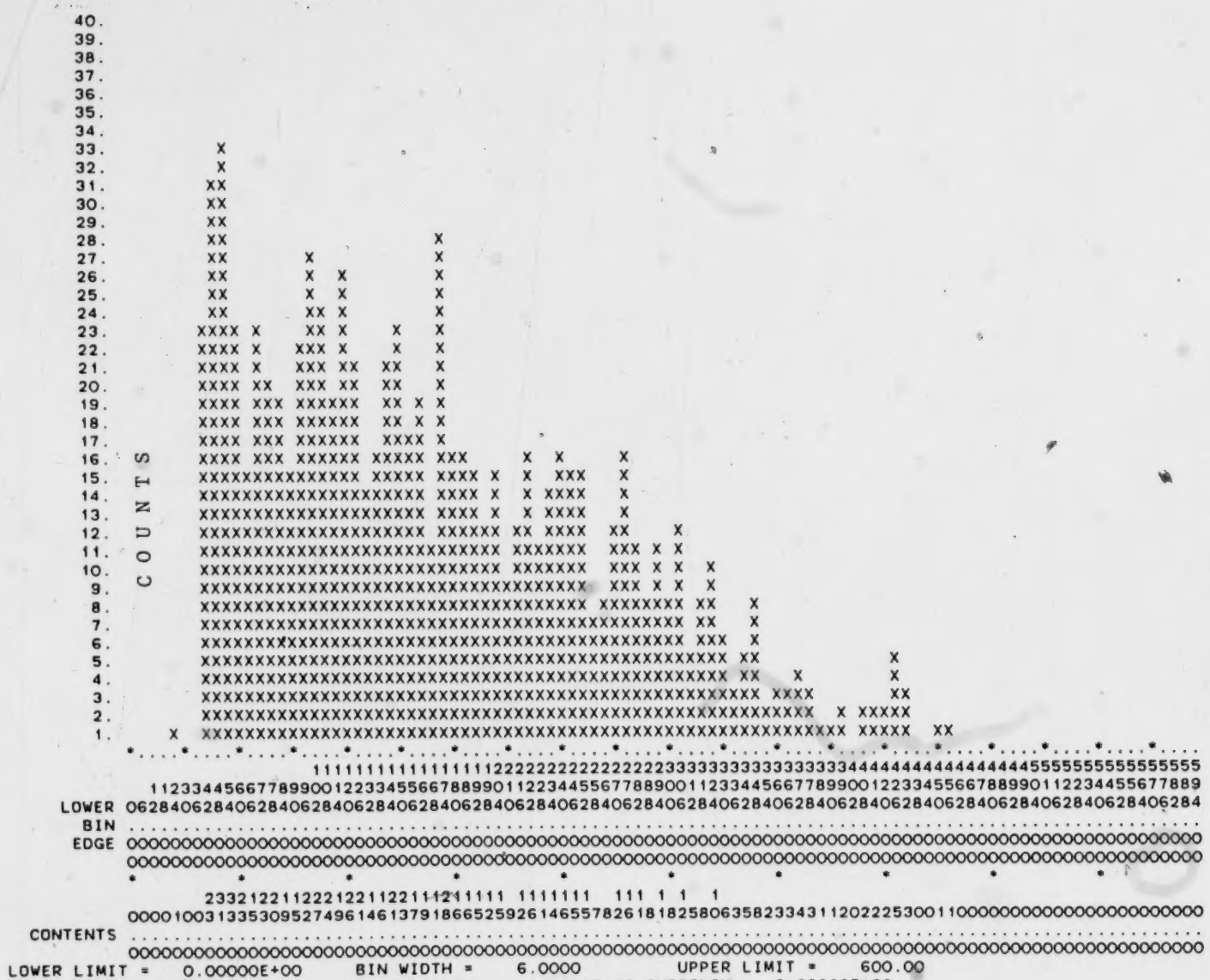
COUNTS
LOWER BIN EDGE
CONTENTS
LOWER LIMIT = 0.00000E+00 BIN WIDTH = 6.0000 UPPER LIMIT = 600.00
TOTAL BIN CONTENTS = 846.00 UNDERFLOW = 0.00000E+00 OVERFLOW = 0.00000E+00
PULSE HEIGHT

FIGURE 3.8B

PULSE HEIGHT HISTOGRAM OF CHERENKOV COUNTER FOR THE ACCIDENTALS

T_p = 300 MeV

θ_γ^{Lab} = 78°

TARGET: Ti

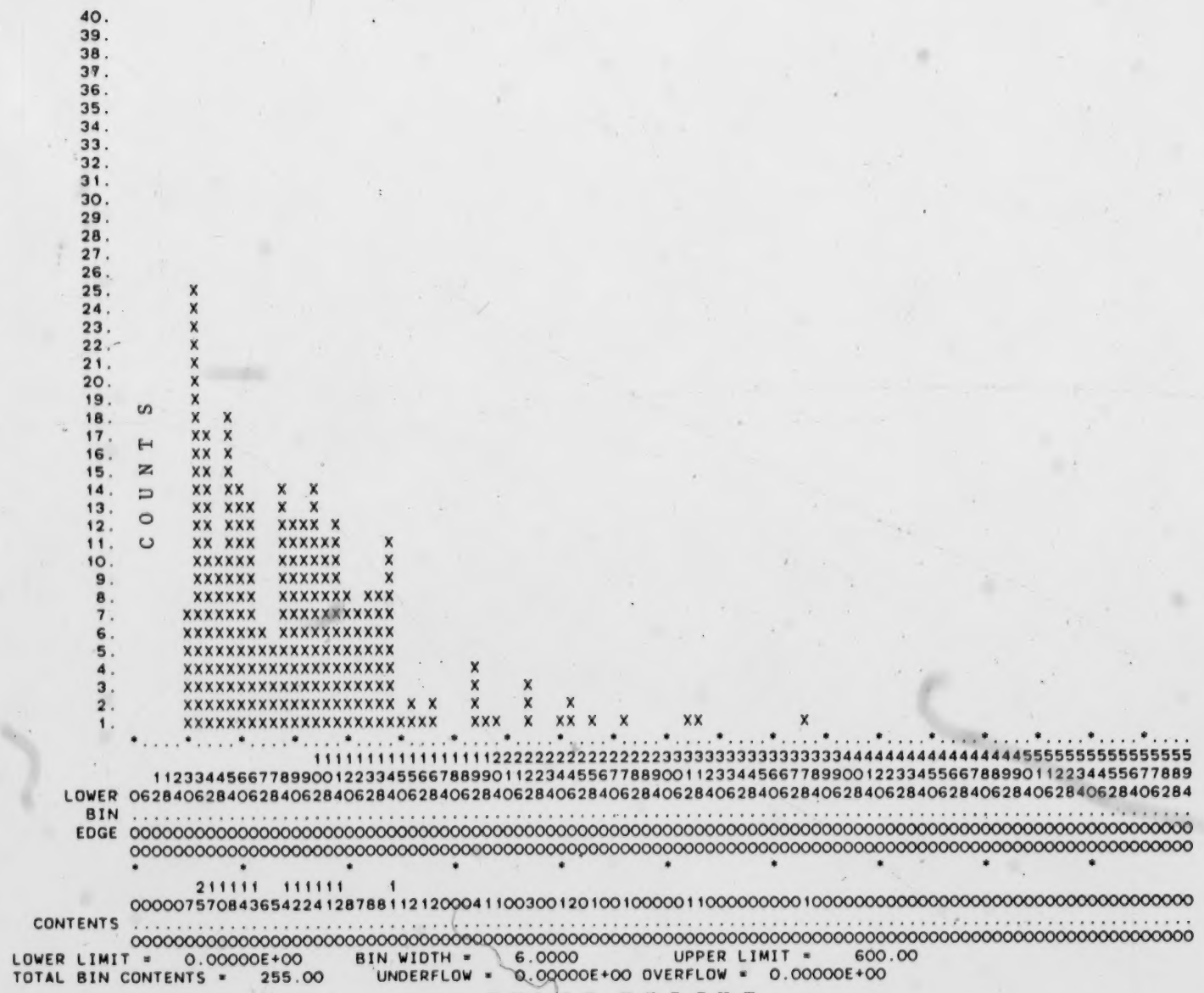
COUNTS
LOWER BIN EDGE
CONTENTS
LOWER LIMIT = 0.00000E+00 BIN WIDTH = 6.0000 UPPER LIMIT = 600.00
TOTAL BIN CONTENTS = 255.00 UNDERFLOW = 0.00000E+00 OVERFLOW = 0.00000E+00
PULSE HEIGHT

FIGURE 3.9

PULSE HEIGHT HISTOGRAM OF CHERENKOV COUNTER FOR THE REALS IN THE REACTION $p + d \rightarrow {}^3He + \gamma$

TARGET: CD_2

$T_p = 300$ MeV

$\theta_\gamma^{Lab} = 75°$

$T_\gamma = 200$ MeV

CARBON BACKGROUND PRESENT

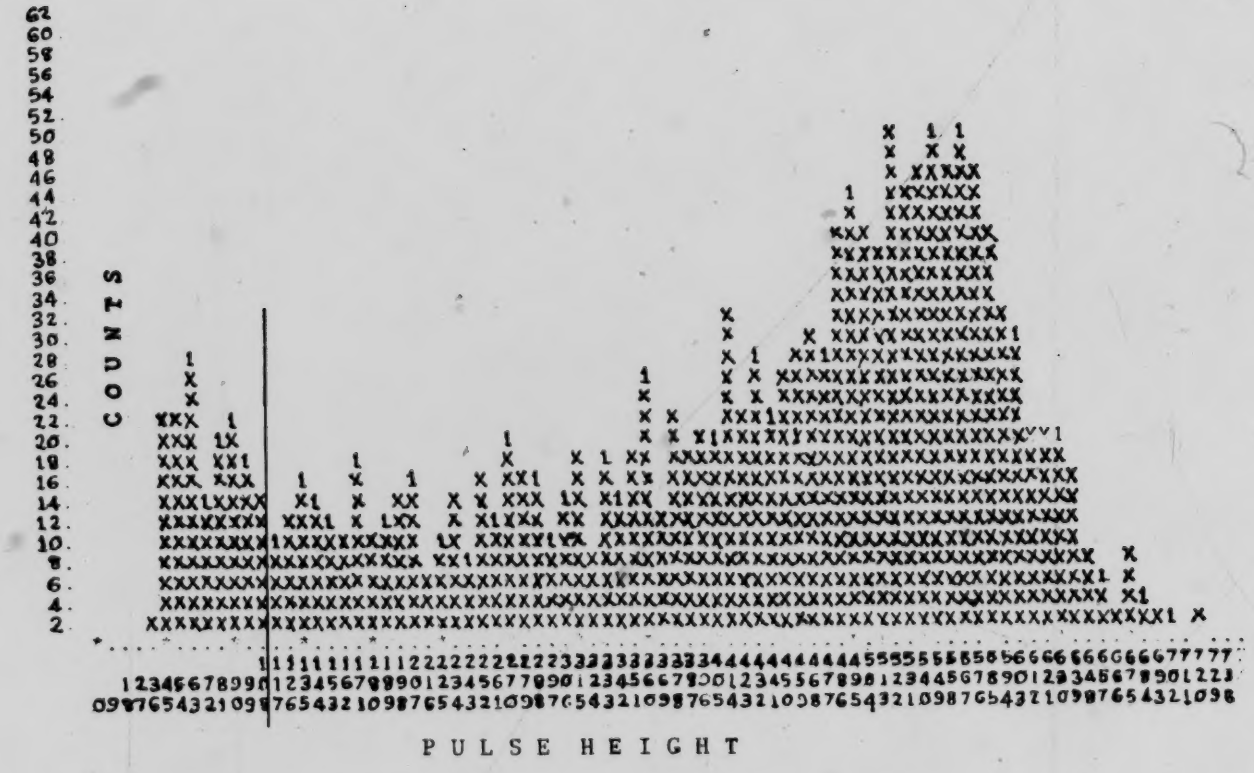
COUNTS
PULSE HEIGHT

FIGURE 3.10

RECOIL ENERGY VERSUS RECOIL ANGLE SPECTRUM

REACTION: $p + T \rightarrow \alpha + \gamma$

$T_p = 300$ MeV

$\theta_\gamma^{lab} = 55°$

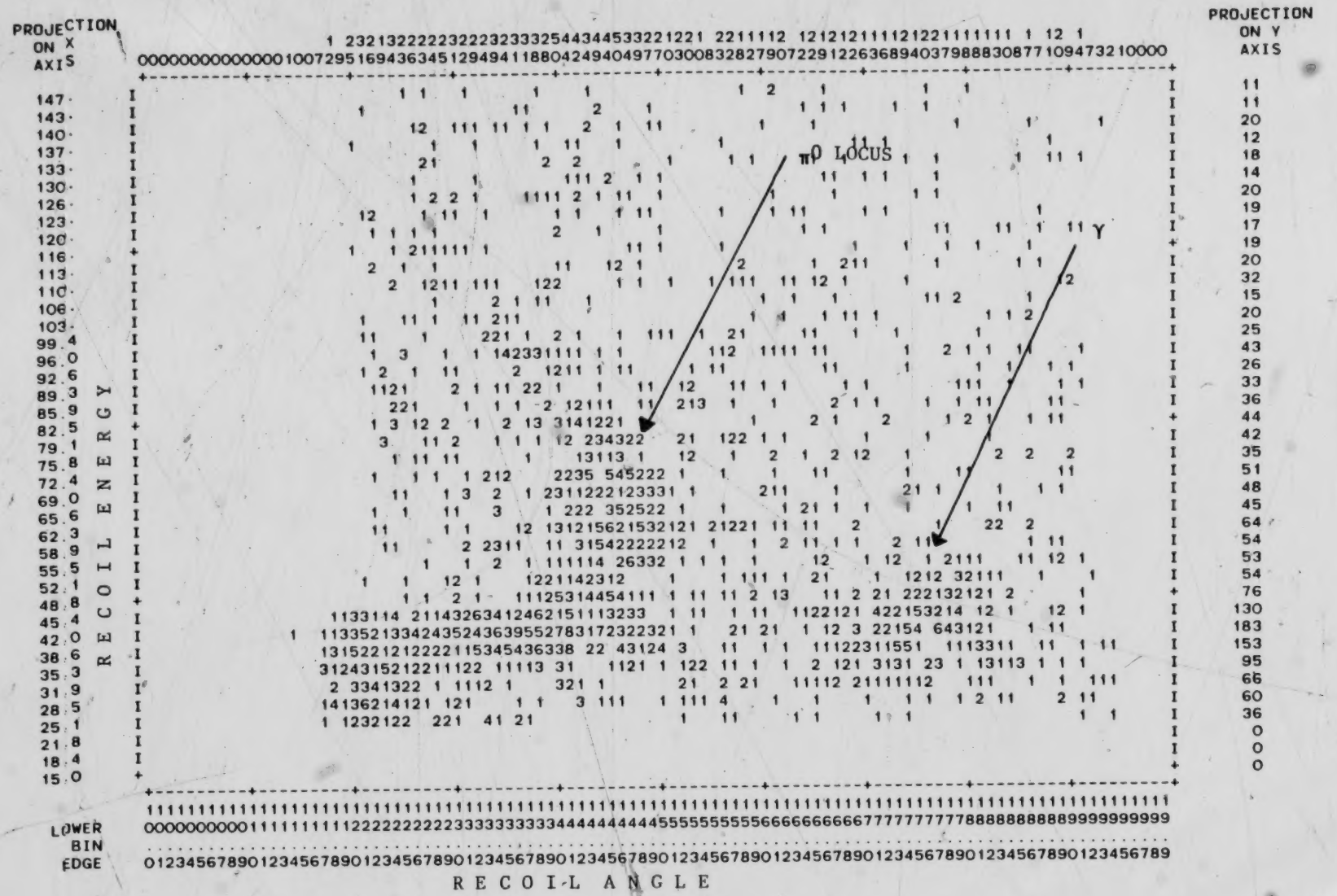
PROJECTION ON X AXIS
PROJECTION ON Y AXIS
πO LOCUS
Y
RECOIL ENERGY
LOWER BIN EDGE
RECOIL ANGLE

FIGURE 3.11

RECOIL ANGLE VERSUS ENERGY SPECTRUM

REACTION: $p + T \rightarrow \alpha + \gamma$

$T_p = 300$ MeV

$\theta_\gamma^{lab} = 15.3°$

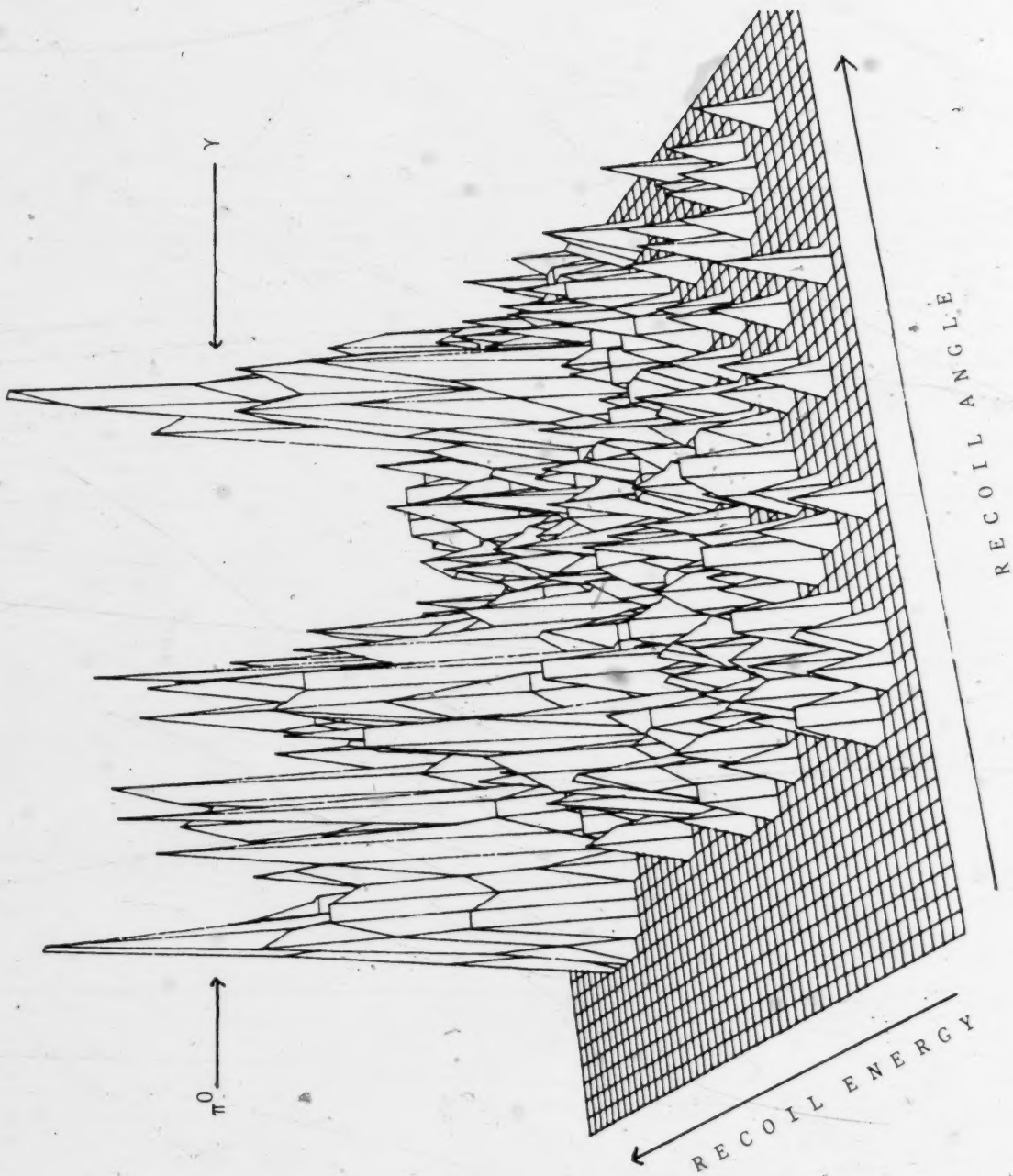
Y
0
RECOIL ANGLE
RECOIL ENERGY

locus spectrum. Clear separation between (p,γ) events and (p,π°) events may be noticed. A kinematic check was made to reaffirm the (p,γ) peak obtained. The Cherenkov counter angular acceptance was calculated from geometry. The corresponding angular region for α's was found from the kinematical correspondence. Again from kinematics, we knew the energy region corresponding to this peak. Since the energy was calibrated in absolute terms as described earlier, we could distinguish the (p,γ) peak from the energy point of view as well. The (p,π°) locus provided additional consistency checks. The kinematical plot (fig. 3.12) illustrates how the (p,π°) locus provided the consistency check.

3.5 THE CROSS-SECTION EVALUATION

The data were analyzed for the TiT runs as well as for the blank titanium runs. Tables 3.5a and 3.5b give typical summaries after analyzing a number of runs and adding up the appropriate counts with proper normalization factors. The program 'XSECT' was written to evaluate the cross section and the analyzing power. The following summarizes the way in which the cross section was evaluated.

3.5.1 The (p,γ) Events

The total number of events corresponding to the (p,γ) reaction were calculated as described earlier. Let that be denoted by 'A'. Note that 'A' was the net contribution. That is, the accidental contribution was subtracted from the reals in arriving at 'A'. Note

FIGURE 3.12

KINEMATICS OF PT→αγ AND PT→απ°

T_p = 300 MeV

G: GAMMA

P: π°

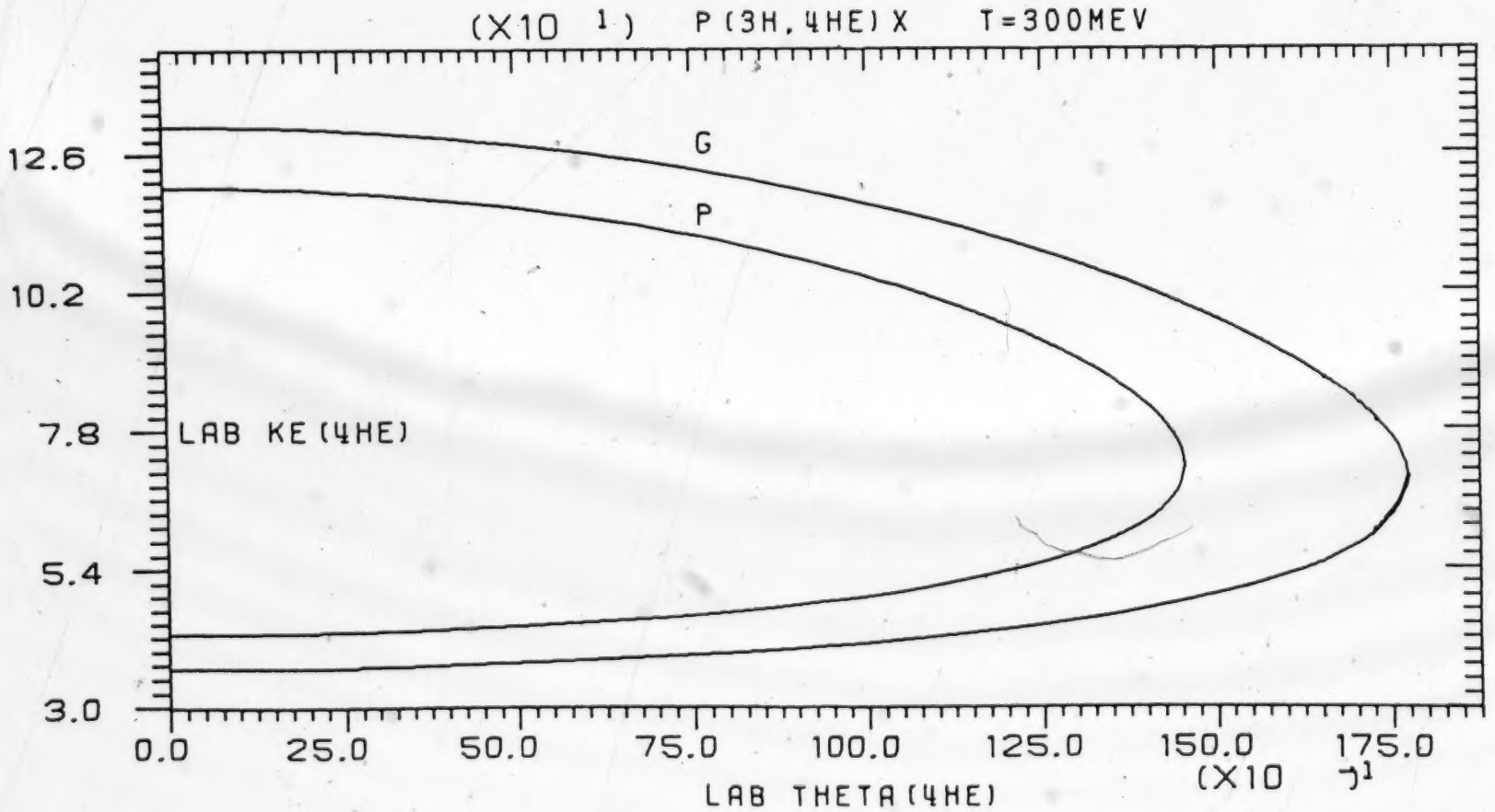
(X10 1) P(3H,4HE)X T=300MEV
G
P
12.6
10.2
7.8
5.4
3.0
LAB KE(4HE)
0.0
25.0
50.0
75.0
100.0
125.0
150.0
175.0
LAB THETA(4HE)
(X10 -1)

TABLE 3.5a

OFF-LINE ANALYSIS OUTPUT - POLARIMETER COUNTS

TARGET	POLARIMETER COUNTS					
	LEFT			RIGHT		
	SPIN UP	SPIN DOWN	SPIN OFF	SPIN UP	SPIN DOWN	SPIN OFF
TiT	73963248 (1928551)	41873708 (950999)	24461808 (633684)	41350880 (934497)	73617136 (1819933)	24307816 (611107)
Ti	29577746 (681173)	17046344 (342670)	24041232 (767857)	16587889 (328604)	29870354 (646987)	23867232 (735271)

No. of incident protons (TiT) = 2.27×10^{15} (up); 2.28×10^{15} (down); 0.96×10^{15} (off).
No. of incident protons (Ti) = 0.91×10^{15} (up); 0.93×10^{15} (down); 0.94×10^{15} (off).

Note: Numbers in parenthesis refer to accidentals.

Angles covered by the run are θ_{γ}^{CM} = 54°, 78°, 99°.

TABLE 3.5b

OFF-LINE ANALYSIS OUTPUT - MWPC AND PULSER INFORMATION

TARGET	MWPC INFORMATION				PULSER INFORMATION		
	LEFT		RIGHT		PULSER	PULSER	SYSTEM
	TOTAL COUNTS	COUNTS-MM	TOTAL COUNTS	COUNTS-MM	PRESENTED	ACCEPTED	LIVETIME
TiT	559068	430293	537215	399022	194359	167611	86%
Ti	252495	173994	216513	147818	79321	60076	76%

MWPC efficiency (TiT) = 77% (LEFT); 74% (RIGHT).

MWPC efficiency (Ti) = 69% (LEFT); 68% (RIGHT).

TABLE 3.5c

OFF-LINE ANALYSIS OUTPUT - (p,γ) EVENTS

LEFT								
L1 ($\theta_\gamma^{CM} = 54°$)			L2 ($\theta_\gamma^{CM} = 78°$)			L3 ($\theta_\gamma^{CM} = 99°$)		
SPIN UP	SPIN DOWN	SPIN OFF	SPIN UP	SPIN DOWN	SPIN OFF	SPIN UP	SPIN DOWN	SPIN OFF
441 ±21	467 ±22	154 ±12	198 ±14	270 ±16	105 ±10	145 ±12	129 ±11	57 ±8

RIGHT								
R1 ($\theta_\gamma^{CM} = 54°$)			R2 ($\theta_\gamma^{CM} = 78°$)			R3 ($\theta_\gamma^{CM} = 99°$)		
SPIN UP	SPIN DOWN	SPIN OFF	SPIN UP	SPIN DOWN	SPIN OFF	SPIN UP	SPIN DOWN	SPIN OFF
519 ±23	406 ±20	182 ±13	231 ±15	170 ±13	110 ±10	154 ±12	162 ±13	76 ±9

also that 'A' refers to the counts in the TiT run. This means that background from Ti was present in 'A'. Later on, we will see how that contribution was subtracted looking at the data for a Ti run.

3.5.2 The Total Beam Current

The total number of protons incident on the target, which generated 'A' events, were taken from the polarimeter data in the trailer block. Eq. 2.8.1 was used to calculate the incident proton count rate.

3.5.3 The Target Thickness

The target thicness was evaluated as described in Appendix A. The thickness of Ti and Cu was the same for the TiT and Ti targets. The tritium thickness is denoted by T_2 and the Ti-Cu thickness by T_1.

3.5.4 The Solid Angle

The solid angle was determined by the Cherenkov counter, since the relative distances of the wire planes and the Cherenkov counters were adjusted such that the Cherenkov counter image was always inside the wire planes. Let 'C' denote the solid angle, A_c the front face area of the counter and d_c its distance from the target.

$$C = \frac{A_c}{{d_c}^2}$$

3.5.5 The Wire Chamber Efficiency

Section 3.3 describes the significance of the wire chamber efficiency. Since there were two planes (x and y) per wire chamber, an efficiency was calculated for the x and y planes. Let the effective efficiency be represented by 'D'.

$$D = \frac{\text{events without 'XMM' •AND• events without 'YMM'}}{\text{Total events}}$$

where 'XMM" refers to the x plane 'multiple' or 'miss' and 'YMM' refers to the y plane multiple or miss.

3.5.6 The Cherenkov Counter Efficiency

The Cherenkov Counter efficiency involved two factors: one is the one described in Appendix C, which was a function of γ energy and the distance of the Cherenkov counter from the target. Let this factor be denoted by E. The other one was a function of the software cut applied to the Cherenkov counter pulse height histogram (section 3.4.3). Let this factor be denoted by F.

3.5.7 The System Live-Time

Section 2.10 describes the significance of system live-time. A major portion of the system dead-time was contributed by the computer processing the event. The rest of it was contributed by the LATCH attached to the EVENT FAST. The overall dead-time was determined making use of a pulser. The pulser was fed to drive the LED's attached to the plastic scintillators and the Cherenkov counter. The pulser pulses were also fed directly, along with the

'E' signal, to an 'OR' gate whose output formed part of the input to the 'AND' gate which determined 'LEFT' or 'RIGHT' 'DCR'. The pulser feed was made proportional to the beam current by setting coincidence between the pulser generator output and the polarimeter 'L+R' output. Pulser pulses presented to the system were scaled and recorded in the trailer block. The pulser event simulated a good event, thus getting recorded as if it was a good event. However pulser 'DCR' demarcated them as pulser events. A typical value of a pulser present was 0.16 M while a total number of 1.12 M events were recorded, of which 3601 represented (p,γ) events of $\theta_{\gamma}^{c.m.} = 54°$ for both sides. The overall system dead-time was a function of the pulser accepted by the system ('DCR' test) and the pulser presented to the system (scaled). If G denotes the system live-time, we have:

$$G = \frac{\text{pulser accepted}}{\text{pulser presented}}$$

3.5.8 The 'TI' Run Parameters

Let A_1 denote the number of events falling in the same software region as for (p,γ) events due to tritium. The number of incident protons are represented by B_1, the target thickness by T_1, the solid angle (same as the one for the tritium run) by C, the wire chamber efficiency by D_1, the Cherenkov efficiency factors by E and F (same as the ones for the tritium run), and the system live-time by G_1.

3.5.9 Extraction of Events Due to Tritium and Cross Section Calculation

Of the total number of events A, not all stand for events due to tritium. Letting A' denote the number of events due to Ti-Cu, we have:

$$A' = A_1 \cdot \frac{B \cdot D \cdot G}{B_1 \cdot D_1 \cdot G_1} \qquad 3.5.9.1$$

The number of events due to tritium alone is denoted by A_T

$$A_T = A - A' \qquad 3.5.9.2$$

The differential cross-section x is given by:

$$x = \frac{A_T}{B \cdot T_2' \cdot C \cdot D \cdot E \cdot F \cdot G} \text{ barns/steradian} \qquad 3.5.9.3$$

where T_2' is the number of tritium nuclei/cm^2 of the target.

3.6 THE STATISTICAL UNCERTAINTY IN THE CROSS-SECTION VALUE

The standard deviation in the value of x may be obtained from eq. 3.5.9.3.

$$\sigma_x = x \left[\frac{A + \sigma_{A'}^2}{A_T^2} + \frac{1}{B} + \frac{1}{d} + \frac{1}{e} + \frac{1}{g} + \frac{1}{h} \right]^{1/2} \qquad 3.6.1$$

where $D = \frac{d}{e}$ and $G = \frac{g}{h}$.

3.7 THE ANALYZING POWER EVALUATION

When we followed the method described above after splitting the total events into contributions due to spin up and spin down, we got the spin-dependent cross sections. This was done for both the 'LEFT' side and 'RIGHT' side. The analyzing power was evaluated from these cross sections. Let AP represent the analyzing power.

$$AP = \frac{1}{\bar{P}} \left[\frac{X_{L\uparrow} - X_{L\downarrow} + X_{R\downarrow} - X_{R\uparrow}}{X_{L\uparrow} + X_{L\downarrow} + X_{R\downarrow} + X_{R\uparrow}} \right] \qquad 3.7.1$$

where $X_{L\uparrow}$ etc. are differential cross-sections for LEFT, SPIN UP etc., and $\bar{P}$ is the average beam polarization given by:

$$\bar{P} = \frac{P_U I_U + |P_D| I_D}{I_U + I_D} \qquad 3.7.2$$

where $P_U(P_D)$ is the beam up (down) polarization given by eq. 2.8.2. $I_U(I_D)$ are the beam intensities for up (down) polarization. The variance in the analyzing power is given by:

$$\sigma_{AP}^2 = \frac{1}{\bar{P}^2} (AP)^2 \sigma_{\bar{P}}^2 + \frac{4}{\bar{P}^2 (m+n+r+s)^4}$$

$$\{(n+s)^2 (\sigma_m^2 + \sigma_\gamma^2) + (m+r)^2 (\sigma_n^2 + \sigma_s^2)\} \qquad 3.7.3$$

where $m = \sigma_{L\uparrow}$, $n = \sigma_{L\downarrow}$, $r = \sigma_{R\downarrow}$, $s = \sigma_{R\uparrow}$ ($\sigma_{L\uparrow}$ etc. refer to the standard deviation in $X_{L\uparrow}$ etc.) and

$$\sigma_{\bar{P}}^2 = \frac{1}{(I_U+I_D)^2}(I_U^2\,\sigma_{P_U}^2 + I_D^2\,\sigma_{P_D}^2)$$

$$+ \frac{(P_U-P_D)^2}{(I_U+I_D)^4}\,(I_D^2\,\sigma_{IU}^2 + I_U^2\,\sigma_{ID}^2) \qquad 3.7.4$$

substituting eq. 3.7.4 in eq. 3.7.3 we obtained the standard deviation in the analyzing power.

CHAPTER 4

RESULTS AND CONCLUSIONS

4.1 THE RESULTS

The experimental results for the differential cross section and the analyzing power are tabulated in table 4.1 The errors quoted represent only the statistical uncertainty. These are in the range from 6% to 40% for cross section and 9% to 48% for analyzing power.

The results were converted to cross section values for the inverse reaction, using the principle of detailed balance, at the corresponding incident γ energy determined by the conservation of total CM energy. Table 4.2 gives the results for the inverse reaction. This conversion was done so that the results could be compared with the existing inverse reaction cross section values (Arg-75, Pic-70, Are-79, Sch-83, Kie-73). These correspond to data from SACLAY, FRASCATI, BONN, MIT, and ILLINOIS respectively. Results were also compared with forward reaction cross section values from Did-70 (ORSAY).

The results are plotted in Fig. 4.1 to 4.3a. Fig. 4.1 gives the angular distribution of the cross section at γ-energy T_γ = 246 MeV. The results are shown along with other data for comparison. Figs. 4.2, 4.2a, and 4.2b give the excitation function including the data from six other groups. Fig. 4.3 gives the analyzing power values of T_p = 300 MeV.

There is fairly good agreement between the results of the present experiment and the results of other groups with the exception of those of Frascati and Illinois. This agreement

TABLE 4.1

EXPERIMENTAL RESULTS FOR CROSS SECTION AND ANALYZING POWER

INCIDENT PROTON ENERGY (MEV)	θ_γ^{CM}	$\frac{d\sigma}{d\Omega}^{CM}$ (nb/sr)	ANALYZING POWER
227	90	31.91 ± 2.21	0.1167 ± 0.0888
300	54	64.62 ± 3.78	0.1050 ± 0.0971
300	65	49.93 ± 3.10	0.1180 ± 0.0888
300	78	22.36 ± 1.69	0.4355 ± 0.1301
300	90	16.32 ± 1.77	0.0337 ± 0.0305
300	99	7.69 ± 1.50	-0.6272 ± 0.3010
300	118	4.94 ± 1.98	-0.5842 ± 0.3210
375	60	37.69 ± 4.42	0.4090 ± 0.2222
375	91	14.34 ± 3.23	-0.6147 ± 0.3564

TABLE 4.2

CROSS SECTION VALUES CONVERTED USING DETAILED BALANCE

INCIDENT GAMMA ENERGY (MEV)	θ_P^{CM}	$\frac{d\sigma}{d\Omega}^{CM}$ (nb/sr)
191	90	474.8 ± 32.8
246	54	786.8 ± 46.0
246	65	608.0 ± 37.8
246	78	272.2 ± 20.5
246	90	198.7 ± 21.6
246	99	83.6 ± 18.3
246	118	60.2 ± 24.1
302	60	395.1 ± 46.2
302	91	150.3 ± 33.8

FIGURE 4.1

ANGULAR DISTRIBUTION OF CROSS-SECTION AT T_γ = 246 MEV

REACTION; $\gamma + \alpha \rightarrow P + T$

+	BONN
×	SACLAY
▲	MIT
■	PRESENT WORK

A: DWIA CALCULATION; DISTORTION NOT INCLUDED; TRITON WAVEFUNCTION: CORRELATED GAUSSIAN.

B: DWIA CALCULATION; DISTORTION INCLUDED; TRITON WAVEFUNCTION: CORRELATED GAUSSIAN.

C: DWIA CALCULATION; DISTORTION NOT INCLUDED; TRITON WAVEFUNCTION: CORRELATED EXPONENTIAL.

D: DWIA CALCULATION; DISTROTION INCLUDED; TRITON WAVEFUNCTION: CORRELATED EXPONENTIAL.

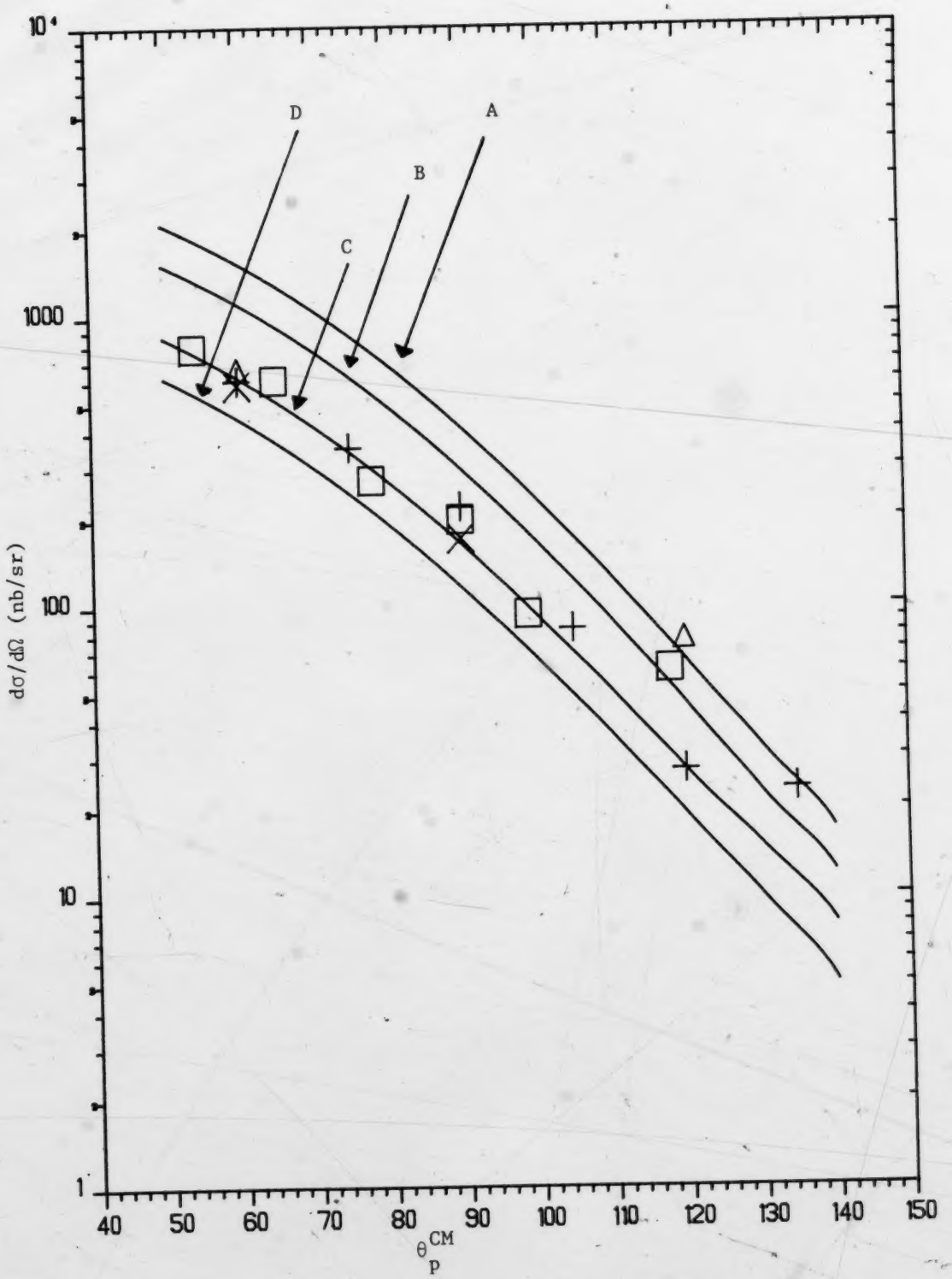
10⁴
1000
100
10
1
dσ/dΩ (nb/sr)
D
A
B
C
40
50
60
70
80
90
100
110
120
130
140
150
θ CM p

FIGURE 4.2

COMPARISON OF EXCITATION FUNCTIONS FOR RADIATIVE CAPTURE AND ITS INVERSE REACTION

REACTION; $\gamma + \alpha \rightarrow P + T$

+	BONN
×	SACLAY
▲	MIT
■	PRESENT WORK
O	ORSAY
I	ILLINOIS, FRASCATTI

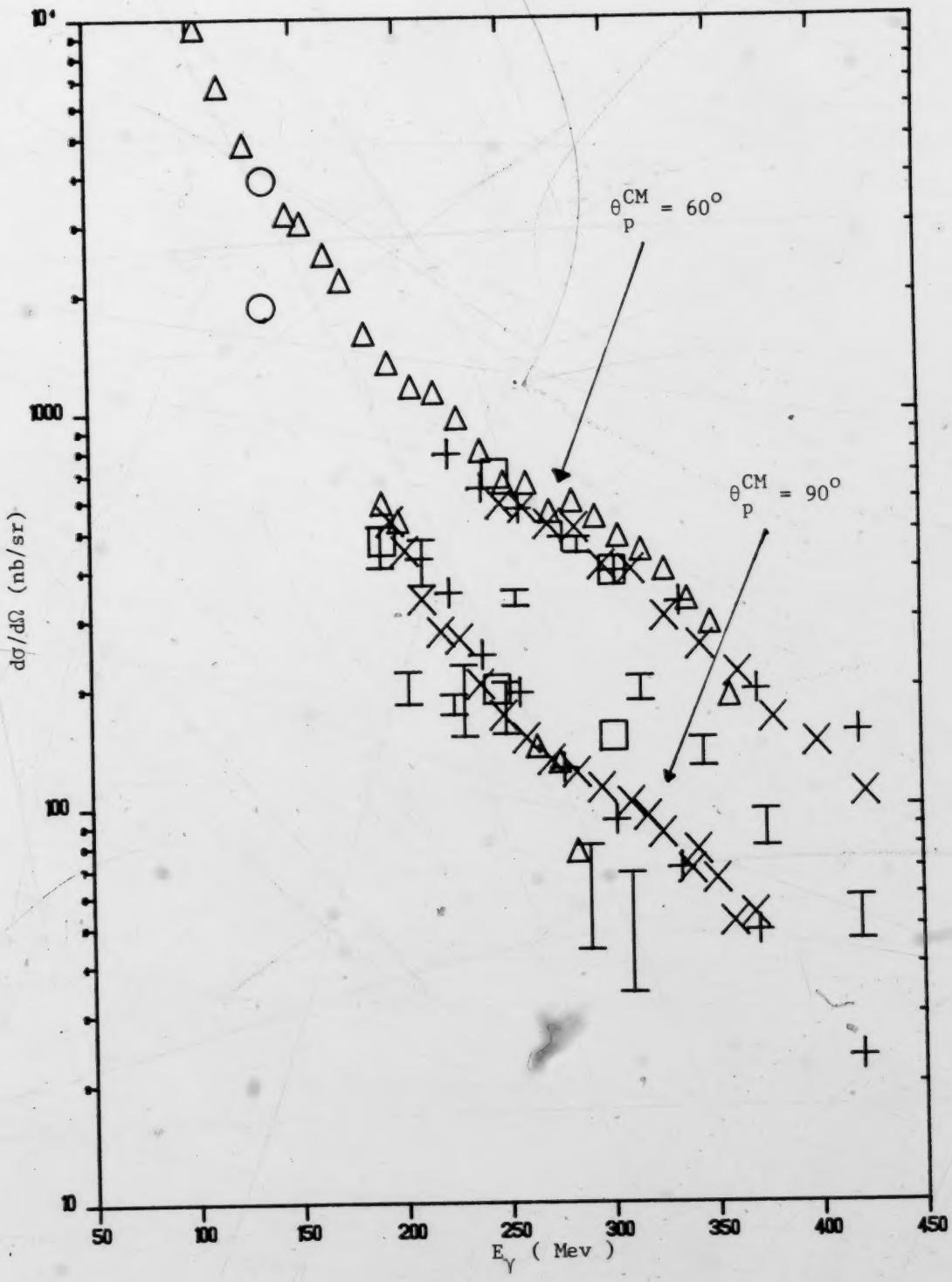
10^4
1000
100
10
$d\sigma/d\Omega$ (nb/sr)
$\theta_p^{CM} = 60^o$
$\theta_p^{CM} = 90^o$
50
100
150
200
250
300
350
400
450
E_γ (Mev)

FIGURE 4.2A

COMPARISON OF EXCITATION FUNCTION AT 60° CM WITH THE DWIA CALCULATION

REACTION; $\gamma + \alpha \rightarrow P + T$

+	BONN
×	SACLAY
▲	MIT
■	PRESENT WORK
O	ORSAY

WAVE FUNCTION USED: CORRELATED EXPONENTIAL

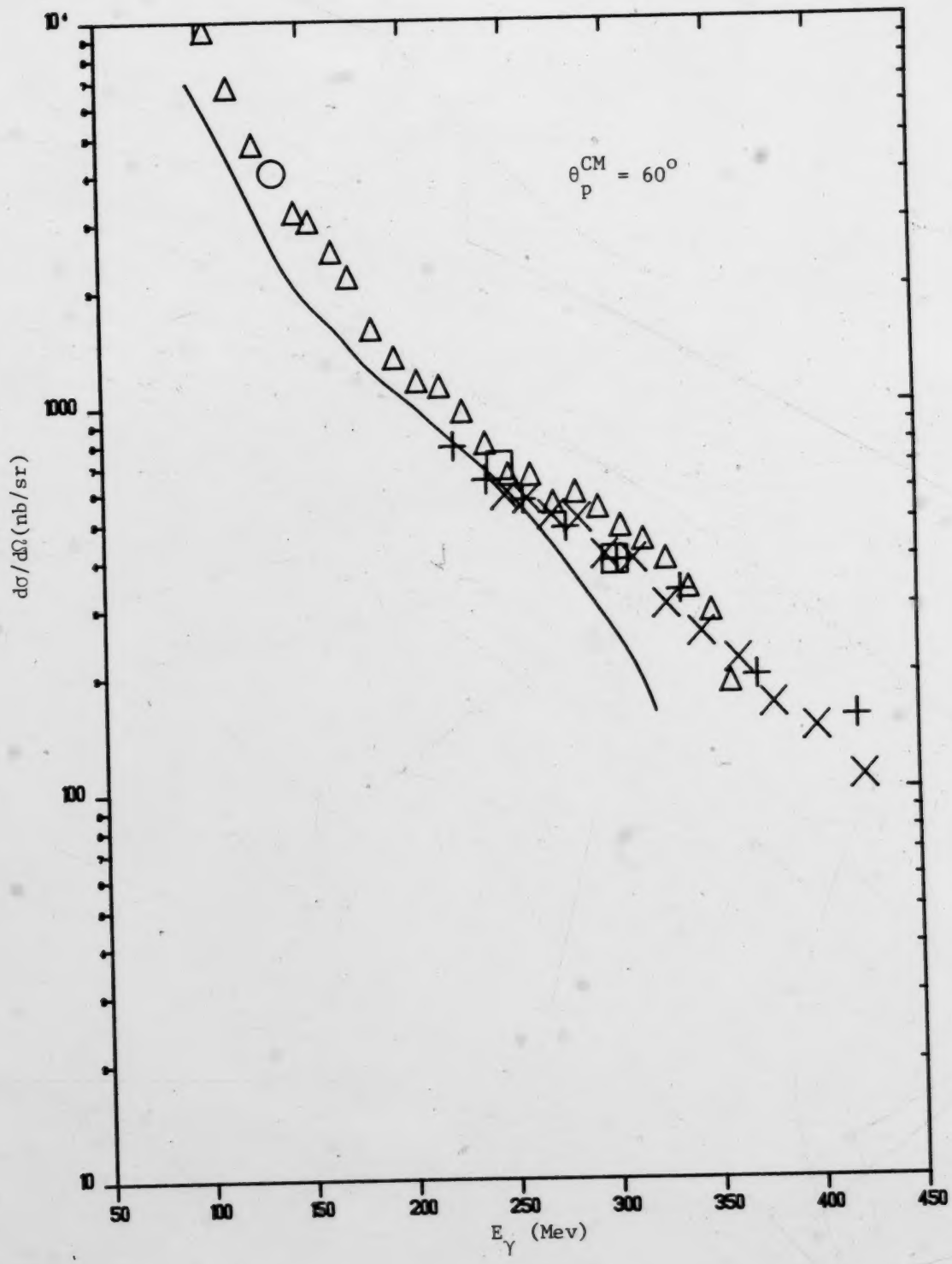
10^4
1000
100
10
$d\sigma/d\Omega$(nb/sr)
$\theta_p^{CM} = 60^o$
50
100
150
200
250
300
350
400
450
E_γ (Mev)

FIGURE 4.2B

COMPARISON OF EXCITATION FUNCTION AT 90° CM WITH THE DWIA CALCULATION

REACTION; $\gamma + \alpha \rightarrow P + T$

+	BONN
×	SACLAY
▲	MIT
■	PRESENT WORK
O	ORSAY
I	ILLINOIS, FRASCATI

WAVE FUNCTION USED: CORRELATED EXPONENTIAL

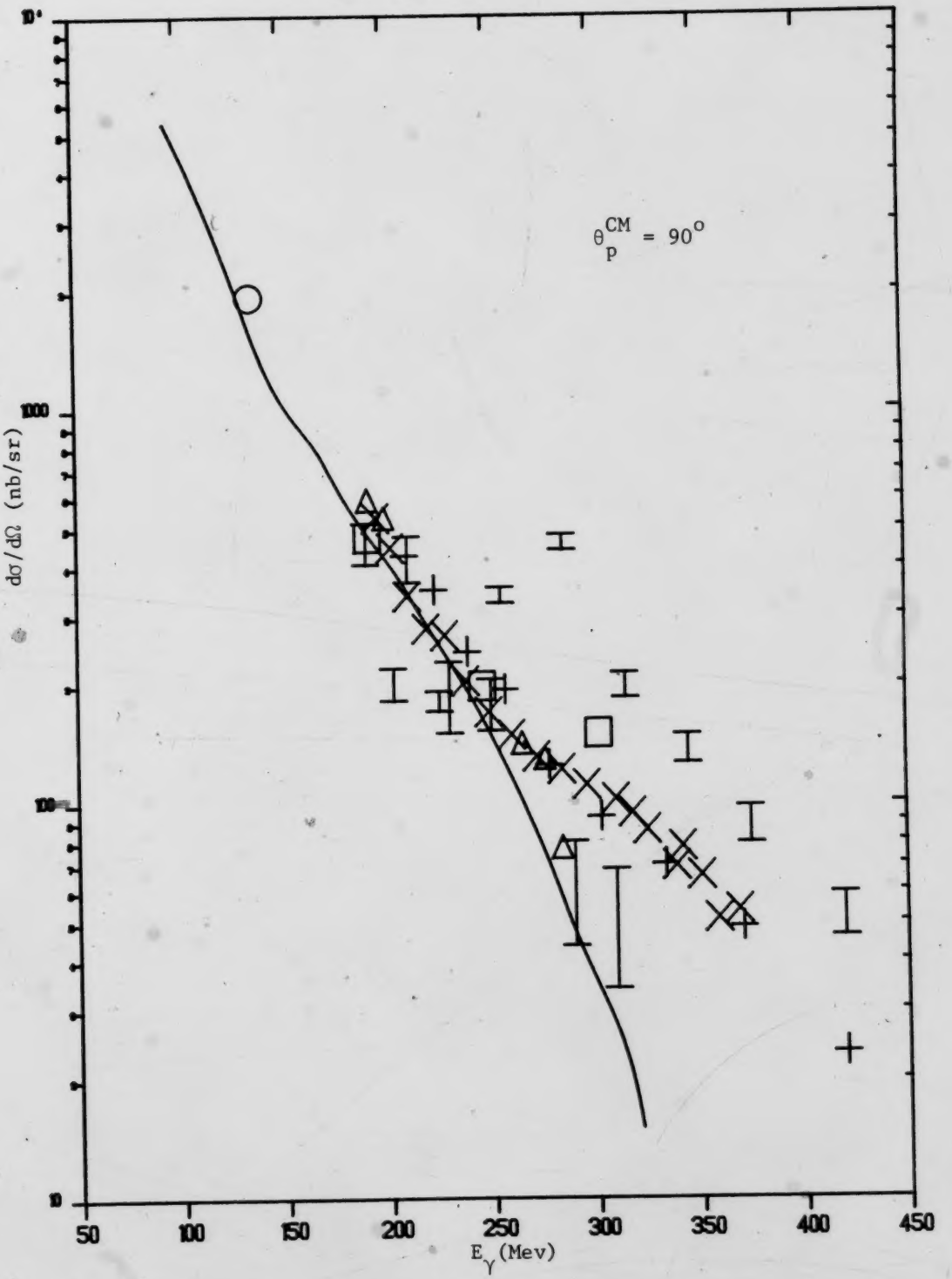
$\theta_p^{CM} = 90^o$
dσ/dΩ (nb/sr)
E_γ(Mev)
10
100
1000
50
100
150
200
250
300
350
400
450

FIGURE 4.3

ANALYZING POWER DISTRIBUTION FOR THE REACTION P + T → α + γ AT

T_P = 300 MEV

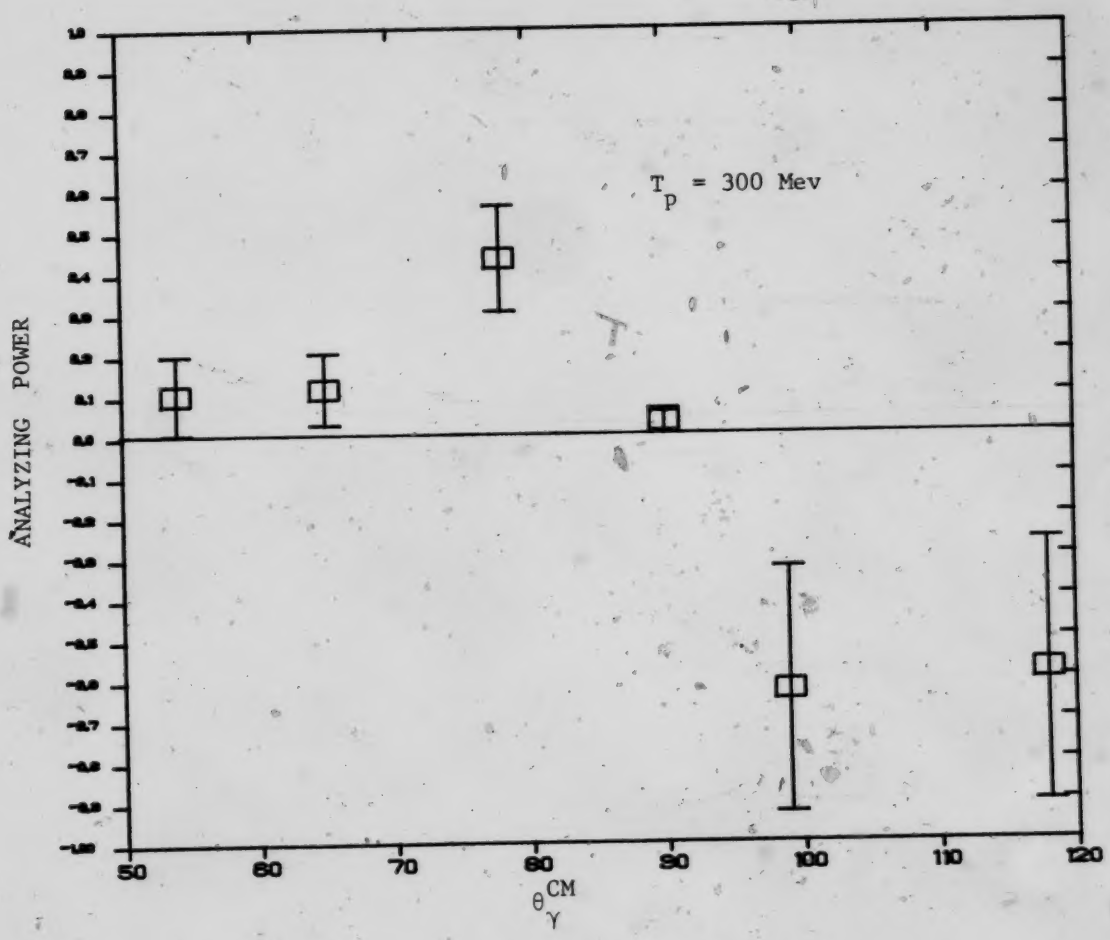
T_p = 300 Mev
ANALYZING POWER
50
60
70
80
90
100
110
120
θ_γ^{CM}

FIGURE 4.3A

COMPARISON OF EXCITATION FUNCTION AT 60° CM WITH GARI AND HEBACH'S CALCULATION

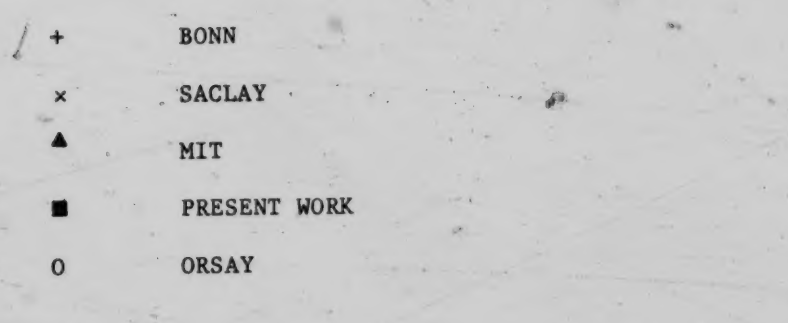

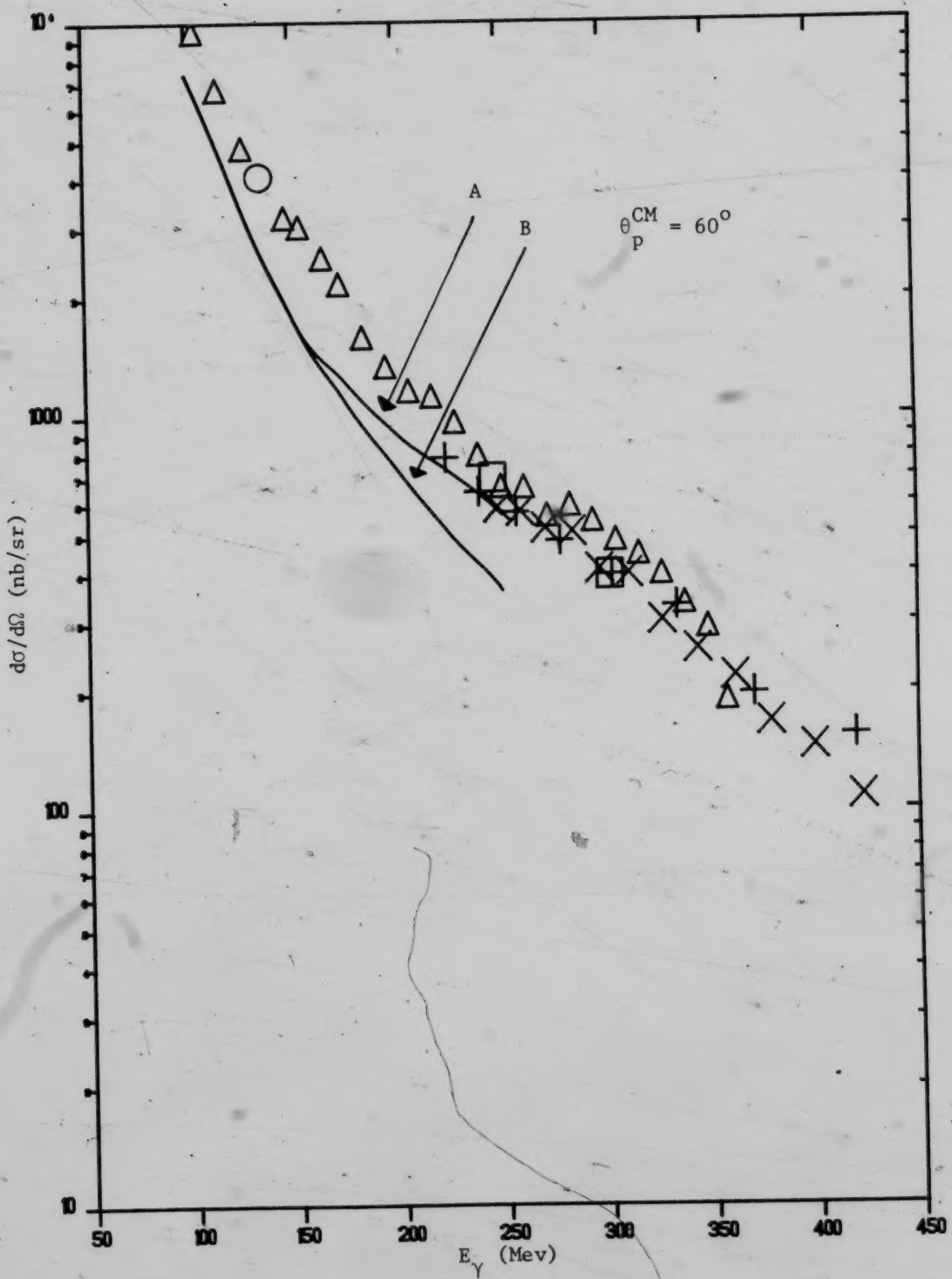
10⁴
1000
100
10
dσ/dΩ (nb/sr)
A
B
$\theta_p^{CM} = 60^o$
50
100
150
200
250
300
350
400
450
E_γ (Mev)

indicates that time reversal is not violated in the electromagnetic interaction of hadrons. This aspect is discussed later.

Figs. 4.1, 4.2a and 4.2b also give theoretical curves for the cross section values, calculated in the Distorted Wave Impulse Approximation (DWIA). This is discussed in the next section.

4.2 DISTORTED WAVE IMPULSE APPROXIMATION (DWIA)

The calculations performed are based upon the quasi-deuteron model first proposed by Levinger (Lev-51). This model considered the total nuclear wavefunction as the product of the wavefunction for two nucleons very close together and the wavefunction for the remaining nucleons. The remaining nucleons provided a potential in which the deuteron moves and they scatter the high energy nucleons of the deuteron. The wavefunction for the A-nucleon system was expressed as a product of three terms: the first term representing the motion of center of mass of the quasi-deuteron, the second term representing the wavefunction of the quasideuteron, and the third term representing the wavefunctions of the A-2 nucleus.

$$\Psi(1,\ 2,\ \ldots A) = \exp\left(i\vec{k}' \cdot \vec{r}'\right)\ \psi_k(r)\ \phi(3,\ \ldots A) \qquad (4.1)$$

where Ψ is the total wavefunction, $\exp(i\vec{k}' \cdot \vec{r}')$ stands for the motion of the center of mass of the deuteron, $\psi_k(r)$ stands for the quasideuteron wavefunction and ϕ stands for the wavefunction of the remaining A-2 nucleons. The wavenumber for the relative motion of proton and neutron is represented by k and the internucleon distance

is represented by r. The cross section for the photonuclear process was obtained in terms of the cross-section for the photodisintegration of the quasideuteron, given the velocity v_x of the quasideuteron in the direction of observation and v_y in the perpendicular direction. A proton observed at an energy T outside the nucleus is scattered at an energy T' by the quasideuteron. The same proton, observed at an angle θ is scattered at an angle θ' by the quasideuteron. The differential cross section as a function of T, was given by:

$$d\sigma(T) = \int d\sigma(T') \frac{dT'}{dT} P(v_x)\, dv_x \qquad (4.2)$$

where $P(v_x)$ is the distribution function for the velocity component v_x.

The differential cross section as a function of angle was given by:

$$d\sigma(\theta) = \int d\sigma(\theta') \frac{\sin \theta'}{\sin \theta} P(v_y)\, dv_y \qquad (4.3)$$

where $P(v_y)$ is the distribution function for the velocity component v_y.

This method, with modifications, was applied to calculate the cross section for the reaction $pd \rightarrow t\pi^+$ by Ruderman (Rud-52). In this approach the cross section was calculated in terms of the cross section for the primary reaction $PP \rightarrow d\pi^+$. The neutron in the

deuterium acts as a spectator. The triton wavefunction was expressed in terms of the deuteron wavefunction on the assumption that the neutron and proton that participated directly in the production of the triton are very close. Thus the following expression for the cross section (Blu-54) was obtained:

$$\frac{d\sigma}{d\Omega}(Pd \rightarrow t\pi^+) = \frac{1}{v_{Pd}} [f(\theta)]^2 \frac{1}{3} \frac{E_t}{E_\pi + E_t} \left[v_{PP} \frac{E_\pi + E_d}{E_d} \frac{d\sigma}{d\Omega} (PP \rightarrow d\pi^+) \right] \tag{4.4}$$

where v's are the relative velocities and E's the total energies in the CM frame. The quantities inside the square brackets were evaluated in the CM system of the two protons. The energy of the proton was determined for producing a meson of momentum $\vec{q}$. The quantity $f(\theta)$ is the form factor, given by:

$$f(\theta) = \int \psi_D(\vec{x}) \exp\left(i \frac{\vec{\Delta} \cdot \vec{x}}{\hbar}\right) \frac{\psi_T(0,\vec{x})}{\psi_D(0)} d\vec{x} \tag{4.5}$$

where ψ_D and ψ_T are the deuteron and triton wavefunctions, $\vec{x}$ the neutron-proton relative co-ordinate and $\vec{\Delta} = \frac{1}{2}\vec{k} - \frac{1}{3}\vec{q}$. The momentum of the incident proton is given by $\vec{k}$.

This model was modified by Fearing to incorporate distortion in the initial and final channels (Fea-74, Fea-75a) and to include a better treatment of wavefunctions. The model was extended to

include the reaction Pd → ^{3}He γ (Fea-75b), with the difference that there is no outgoing wave distortion. Described below are the main features of the model and the calculations done in the present work to get the cross section for P + T → γ + ^{4}He using DWIA.

4.3 SALIENT FEATURES OF FEARING'S DWIA MODEL

The cross section for the reaction P + T → ^{4}He + γ could be expressed as a product of the cross section for the sub-process P + n → d + γ, a kinematic factor, a spin-isospin-antisymmetrisation factor, and a form factor.

$$\left(\frac{d\sigma}{d\Omega}\right)^{P+T\rightarrow\gamma+\alpha}_{PTcm} = KF \cdot g \cdot |F(\Delta)|^2 \left(\frac{d\sigma}{d\Omega}\right)^{P+n\rightarrow\gamma+d}_{Pn\ cm} \qquad (4.6)$$

where KF is the kinematical factor, g the spin factor, and F(Δ) the form factor.

$$KF = \frac{E_T\ E_\alpha\ P_\gamma}{E_q\ E_d\ P_p} \left(\frac{P}{P_\gamma}\right)_{pn\ cm} \qquad (4.7)$$

where E's and P's are the energy and momentum in the PT cm frame.

Eq. refers to the target neutron:

$$E_q = (q^2 + m_n^2)^{1/2} \qquad (4.8)$$

$$E_d = E_p + E_q - E_\gamma \qquad (4.9)$$

'q' is the effective momentum involved, determined by taking into account the fact that the sub-process takes place off-mass-shell.

The spin factor is given by:

$$g = \frac{\overline{\Sigma}_{\text{spins}} \left| \sum_{\beta_d \beta_0 \beta_1} \langle \beta_d | T_{01} | \beta_0 \beta_1 \rangle \langle \alpha_\alpha | \beta_d \rangle \langle \beta_0 \beta_1 | \alpha_p \alpha_T \rangle \right|^2}{\overline{\Sigma}_{\text{spins}} |\langle \beta_d | T_{01} | \beta_0 \beta_1 \rangle|^2} \tag{4.10}$$

where β's refer to the spin-isospin wavefunctions of those involved in the process $pn \rightarrow d\gamma$, 0 refers to the incoming proton, 1 to the neutron, and α's refer to spin-isospin wavefunctions of those involved in the process $PT \rightarrow \gamma\alpha$. Both the numerator and the denominator are calculated by summing over the final spins and averaging over the initial spins. T_{01} is the two-body T-matrix. The value of g for the reaction $P + T \rightarrow \gamma + {}^4He$, was calculated and found to be equal to 1/18.

The form factor is given by:

$$F(\Delta) = \frac{2}{\sqrt{3}} \left[\int d^3y'_0 \, d^3y'_1 \, d^3y_2 \, d^3y_3 \, \delta^3(y_2 + y_3) \, e^{i\Delta \cdot y_1} \right.$$

$$F_{pT}(x_0, v_{pT}) \, F_{pn}(0, v_{pn}) \, \phi^*_\alpha(y'_0, y'_1, y_2, y_3)$$

$$\left. \Phi_d(y'_0 - y'_1) \, \Phi_T(y_1, y_2, y_3) \right] \tag{4.11}$$

where unprimed and primed quantities stand for those before and after the collision. If r_0, r_1, r_2, r_3 represent the co-ordinates of the initial four nucleons and r'_0, r'_1, r'_2, r'_3 those of the final four nucleons, then $y_i = r_i - R_s$ and $y'_i = r'_i - R_s$ where R_s is the center of mass of the spectator nucleons n and p. $\Delta = \frac{1}{2}(P_p - \frac{P_T}{3} - P_\gamma)_{PT\ cm}$ is known as the effective momentum transfer. $x_0 = r_0 - R_T$ where R_T is the triton c.m. co-ordinate. V_{PT} is the relative velocity between proton and triton and v_{pn} that between proton and neutron. Φ's are antisymmetric wavefunctions. The F's are the distortion functions which are measures of the deviation of the scattering waves from plane waves. F is found by integrating the scattering potential along the projectile path. The potential, in turn, is expressed in terms of the nuclear density function, the forward scattering amplitude and the total cross section for p-p elastic scattering and p-n elastic scattering.

$$F(x,v) = \exp\left\{\frac{i}{2}\left[\sigma_p(\eta_p + i) + 2\sigma_n(\eta_n + i)\right]\int_0^\alpha \rho(x - v\tau)d\tau\right. \qquad (4.12)$$

where σ_p is the total cross section for p-p scattering, and σ_n is the total cross section for p-n scattering. η_p is the ratio of the real

to imaginary parts of the forward amplitude for p-p scattering and η_n the analogous quantity for p-n scattering. The charge density function is represented by ρ. It is given by the following equation:

$$\rho(r) = \frac{\rho_o}{1 + e^{(r-R)/a}} \qquad (4.13)$$

where ρ_o is the central density, 'a' the skin thickness and 'R' the radius obtained from the electron scattering data. The central density is given by:

$$\rho_o = \frac{3}{4\pi (R^3 + \pi^2 a^2 R)} \qquad (4.14)$$

4.4 THE WAVEFUNCTIONS OF d, t AND α

The form factor evaluation requires knowledge of the wavefunctions of the deuteron, triton and alpha (eq. 4.11). The Hulthen wavefunction (Fea-75a) was used for the deuteron. The Hulthen deuteron wavefunction is given below.

$$\phi_d(\vec{x}_1,\vec{x}_2) = N_d \left[\frac{e^{-\beta|\vec{x}_1-\vec{x}_2|} - e^{-\gamma|\vec{x}_1-\vec{x}_2|}}{|\vec{x}_1-\vec{x}_2|} \right] \qquad (4.15)$$

where $N_d = 9.8\ \text{MeV}^{1/2}$

$\beta = 45$ MeV

$\gamma = 270$ MeV.

A correlated Gaussian wave function (Fea-77) was used for the triton. The following is the functional form.

$$\phi_t(\vec{x}_0,\vec{x}_1,\vec{x}_2) = N_t\, e^{-\alpha^2 u}\left[1 - C\exp(-\beta^2|\vec{x}_0-\vec{x}_1|^2)\right]$$

$$\times\left[1 - C\exp(-\beta^2|\vec{x}_0-\vec{x}_2|^2)\right]\left[1 - C\exp(-\beta^2|\vec{x}_1-\vec{x}_2|^2)\right] \qquad (4.16)$$

where $u = |\vec{x}_0-\vec{x}_1|^2 + |\vec{x}_1-\vec{x}_2|^2 + |\vec{x}_0-\vec{x}_2|^2$,

$N_t = 1.83 \times 10^6\ \text{MeV}^3$,

$\alpha = 62.8$ MeV,

$\beta = 232$ MeV, and

$C = 0.925$.

A correlated exponential wavefunction was also used for triton. The form is as given below:.

$$\phi_3(\vec{x}_0,\vec{x}_1,\vec{x}_2) = N_t\, e^{-\alpha w}\left[1 - C\exp(-\beta^2|\vec{x}_0-\vec{x}_1|^2)\right]$$

$$\times\left[1 - C\exp(-\beta^2|\vec{x}_0-\vec{x}_2|^2)\right]\left[1 - C\exp(-\beta^2|\vec{x}_1-\vec{x}_2|^2)\right]$$

where $w = |\vec{x}_0-\vec{x}_1| + |\vec{x}_1-\vec{x}_2| + |\vec{x}_0-\vec{x}_2|$.

A correlated Gaussian function was used for ^{4}He, which is given below:

$$\phi_d(\vec{x}_0,\vec{x}_1,\vec{x}_2,\vec{x}_3) = N_\alpha e^{-\beta^2 u}[1 - C\exp(-\gamma^2|\vec{x}_0-\vec{x}_1|^2)]$$

$$\times [1 - C\exp(-\gamma^2|\vec{x}_0-\vec{x}_2|^2)][1 - C\exp(-\gamma^2|\vec{x}_0-\vec{x}_3|^2)]$$

$$\times [1 - C\exp(-\gamma^2|\vec{x}_1-\vec{x}_2|^2)][1 - C\exp(-\gamma^2|\vec{x}_1-\vec{x}_3|^2)] \qquad (4.17)$$

$$\times [1 - C\exp(\gamma^2|\vec{x}_2-\vec{x}_3|^2)]$$

where $N_\alpha = 9.55 \times 10^4$ MeV^3, $\beta = 166$ MeV, and $\gamma = 615$ MeV.

Taking a close look at eqn. 4.11 it may be seen that the form factor is the fourier transform with respect to the momentum transfer of the overlap of the triton and α wavefunctions with the deuteron wavefunction, modified by the PT and Pn distortion function. This means that in order to have an appreciable cross section, there has to be a good amount of overlap between the intermediate deuteron and final state nuclear wavefunctions, a condition which is satisfied for low-mass nuclei.

4.5 DATA FOR THE REACTION P + n → γ + d

This section elaborates on the last term in eq. 4.6, namely the experimental cross section values used for the reaction P + n → γ + d. Reaction amplitudes for the reaction P + n → γ + d can be substituted for the interaction vertex, thereby eliminating the ambiguities associated with the Single Nucleon Model (SNM) and the Two Nucleon Model (TNM). In the SNM, the proton emits a γ and then is captured by the triton to form ^{4}He. The entire momentum

transfer is taken up by a single nucleon, thereby involving high momentum components of the wavefunction, which are not yet understood properly. In the TNM, the incoming proton shares its momentum with one nucleon of the triton either in the process of quasideuteron formation or Δ isobar production. Here momentum transfer is shared by two nucleons, which eliminates the need for high momentum components.

The experimental cross section value for $\gamma + d \rightarrow P + n$ has been measured recently with high precision over a wide energy range by four groups (Cra-82, Are-84, Bab-83, Dou-76). These data come from MIT, BONN, TOKYO and LUND respectively. Taken as a whole, these data sets cover an energy range of E_γ = 100 MeV to 832 MeV over an angular range of θ_p^{CM} = 15° to 160°. The values from LUND below 300 MeV have been discarded.

Fig. 4.4 gives a plot of these data as angular distributions of the cross section for various incident γ energies. Plotted also are the fitted curves at appropriate energies. Fitting was done taking s cros section values from all the groups. The cross section values at a particular energy were fitted to a polynomial of the form given below:

$$\frac{d\sigma}{d\Omega}(E_\gamma) = a_0 + a_1 \cos\theta_{PCM} + a_2 \cos^2\theta_{PCM} + a_3 \cos^3\theta_{PCM} \qquad (4.18)$$

where a's are the parameters to be determined and θ_{PCM} is the proton scattering angle in the CM frame. Fitting the data to the polynomial

FIGURE 4.4

ANGULAR DISTRIBUTION OF CROSS SECTION FOR $\gamma + d \rightarrow p + n$ AND THE FITTED CURVE

DATA ARE TAKEN FROM (CRA-82), (ARE-84), (BAB-83), (DOU-76)

I, CURVE A: 200 MEV

×, CURVE B: 340 MEV

▲ , CURVE C: 400 MEV

■ , CURVE D: 440 MEV

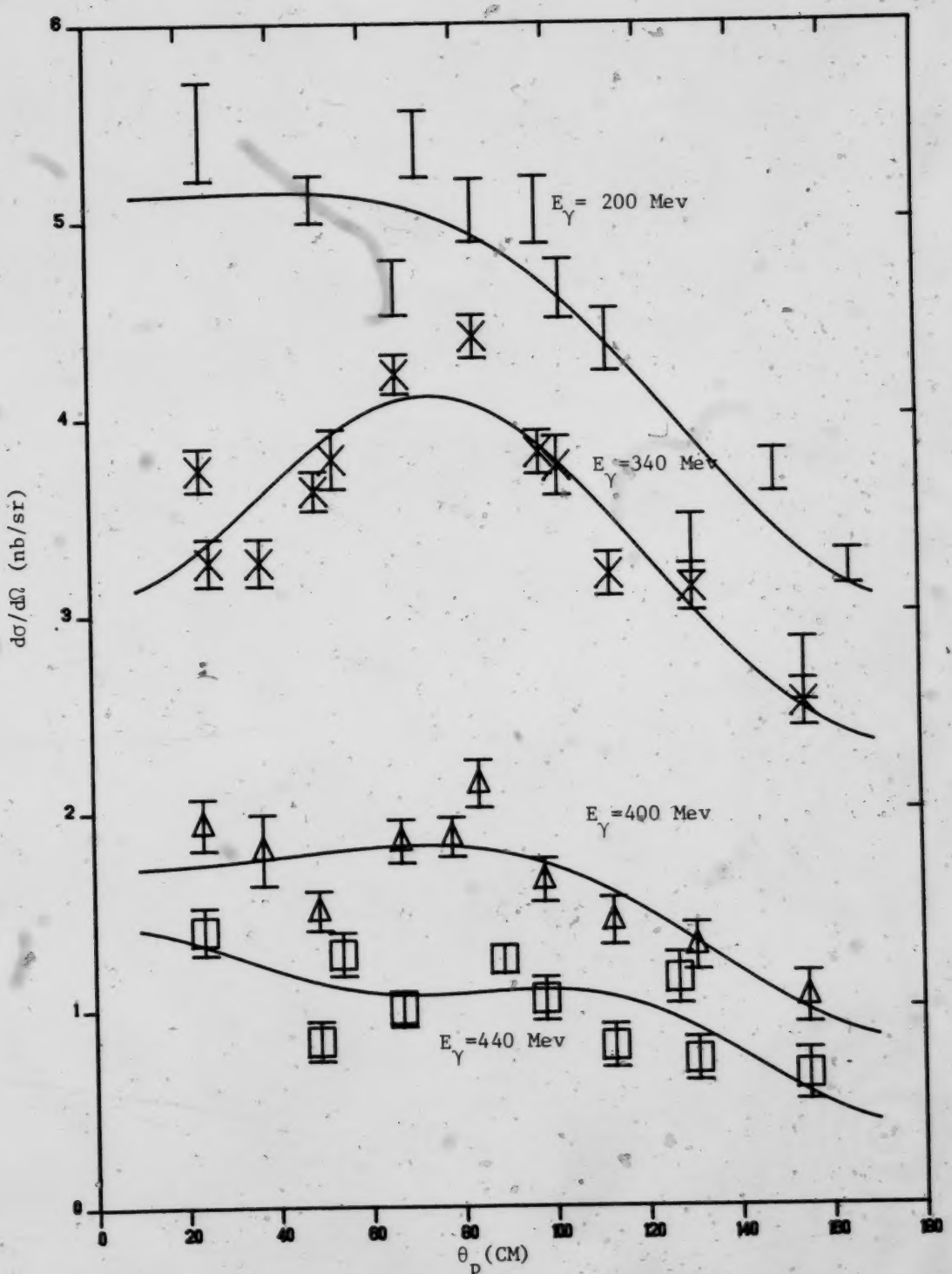
E_γ = 200 Mev
E_γ =340 Mev
E_γ =400 Mev
E_γ =440 Mev
dσ/dΩ (nb/sr)
θ_p (CM)
0
1
2
3
4
5
6
0
20
40
60
80
100
120
140
160
180

(4.18) was done for a set of energies and the values of 'a' were generated as a function of E_γ. Table 4.3 gives the coefficients of the polynomial thus generated.

These coefficients were then fitted as a function of energy. The following functional forms were used.

$$a_0 = c01 \exp(-c02 \cdot x) + \frac{c03 - c04 \cdot x}{1 + \left(\frac{x - c05}{c06}\right)^5} \qquad (4.19)$$

$$\frac{a_1}{a_0} = c11 - c12 \cdot x + c13 \cdot x^2 \qquad (4.20)$$

$$\frac{a_2}{a_0} = c21 - c22 \cdot x - \frac{c23}{x} \qquad (4.21)$$

$$\frac{a_3}{a_0} = c31 - c32 \cdot x - \frac{c33}{x} \qquad (4.22)$$

Table 4.4 gives the values of the above parameters. The C values were substituted in eqs. 4.19 to 4.22 to generate a's which were then used in eq. 4.18 to give cross section at any energy and angle. This cross section value was then used in eq. 4.6 to yield a cross section value for $P + T \rightarrow {}^4He + \gamma$.

4.6 $|M|^2$ VERSUS t REPRESENTATION OF THE RESULT

A better way of looking at the result than the $\frac{d\sigma}{d\Omega}$ versus θ

TABLE 4.3

COEFFICIENTS OF THE POLYNOMIAL

E_γ (MeV)	a_0	a_1	a_2	a_3
300	5.30 ± 0.07	0.52 ± 0.32	-1.61 ± 0.27	0.90 ± 0.60
325	4.34 ± 0.04	0.83 ± 0.29	-1.43 ± 0.25	-02.0 ± 0.60
350	3.24 ± 0.04	0.75 ± 0.20	-0.94 ± 0.17	-0.20 ± 0.40
375	2.40 ± 0.05	0.61 ± 0.14	-0.94 ± 0.12	-0.70 ± 0.30
400	1.77 ± 0.03	0.35 ± 0.12	-0.38 ± 0.12	-0.30 ± 0.20
425	1.45 ± 0.02	0.36 ± 0.11	-0.38 ± 0.10	-0.20 ± 0.40
450	1.16 ± 0.02	0.30 ± 0.11	-0.26 ± 0.10	-0.10 ± 0.20
475	1.08 ± 0.02	0.18 ± 0.18	-0.41 ± 0.15	0.30 ± 0.40
500	0.93 ± 0.04	0.13 ± 0.27	-0.20 ± 0.34	0.40 ± 0.70
525	0.80 ± 0.03	0.33 ± 0.26	-0.09 ± 0.33	-0.10 ± 0.70
550	0.72 ± 0.02	0.14 ± 0.17	0.07 ± 0.49	0.40 ± 0.70
575	0.69 ± 0.02	0.11 ± 0.13	-0.43 ± 0.39	-0.10 ± 0.60
600	0.60 ± 0.02	0.34 ± 0.12	0.19 ± 0.62	0.30 ± 0.70
625	0.51 ± 0.02	0.60 ± 0.15	1.08 ± 0.74	0.90 ± 0.80

TABLE 4.4

'C' PARAMETERS OF EQUATIONS 4.17-4.20

C01	C02	C03	C04	C05	C06
132.25± 10.50	0.39 ± 0.01	6.23 ± 0.07	0.0040 ± 0.0002	247.25 ± 1.18	14853 ± 480

C11	C12	C13
0.6650 ± 0.0251	0.0029 ± 0.0002	$4.14 \times 10^{-6} \pm 4.10 \times 10^{-7}$

C21	C22	C23
0.150 ± 0.001	-0.1210 ± 0.0002	-0.1210 ± 0.0002

C31	C32	C33
-0.0943 ± 0.0038	-0.0002 ± 0.001	5.9048 ± 2.3613

representation is $|M|^2$ versus t representation, since the phase space factor is removed in the latter representation. $|M|^2$ is known as the invariant matrix element squared (Wil-71) which, for the reaction $\gamma + d \rightarrow P + n$ is:

$$|M|^2 = \left(\frac{8\pi}{\hbar c}\right)^2 (2S_\gamma + 1)(2S_\alpha + 1)\, S \left(\frac{P_\gamma}{P_p}\right) \frac{d\sigma}{d\Omega} \qquad (4.23)$$

where S_γ, S_α are the photon and α spin, S the square of C.M. energy, P_γ, P_P, $\frac{d\sigma}{d\Omega}$ are in the C.M. frame of reference. 't' is the square of the 4-momentum transfer. Fig. 4.5 gives such a representation of the result. It may be seen that 60°CM and 90°CM results do not fall on universal curve unlike the case of $\gamma + {}^3He \rightarrow P + d$ (Cou-83).

4.7 CONCLUSIONS

The angular distribution of the cross section at 246 MeV incident energy is plotted in Fig. 4.1 along with the data from BONN, MIT and SACLAY and the present work. The theoretical curves calculated from DWIA are also plotted. Curve A and curve B stand for the Correlated Gaussian wavefunction used for triton, A standing for the case without distortion and B with distortion. As may be seen, the distortion decreases the cross section by around 29%. This means that the distortion effects are of considerable importance. Since the distortion represents dominantly the absorption of the incoming proton, the cross section is reduced as expected, when distortion is included.

FIGURE 4.5

$|M|^2$ VERSUS t REPRESENTATION OF THE RESULT

REACTION: $\gamma + {}^4HE \rightarrow P + T$

■ θ_P^{CM}: 90°

▲ θ_P^{CM}: 60°

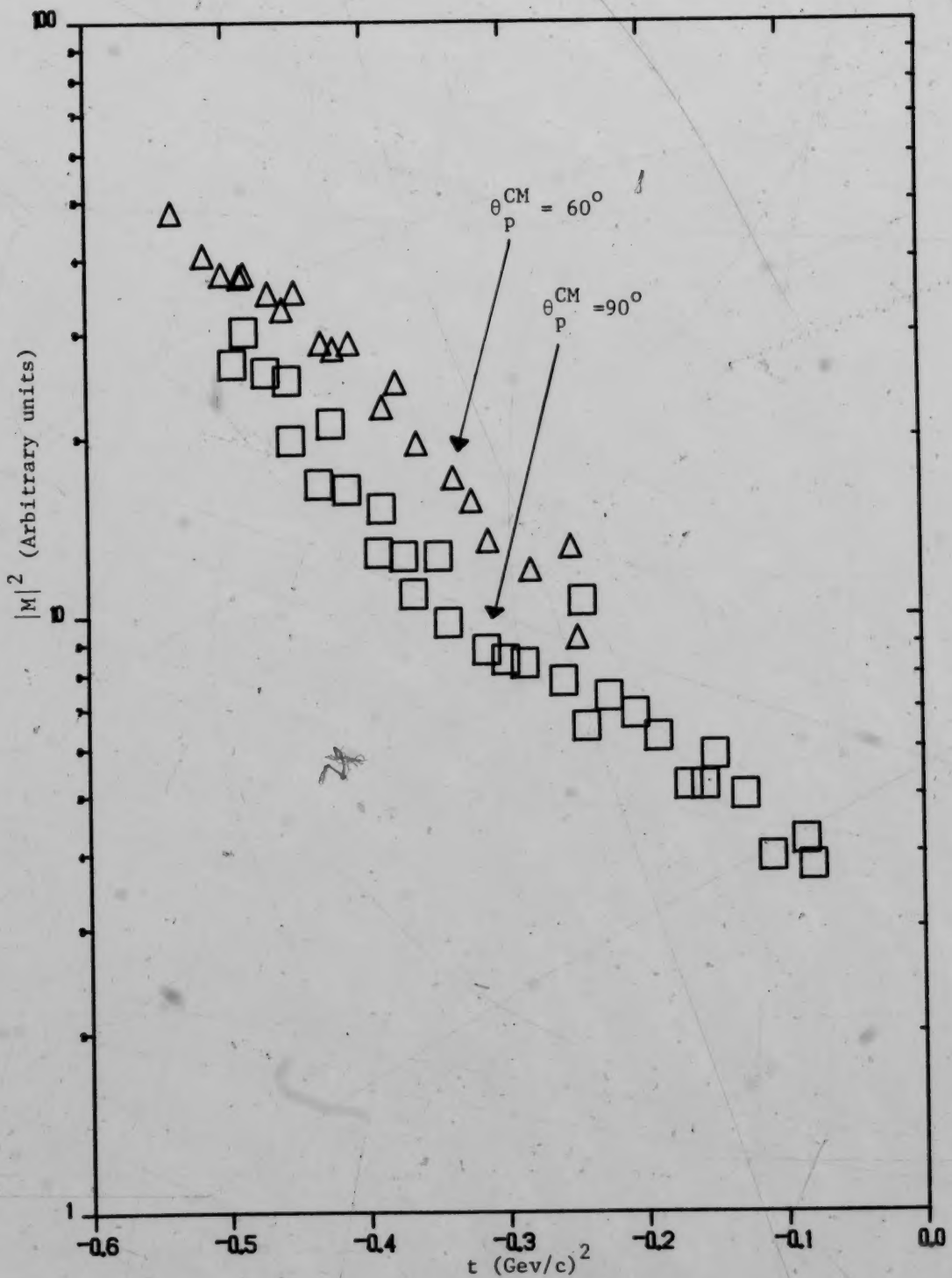
100
10
1
$|M|^2$ (Arbitrary units)
$\theta_p^{CM} = 60^o$
$\theta_p^{CM} = 90^o$
-0.6
-0.5
-0.4
-0.3
-0.2
-0.1
0.0
t (Gev/c)^2

All the curves reproduce the shape very well except at backward angles, which is characteristic of the model in situations like $p+d \rightarrow t+\pi^+$ (Fea-75) and $p+d \rightarrow {}^3He+\gamma$ (Cam-83). This could be because mechanisms involving more than two nucleons become important resulting in the reduced momentum transfer which results in the increased form factor and hence the increased cross section. Since the model is concerned at the primary mechanism $pn \rightarrow d\gamma$, thereby confining itself to the two-nucleon mechanism, it is natural that the theoretical prediction is lower than the experimental value. A typical situation is at 140° where the experimental value is 2.5 times that of the theoretical calculation.

It may be observed that the distortion introduces a normalization effect without changing the shape of the curve. Again this is characteristic of the model, observed in the situation of $p+d \rightarrow t+\pi^+$ also. This is understandable enough, since the distortion functions are evaluated at the origin and so distortion effect should be independent of the coordinates.

Curves C and D represent calculations using the correlated exponential wavefunction for the triton, C representing the case of no distortion and D the case with distortion. Curve C gives very good agreement with the experimental situation. One tends to conclude that the correlated exponential wavefunction gives the best representation of the triton.

Fig. 4.2 gives the experimental results for the excitation function at 60° and 90° C.M. angles. Plotted also are the data from

BONN, SACLAY, MIT, ILLINOIS and ORSAY. Fig. 4.2a gives the 60° excitation function along with the DWIA calculation results. Calculation was done using the correlated exponential wavefunction for the triton. It may be seen that the shape of the data is well imitated by theory except at large energies where the theory predicts values lower by a factor of 2 at a typical value of E_γ = 300 MeV. Again, this is characteristic of the theory illustrated in the case of $p+d \rightarrow t+\pi^+$. The multi-nucleon mechanism becomes important at high energies resulting in the increased form factor and the cross section. Since the theory does not take this into account, it is falling below the experimental value at high energies.

Fig. 4.2b represents the excitation function at 90° C.M. The fall-off at higher energies is sharper than compared to the 60° case. Theory underpredicts the cross section by a factor of 3 at 300 MeV, compared to a factor of of 2 at 60° C.M.

Fig. 4.3a gives the experimental value of the excitation function at 60° C.M. along with the curve representing the calculation in Gari and Hebach theory. Curve A represents calculation including the Δ effect. Curve B represents calculation excluding the Δ. Both the curves follow the shape well although predicted values are lower by a factor of 1.7 at 200 MeV. The Δ effect becomes important beyond 150 MeV. The theory underpredicts the cross-section by a factor of 1.3 at 200 MeV when the Δ effect is included. The agreement with the experiment becomes very good beyond 225 MeV when the Δ is included.

FIGURE 4.6

COMPARISON OF ANALYZING POWERS FOR THE REACTIONS

$pn \to d\gamma$, $pd \to {}^3He\,\gamma$ AND $pT \to \alpha\gamma$

x	$pn \to d\gamma$
Δ	$pd \to {}^3He\,\gamma$
$\square$	$pT \to \alpha\gamma$

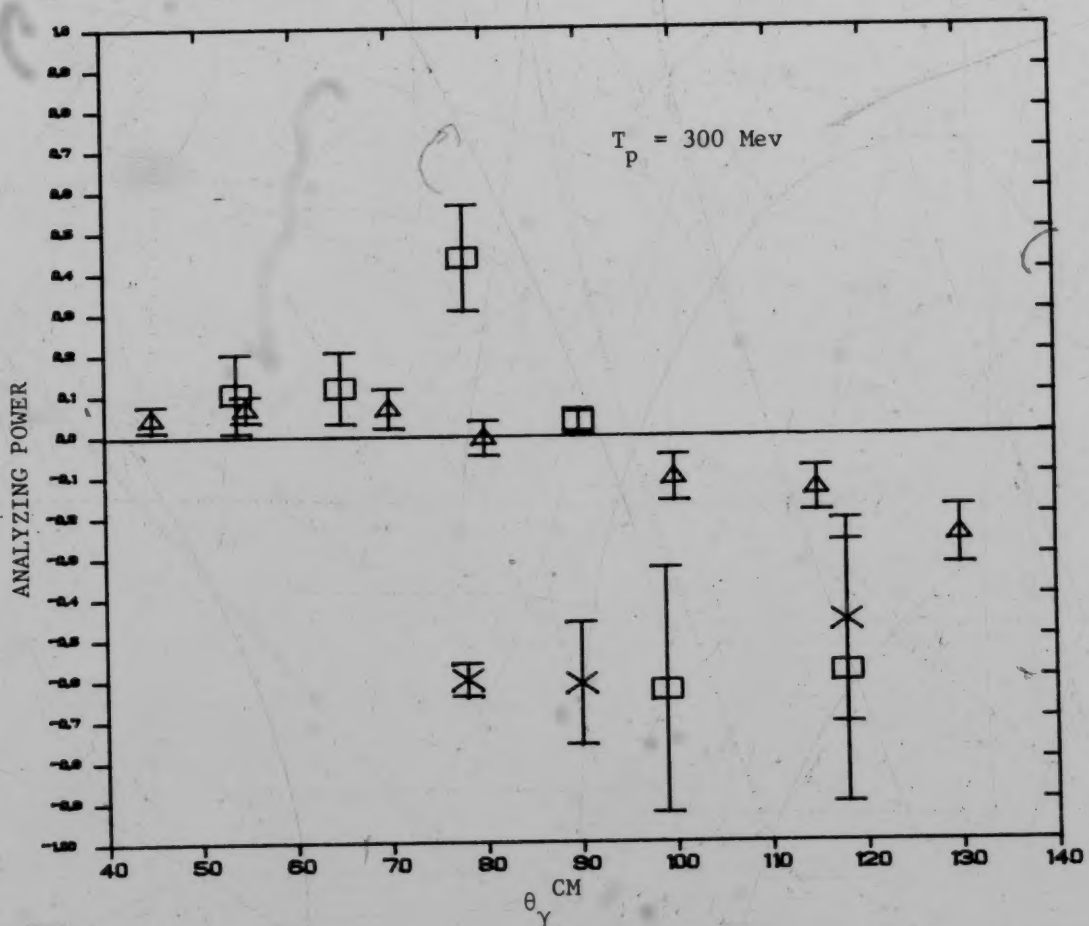
T_p = 300 Mev
ANALYZING POWER
40
50
60
70
80
90
100
110
120
130
140
θ_γ CM

A preliminary discussion of Time Reversal Invariance (TRI) was given in Chapter 1. We have, at our disposal a means to check the TRI by checking the principle of Detailed Balance (eqn. 1.62). As mentioned in Chapter 1, the comparison of the magnitude of the cross section and the shape of the angular distribution are two criteria to check TRI. This is because the ratio of the forward cross section to the backward cross section is given by a quantity independent of the scattering angle. Since both the criteria are satisfied, as may be seen when comparing the present data with the inverse reaction data, we see no evidence for the time reversal violation. As seen earlier, γ-N-N vertex, current conservation and hermiticity prevent and T violation in these interactions except in the Δ resonance region. The present measurements do cover the Δ-resonance region and thus do amount to an important check on TRI. A similar conclusion has been obtained by comparing the results of $P + d \rightarrow {}^3He + \gamma$ to the inverse reaction values (Cam-83). The results for the reaction $P + d \rightarrow {}^3He + \gamma$ mentioned in Appendix D are also consistent with the above claim.

Fig. 4.3 presents the analyzing power of the reaction $p + T \rightarrow \alpha + \gamma$ at $T_p = 300$ MeV as a function of the scattering angle. The positive values at small angles and negative values at large angles are reminiscent of the analyzing power for $pd \rightarrow {}^3He\,\gamma$ (Cam-83). The negative value of the analyzing power might thus be attributed to quasideuteron contributions.

Since the analyzing power involves the ratio of various amplitudes, it is not sensitive to the overall normalization, unlike

the case of differential cross-section.

Fig. 4.6 presents the analyzing power for the reactions p + T → α + γ at T_p = 300 MeV, compared to kinematically shifted analyzing powers for the reactions p + n → d + γ and p + d → ^{3}He + γ. The kinematic correspondence is found by involking the Impulse Approximation where the subprocess amplitude pn → dγ is equated to the free scattering amplitude pn → dγ by equating the momentum transfers as well as the centre of mass total energies (Fea-75).

The magnitude is found to be closest at forward angles to p + d → ^{3}He + γ and at backward angles to p + n → d + γ. The backward angles results however also agree with the p + d → ^{3}He γ result to within one standard deviation. It thus appears that the Impulse Approximation can account for not only the cross-section but also the analyzing power.

REFERENCES

Are-79 J. Arends et al., Nucl. Phys. **A322**, 253 (1979).

Are-84 J. Arends et al., Nucl. Phys. **A412**, 509 (1984).

Aren-82 H. Arenhovel, Czech. J. Phys. **32**, 155 (1982).

Arg-75 P.E. Argan et al, Nucl. Phys. **A237**, 447 (1975).

Bab-83 K. Baba et al., Phys. Rev. **C28**, 286 (1983).

Ber-65 J. Bernstein et al., Phys. Rev. **B139**, 1650 (1965).

Biz-80 J. Bizard et al., Nucl. Phys. **A338**, 451 (1980).

Bli-82 A.V. Blinov et al. Sov. J. Nucl. Phys. **35**,, 3, 301 (1982).

Blu-54 S.A. Bludman, Phys. Rev. **94**, 1722 (1954).

Cai-75 E.B. Cairns and W.K. Dawson, IEEE Transactions on Nuclear Science, **NS-22**, 308 (1975).

Cam-82 J.M. Cameron et al. Phys. Lett. **118**, 55 (1982).

Cam-83 J.M. Cameron et al., "Cross Section and Analyzing Powers for the Reaction pd → ^{3}He + γ at Intermediate Energies, Nucl. Phys. A (to be published).

Cha-56 O. Chamberlain et al., Phys. Rev. **192**, 1659 (1956).

Cha-72 G. Charpak et al., Nucl. Instr. and Meth. **99**, 279 (1972).

Chr-64 J.H. Christenson et al., Phys. Rev. Lett. **13**, 138 (1964).

Cou-83 P. Couvert, U.A./TRIUMF Workshop, Edmonton, 1983, TRIUMF Report TRI-83-3.

Cra-82 B.C. Craft III, M.I.T Doctoral Thesis, (1982).

Did-70 J.P. Didelez and H. Langevin-Joliot, IL Nuovo Cimento, **LXVII A**, 3, 388 (1970).

Don-71 B.L. Donnally, Proc. 3rd International Symposium on Polarization Phenomena in Nuclear Reactions, ed. H.H. Barschall and W. Haeberli (1971) 295.

Dou-76 P. Dougan et al. Z. Physik A276, 55 (1976)

Dri-79 H. Driller et al., Nucl. Phys. A317, 300 (1979).

Fea-74 H.W. Fearing, Phys. Lett. 52, 407 (1974).

Fea-75a H.W. Fearing, Phys. Rev. C11, 1210 (1975).

Fea-75b H.W Fearing, Santa Fe Conference on High Energy Physics and Nuclear Structure (1975).

Fea-77 H.W. Fearing, Phys. Rev. C16, 313 (1977).

Fin-76 Jan Finjord, Nucl. Phys. A274, 495 (1976).

Gar-81 M. Gari and H. Hebach, Phys. Rep. 72, 1 (1981).

Gim-79 J.L. Gimlett et al., Phys. Rev. Lett 42, 354 (1979).

Gre-79 L.G. Greeniaus et al., Nucl. Phys. A322, 308 (1979).

Ham-62 T. Hamada and I.D. Johnston, Nucl. Phys. 34, 382 (1962).

Hil-58 P. Hillman et al., Phys. Rev. 110, 1218 (1958).

Hua-60 C.F. Huang et al., Phys. Rev. 119, 352 (1960).

Hut-80 D.A. Hutcheon, Internal Report, 1980.

Hut-81 D.A. Hutcheon, TRIUMF Design Note TRI-DN-81-3 (1981).

Kie-73 S.E. Kiergan et al., Phys. Rev. C8, 2, 431 (1972).

Lag-75 J.M. Laget, Phys. Lett. B55, 37 (1975).

Lev-51 J.S. Levinger, Phys. Rev. 84, 43 (1951).

Lon-75 E. Longo and I. Sestili, Nucl. Instr. and Meth. 128, 283 (1975).

Lon-76 J.T. Londergan et al. Phys. Lett. 65, 427 (1976).

Lon-79 J.T. Londergan and G.D. Nixon, Phys. Rev. C19, 998 (1979).

Mil-83 C.A. Miller, U.A./TRIUMF Workshop, Edmonton, 1983, TRIUMF Report TRI-83-3.

Par-64 F. Partovi, Ann. of Phys. 27, 79 (1964).

Pic-70 P. Picozzo et al., Nucl. Phys. A157, 190 (1970).

Ram-81 N. Ramsey, Comm. Nucl. Part. Phys., 10, 22 (1981).

Rog-77 L.G. Rogers, TRIUMF Design Note TRI-DNA-77-5 (1977).

Rud-52 M. Ruderman, Phys. Rev., 87, 383, (1952).

Sat-58 G.R. Satchler, Nucl. Phys. 8, 65 (1958).

Sch-83 R.A. Schumacher et al., M.I.T. Doctoral Thesis (1983).

Sob-73 D.I. Sober et al., Nucl. Instr. and Meth. 108, 573 (1973).

Ste-80 A.W Stetz, "Cherenkov Counter Efficiencies", Internal Report, 1980.

Ste-81a A.W. Stetz, "KIOWA Histogramming and Plotting", Internal Report, 1981.

Ste-81b A.W. Stetz, TRIUMF Design Note TRI-DN-81-1 (1981).

Wal-66 N.S. Wall and P.R. Roos, Phys. Rev. 150, 811 (1966).

Wei-68 W.G. Weitkamp et al., Phys. Rev. 165, 1233 (1968).

Wil-71 W.S.C. Williams, "An Introduction to Elementary Particle", 2nd ed., (Academic Press, New York, 1971) 109.

Wol-52 J. Wolfenstein and L. Ashkin, Phys. Rev. 85, 947 (1952).

APPENDIX A

TARGET THICKNESS EVALUATION FROM P-T ELASTIC SCATTERING

A preliminary description of the target construction has already been given in Chapter 2.

The thickness was determined by elastically scattering protons from the TiT and Ti targets using the MRS spectrometer facility. The known cross-section values for P + T → P + T at E_p = 318 MeV (Bli-82) was used in determining the tritium content of the TiT target. Additional measurements, made at E_p = 500 MeV, were compared with the cross-section values extrapolated from the results of G. Bizard et al. (Biz-80).

A.1 THE MEDIUM RESOLUTION SPECTROMETER

This magnetic spectrometer consists of a dipole and quadrupole. The dipole field strength is such that the maximum momentum of the detected particle is 1.5 GeV/c. A dipole with a 60° bend angle follows a quadrupole which is preceded by a wire chamber and a scattering chamber, looking downstream. The wire chamber $X_o Y_o$ is of dimensions 5" x 5" with 64 wires in each plane. Beyond the exit of the dipole come two wire chambers, each of dimensions 10" x 40". The X plane has 512 wires and the Y plane has 128 wires. The bottom chamber is known as X_B-Y_B and the top chamber as X_T-Y_T. After these comes a 1" thick plastic scintillator. Wire spacing of any wire chamber is 2 mm.

The large angle configuration (LAC) of the MRS provides for

measurement at scattering angles of 20° and beyond. A small angle configuration (SAC) is achieved by pushing the quad 2 m from the target. In this configuration, measurements can be made from 20° to the left to 12° to the right. The solid angle acceptance of the MRS for angles above 15° is 2.5 msr. The corresponding number for angles less than 15° is 1.5 msr. The combined energy resolution of the cyclotron, the beam transport system, and the spectrometer was measured and found to be 900 keV FWHM at 400 MeV and 600 keV FWHM at 200 MeV. Details of the MRS may be found in (Ste-81, Mil-83).

A.2 THE EXPERIMENTAL PROCEDURE

The experiment was done at the T2 target station using the MRS. The proton beam of 318 MeV was used. The protons elastically scattered from titanium, copper and tritium were analyzed by the MRS. In addition we had to contend with the protons elastically scattered from carbon and hydrogen which constituted the kapton window for the target. Note that the target enclosure had two layers of 1 mil kapton window on either side. We could easily separate protons due to tritium from the rest of the protons by choosing the appropriate kinematical region (see Fig. A.1). The MRS was set at LAC mode and measurements were made at three scattering angles, θ_3 = 18.04°, 22.01° and 25.99°. We had one TiT run and one Ti run for θ_3^{ℓ} = 18.04°, five TiT runs and two Ti runs for θ_3^{ℓ} = 22.01°, three TiT runs and one Ti run for θ_3^{ℓ} = 25.99°. See Table A.1 for a run summary.

FIGURE A.1

ENERGY VERSUS ANGLE GRAPHS FOR PROTONS ELASTICALLY SCATTERED FROM

^{3}H, TI, AND CU

REACTION: $p + A \rightarrow p + A$

$T_p = 318$ MEV

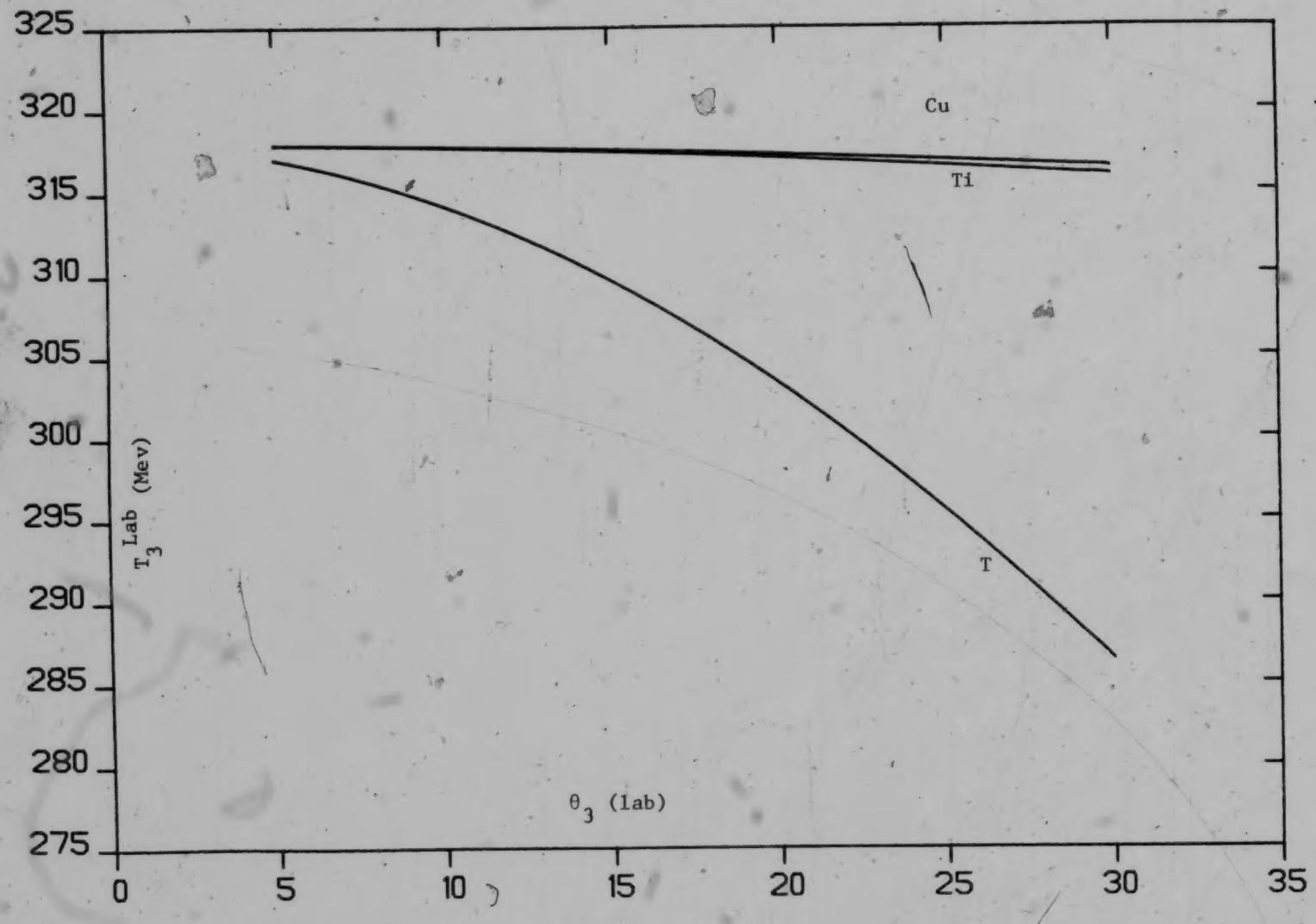
325
320
315
310
305
300
295
290
285
280
275
0
5
10
15
20
25
30
35
Cu
Ti
T
T_3^{Lab} (Mev)
θ_3 (lab)

A.3 THE MOMENTUM ANALYSIS

The focal plane position of the scattered particle is a function of its momentum. This meant that the different momentum groups of protons could be identified by their position in the focal plane. Focal plane position is given in terms of the wire numbers X_o, X_B and X_T, hit by the particle. If X_F stands for the focal plane position, we have:

$$X_F = \frac{359 \cdot X_T - 139 \cdot X_B}{X_T - X_B + 220} + 0.07\,(X_o - 28)^2 \qquad (A.1)$$

A kinematical correction depending upon the value of Y_o needed to be applied to this so that vertical bands corresponding to different momenta could be obtained while plotting Y_o versus the modified focal plane position (denoted by X_{FK}).

$$X_{FK} = X_F + BY_o \qquad (A.2)$$

where B depends upon the scattered proton momentum. Fig. A.2 gives a plot of Y_o versus X_{FK} where kinematical correction has been done for triton. Figures A.3, A.4 and A.5 give the one-dimensional plots for X_{FK} for scattering angles 18.04°, 22.01° and 25.99°. Fig. A.6 is the corresponding plot for the Ti run.

A.4 TARGET THICKNESS EVALUATION

A.4.1 The Solid Angle

The solid angle is determined by the window put on the $X\phi$-$Y\phi$

TABLE A.1

P-T ELASTIC SCATTERING DATA SUMMARY

The solid angle subtended by the X_o-Y_o plane is 1.4963 mstr.

RUN	TGT	ANGLE	CPROT	CMWOK	BUSGT	FCLCMC	MRSGT	POLR	POLL	POLRAC	POLLAC	CHNLL-CHNLH	COUNT
5	TiT	18.04	134294.	96486.	533313.	391820.	803121.	141553.	141311.	241.	282.	588.-616.	5448.
5	TiT	18.04	134294.	96486.	533313.	391820.	803121.	141553.	141311.	241.	282.	588.-616.	2349.
8	TiT	22.01	201730.	144967.	814754.	596712.	1491762.	444903.	445220.	1857.	2216.	624.-640.	5956.
9	TiT	22.01	156298.	111055.	430332.	265763.	391426.	240969.	240885.	856.	1104.	532.-552.	9867.
10	TiT	22.01	74648.	53229.	204186.	125893.	88406.	59054.	59532.	55.	76.	532.-552.	4653.
11	TiT	22.01	103248.	73340.	282732.	173991.	145187.	96649.	97769.	144.	184.	532.-552.	6468.
12	TiT	22.01	12736.	9021.	34879.	21474.	13820.	9001.	9133.	16.	27.	532.-552.	760.
13	Ti	22.01	91698.	65338.	248819.	152021.	118062.	85513.	85942.	286.	355.	532.-552.	3717.
14	Ti	22.01	88764.	63280.	240910.	147468.	102640.	74448.	74300.	53.	97.	532.-552.	3366.
21	TiT	25.99	459241.	328896.	1368877.	880498.	535161.	529493.	530969.	424.	618.	540.-556.	22244.
18	Ti	25.99	34072.	24230.	99627.	62928.	38994.	42000.	42389.	33.	46.	540.-556.	1011.

NOTE: BUSGT MEANS BUSY GATES.

FCLCMC MEANS FAST CLEARS TO CAMAC.

MRSGT MEANS MRS 5X ANDGATE OUTPUT FOR RUNS 1-8.

RHS AND MRS GATE OUTPUT FOR RUNS 9-21.

(NOTE THAT FOCAL PLANE PADDLE WAS IN TRIGGER FOR RUNS 9-21 ONLY AND HENCE MRS GATE OUTPUT TO BE ANDED WITH RHS FOR THESE RUNS).

CHNLL MEANS LOW CHANNEL CORRESPONDING TO TRITIUM PEAK.

CHNLH MEANS HIGH CHANNEL CORRESPONDING TO TRITIUM PEAK.

FIGURE A.2

YO VERSUS XFK SPECTRUM FOR ELASTICALLY SCATTERED PROTONS FROM TI, CU, C, ^{3}H AND ^{1}H

REACTION: p + A → p + A

T_p = 318 MEV

θ_p = 18.04°

TARGET: TiT

KINEMATICAL CORRECTION FOR ^{3}H

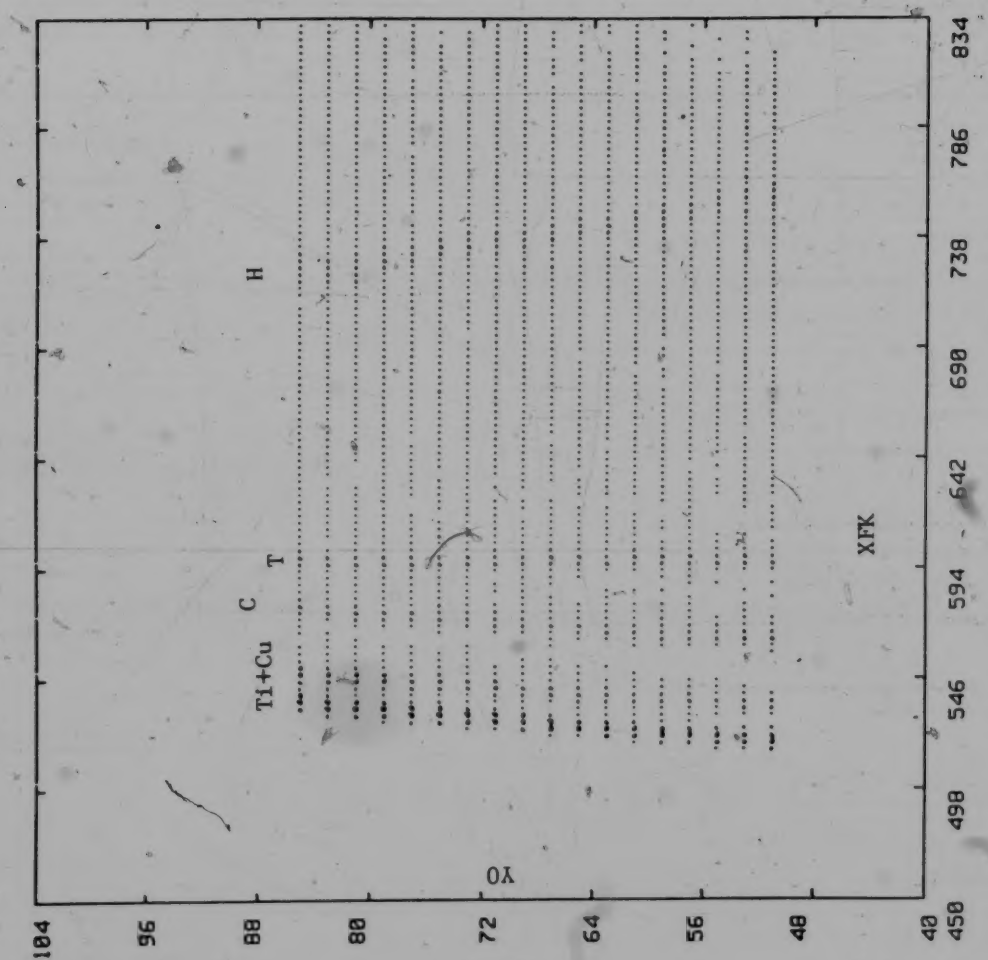
Ti+Cu C T H
YO
XFK
104
96
88
80
72
64
56
48
40
450
498
546
594
642
690
738
786
834

FIGURE A.3

XFK HISTOGRAM FOR ELASTICALLY SCATTERED PROTONS AT $\theta_p = 18.04°$

REACTION: $p + A \rightarrow p + A$

$T_p = 318$ MEV

$\theta_p = 18.04°$

TARGET: TiT

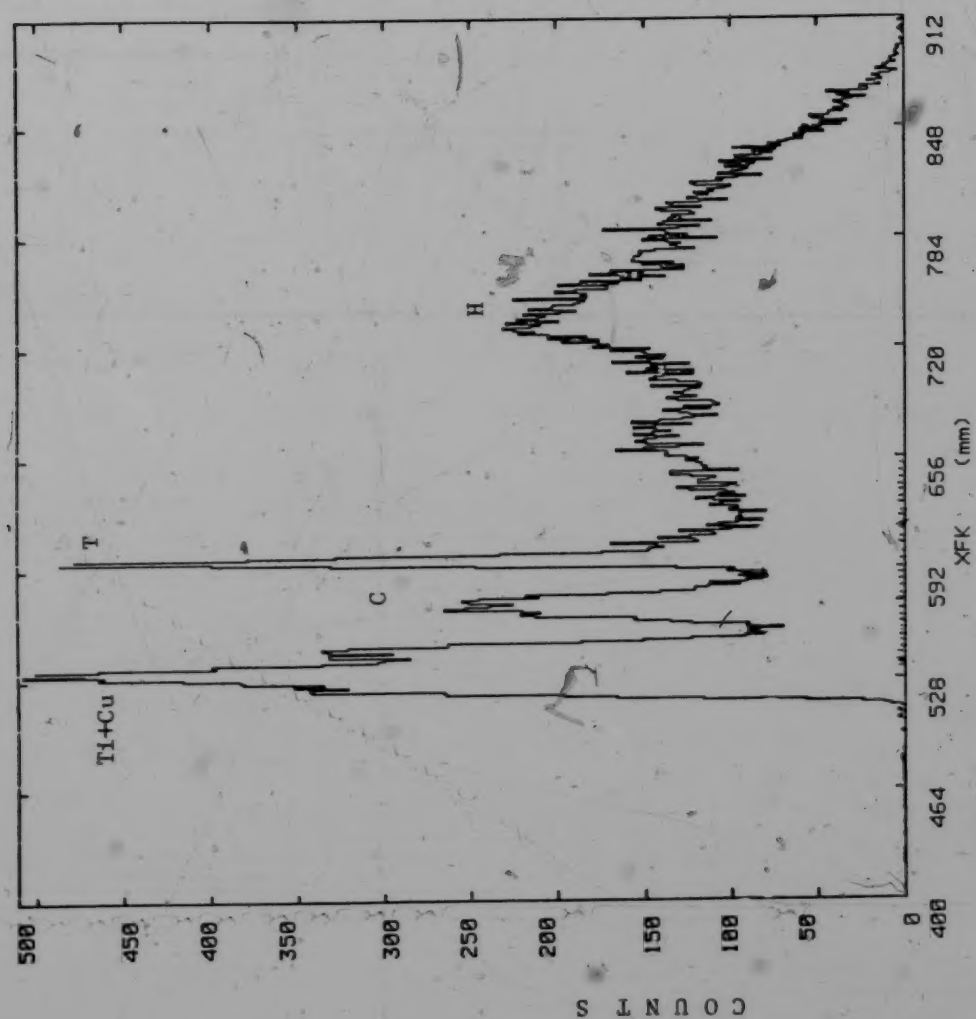
COUNTS
500
450
400
350
300
250
200
150
100
50
0
400
464
528
592
656
720
784
848
912
XFK (mm)
Ti+Cu
C
T
H

FIGURE A.4

XFK HISTOGRAM FOR ELASTICALLY SCATTERED PROTONS AT $\theta_p = 22.01°$

REACTION: $p + A \rightarrow p + A$

$T_p = 318$ MEV

$\theta_p = 22.01°$

TARGET: TiT

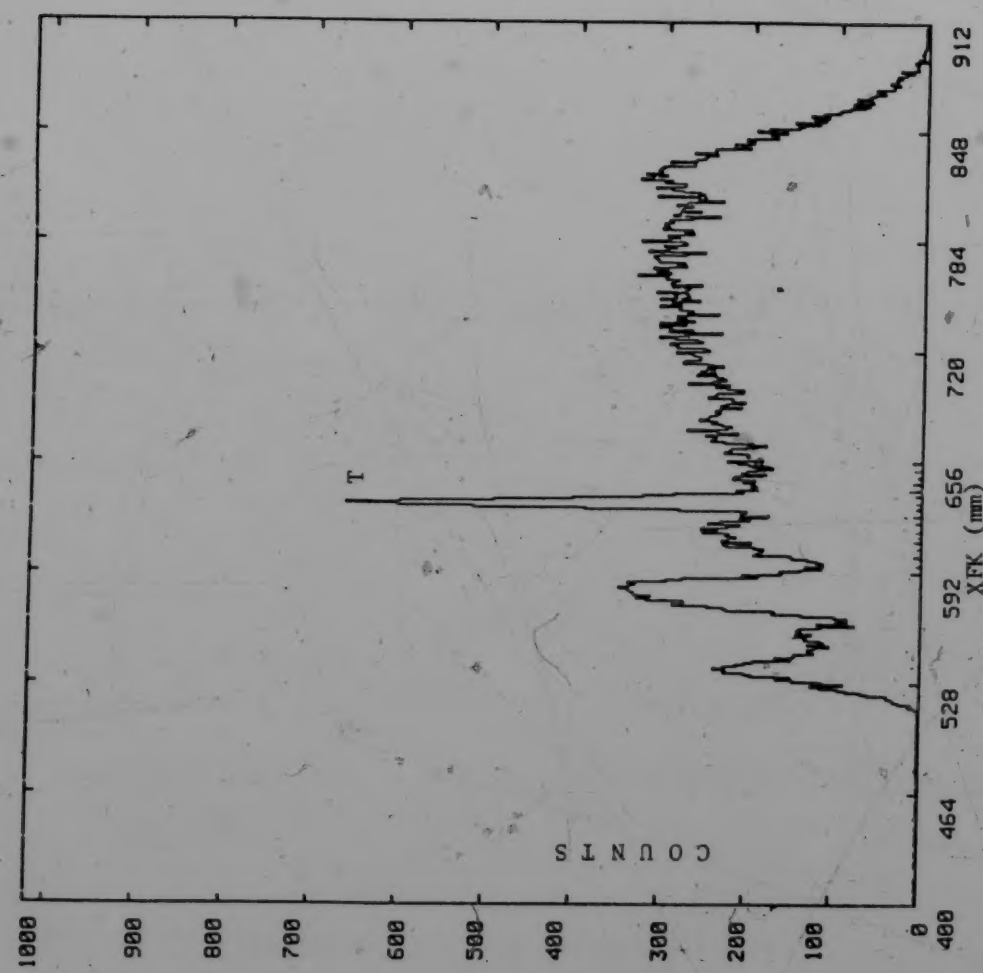
1000
900
800
700
600
500
400
300
200
100
0
COUNTS
T
400
464
528
592
656
720
784
848
912
XFK (mm)

FIGURE A.5

XFK HISTOGRAM FOR ELASTICALLY SCATTERED PROTONS AT $\theta_p = 25.99°$

REACTION: $p + A \rightarrow p + A$

$T_p = 318$ MEV

$\theta_p = 25.99°$

TARGET: TiT

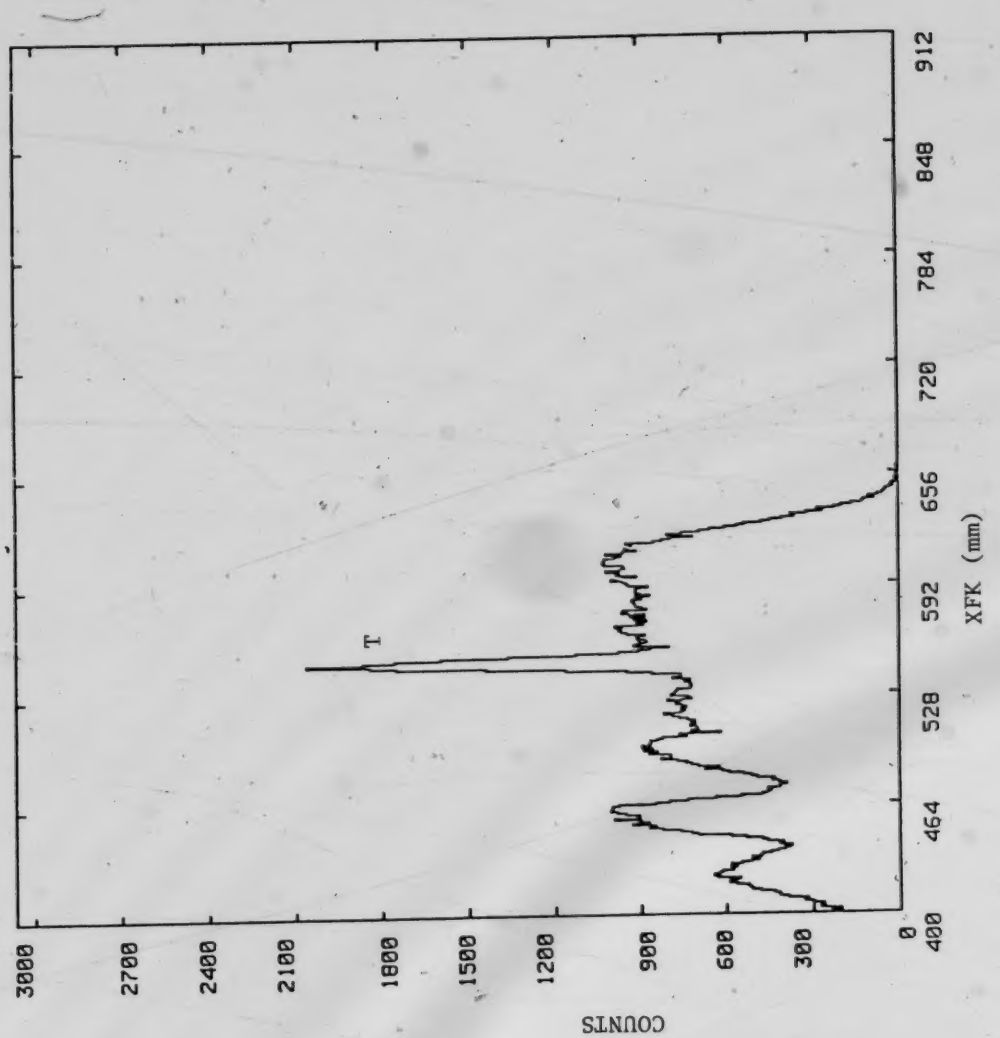
COUNTS
3000
2700
2400
2100
1800
1500
1200
900
600
300
0
400
464
528
592
656
720
784
848
912
XFK (mm)
T

FIGURE A.6

XFK HISTOGRAM FOR ELASTICALLY SCATTERED PROTONS FROM Ti TARGET

REACTION: $p + A \rightarrow p + A$

$T_p = 318$ MEV

$\theta_p = 18.04°$

TARGET: Ti

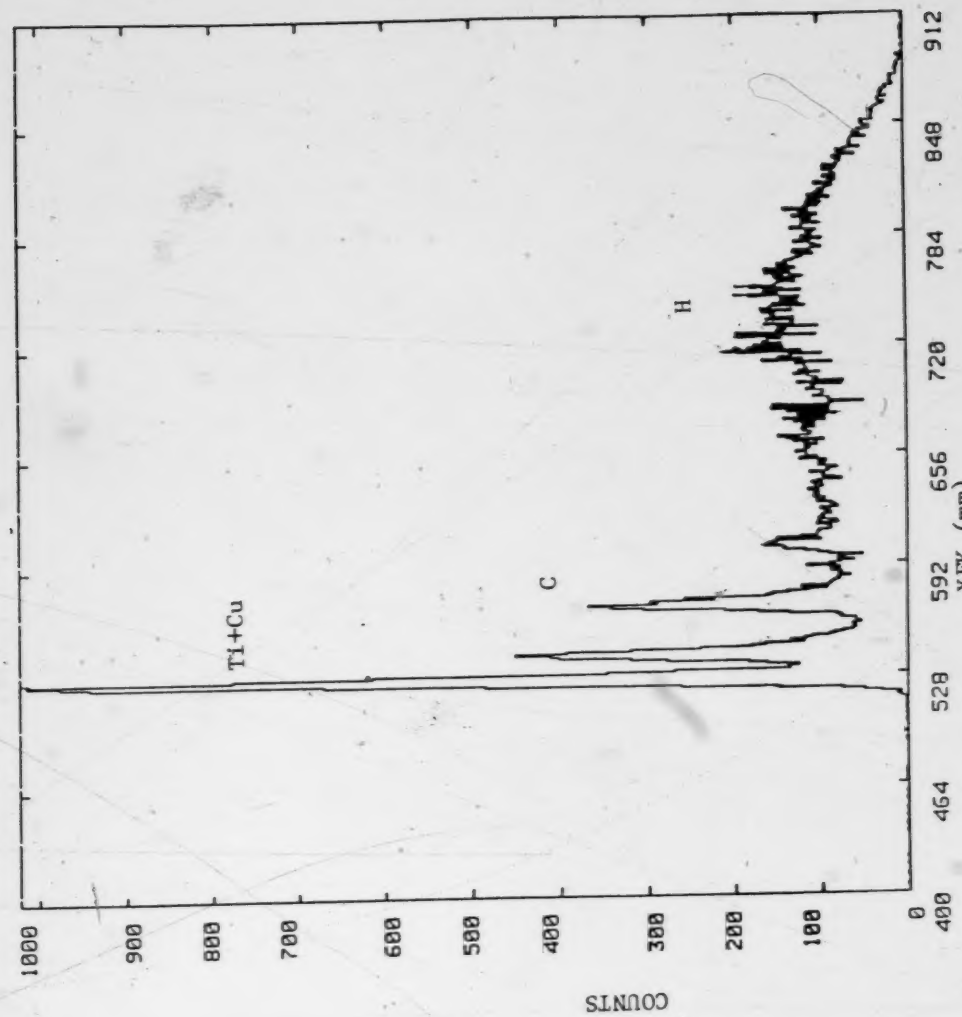
COUNTS
1000
900
800
700
600
500
400
300
200
100
0
400
464
528
592
656
720
784
848
912
XFK (mm)
Ti+Cu
C
H

plane. The window was such that 50 mm to 81 mm of the Xϕ plane and 50 mm to 86 mm of the Yϕ plane contributed to the solid angle. The Xϕ plane was situated at a distance of 85.09 cm and the Yϕ plane at a distance of 87.63 cm from the target. From geometry, the angle subtended by the relevant portions of the Yϕ plane is found to be 15.4045 mr. The corresponding quantity for the Xϕ plane is 25.6705 mr. These numbers yield a solid angle of 1.4963 mst. at the target.

A.4.2 The Wire Chamber Efficiency

The wire chamber efficiency remained relatively constant at around 71% throughout the experiment. If CMWOK stands for the wire chamber counts excluding the misses and multiples and if CPROT stands for the total counts, the wire chamber efficiency is given by:

$$M = \frac{\text{CMWOK}}{\text{CPROT}} \qquad \text{A.3}$$

A.4.3 The System Live-Time

L represents system live-time and was calculated using:

$$L = \frac{\text{Busy Gates - Fast clears to CAMAC}}{\text{MRS AND GATE OUTPUT}} \qquad \text{A.4}$$

For runs 1-8, the focal plane scintillator was not in trigger. From run 9 onwards, it was put in trigger in order to limit the

value of X_{FK}. This essentially simulated the right hand side electronics and so, we have another expression for system live-time.

$$L = \frac{\text{Busy Gates - Fast clears to CAMAC}}{\text{RHS AND MRS GATE OUTPUT}} \qquad \text{A.5}$$

The live-time varies from 14.62% for run 8 to 94.11% for run 18.

A.4.4 Beam Current

The total number of incident protons was determined by the polarimeter situated upstream from the Tl target. Refer to Chapter 3 for the beam current evaluation.

The target thickness, T is given by:

$$T = \frac{N_{net}}{P \cdot \frac{d\sigma}{d\Omega} \cdot S \cdot L \cdot M} \qquad \text{A.6}$$

where N_{net} is the number of events due to tritium alone, P the number of incident protons, $\frac{d\sigma}{d\Omega}$ the differential cross section for PT elastic scattering taken from Ref. Bli-82, S the solid angle, L the system live-time, and M the wire chamber efficiency.

$$N_{net} = N_{TiT} - N_B \qquad \text{A.7}$$

where:

$$N_B = \frac{N_{Ti} * P_{TiT}}{L_{Ti} * M_{Ti} * P_{Ti}} \qquad A.8$$

where N_{Ti} is the number of counts corresponding to the tritium region in the background run, P_{TiT} the number of incident protons for the tritium run, L_{Ti} the system live-time for the background run, M_{Ti} the wire chamber efficiency for the background run and P_{Ti} the number of incident protons for the background run.

The results are compiled in table A.2. The average thickness was evaluated with an uncertainty of 7%.

Tritium content in the target = 1.220 ± 0.084 mg/cm^2.

A.5 CORRECTION FOR THE RADIOACTIVE DECAY

The experiment $P + T \rightarrow \alpha + \gamma$ was done one year previous to the time when target thickness evaluation was done. This calls for a correction in the thickness to account for the radioactive decay of tritium. Tritium undergoes β decay with a half-life of 12.9 years. If N_0 stands for the tritium content at the time the experiment was done, we have:

$$N_0 = (1.220 \pm 0.084)\, e^{0.693/12.9}$$

$$\text{i.e. } N_0 = 1.287 \pm 0.088 \text{ mg/cm}^2.$$

TABLE A.2

THE TRITIUM CONTENT IN THE TiT TARGET

Scattering Angle (°)	Tritium Thickness (mg/cm^2)	Error in Thickness (mg/cm^2)
18.04°	1.314	0.119
22.01°	1.114	0.124
25.99°	1.260	0.382

The average thickness = 1.22 ± 0.084 mg/cm^2.

APPENDIX B

δ-RAYS

The head-on collision between a proton and an electron causes the electron to be ejected out of the atom, whereby the electron gets into the front detectors, simulating good events. These energetic electrons are known as δ-rays.

B.1 ENERGY OF δ-RAYS

A close collision between a proton and an atomic electron may be approximated as the collision between the proton and free electron. Fig. B.1 gives the lab frame situation of this collision.

Let m and m_e be the masses of the proton and electron respectively. P and P" represent the momentum of the proton before and after the collision. P' and E' are the momentum and kinetic energy of the electron after collision. P and P' make an angle θ. Conservation of momentum and total energy give the following equation for the electron kinetic energy:

$$E' = 2m_e c^2 \frac{P^2c^2 \cos^2\theta}{[m_e c^2 + (P^2c^2 + m^2c^4)^{1/2}] - P^2c^2 \cos^2\theta} \qquad (B.1.1)$$

A head-on collision means θ = 0 in which case the electron energy is maximum, E'_m.

FIGURE B.1

DIAGRAMATIC REPRESENTATION OF COLLISION BETWEEN PROTON AND ATOMIC ELECTRON IN THE LAB FRAME

P	PROTON MOMENTUM BEFORE COLLISION
P"	PROTON MOMENTUM AFTER COLLISION
P'	ELECTRON MOMENTUM AFTER COLLISION
θ	ANGLE BETWEEN INCOMING PROTON AND OUTGOING ELECTRON

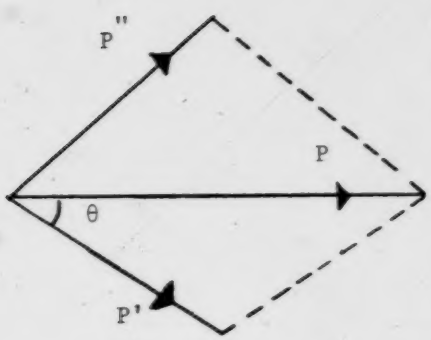
P"
P
θ
P'

$$E'_m = 2m_e c^2 \frac{p^2c^2}{[m_e c^2 + (p^2c^2 + m^2c^4)^{1/2}]^2 - p^2c^2} \qquad (B.1.2)$$

The front detectors in the experiment were kept at an angle of ~15° for 300 MeV incident protons, ~16° for 227 MeV protons and ~18° for 375 MeV protons. This means that the δ-rays that had to be tolerated in the absence of the magnet were of energies 0.7 MeV, 0.5 MeV and 0.8 MeV respectively.

Since $m \gg m_e$, eq. (B.1.1) reduced to the following form:

$$E' = \frac{2m_e c^2}{(\frac{\sec\theta}{\beta})^2 - 1} \qquad (B.1.3)$$

where $\beta = \frac{P}{E_{tot}}$, E_{tot} being the total energy of the proton. We also have:

$$E'_m = \frac{2m_e c^2 \beta^2}{1 - \beta^2} \qquad (B.1.4)$$

B.2 δ-PRODUCTION PROBABILITY

The generalization of the Rutherford formula to account for the fact that the electrons produced are relativistic, yields the cross section for δ-production. The Rutherford formula takes the force of interaction from the impact parameter, finds the momentum transferred from the force and the collision time, and then gets the

kinetic energy transferred to an electron from the momentum, assuming the non-relativistic case. Then it makes use of the probability of collision with the impact parameter being between b and b + db in the thickness dx gm cm^{-2} as follows:

$$F(b)db\ dx = 2\pi b\ db\ N \frac{Z}{A} dx \qquad (B.2.1)$$

where N is the Avogrado number, Z the atomic number and A the atomic mass number.

Since the energy transferred, E', is already obtained in terms of impact parameter, probability can be expressed in terms of E'.

$$\Phi(E')\ dE'\ dx = \frac{2B\ m_e c^2}{\beta^2} \frac{dE'}{(E')^2} dx \qquad (B.2.2)$$

This is the probability for the δ-ray of energy E' to be produced while the proton travels in the material a distance dx gm cm^{-2}. The factor B represents the total area covered by the electrons contained in one gm, each electron considered a sphere of radius r_e.

$$B = \pi N \frac{Z}{A} r_e^2 \qquad (B.2.3)$$

where $r_e = \frac{e^2}{m_e c^2}$, the classical electron radius, which equals 2.8 fm.

For the relativistic case, which is the situation in our case, eq. (B.2.2) generalizes to:

$$\Phi(E,E')\,dE' = \frac{2Bm_e c^2}{\beta^2}\,\frac{dE'}{(E')^2}\left[1 - \beta^2\frac{E'}{E'_m} + \frac{1}{2}\left(\frac{E'}{E+mc^2}\right)^2\right] \qquad (B.2.4)$$

where E' and E'_m are given by eqs. B.1.3 and B.1.4. Here B signifies the collision probability dependence on the electron density and $\frac{1}{\beta^2}$ gives the dependence of the energy transfer on the collision time.

Eq. B.2.4 may be rewritten in terms of the scattering angle θ. We get:

$$\Phi(E,\theta)\,d\theta = \frac{2B}{\beta^4}\,\frac{\sec^2\theta\tan\theta}{(\sec^2\theta-\beta^2)}\,(\sec^2\theta - 2\beta^2 + \beta^4)\,d\theta \qquad (B.2.5)$$

Integrating this over the angles spanned by the wire plane, it is found that the expected δ-rays flux for 300 MeV protons incident on the TiT target would be 5.6×10^5/s.

APPENDIX C

CHERENKOV COUNTER CALIBRATION AND EFFICIENCY DETERMINATION

The purpose of this experiment was to determine the efficiency of the Cherenkov counter for detecting positrons. The response of the counter for positrons of various energies was determined. These data on 'e' detection efficiency were then used in calculating the efficiency for detecting γ rays, knowing the correspondence between the γ energy and the e^+ or e^- energy from pair production and Compton scattering. This calculation of γ detection efficiency assumed that the 'e' detection efficiency is independent of its position in the detector. However, further calculations were then made to take into account the shower loss, e loss, or both from the knowledge of the detector geometry as well as the knowledge of the detector positioning with respect to the target. The distribution of the energies of e^+ and e^- for a particular γ was determined using a Monte-Carlo simulation program.

C.1 M20 STOPPED π/μ CHANNEL

The positron beam available at the M20 stopped π/μ channel of the TRIUMF Cyclotron Facility was used for the experiment. M20 is a 9 m long secondary channel available at the target station 1AT2. The TRIUMF Facility has two pion production target stations, 1AT1 and 1AT2, which are situated in beam line 1A. The target at 1AT2 was a 5 cm Be when the experiment was done. The π^+, generated at the target, decays at rest in the surface layer of the target, in

FIGURE C.1

ELECTRONICS SET-UP USED IN
CHERENKOV COUNTER CALIBRATION EXPERIMENT

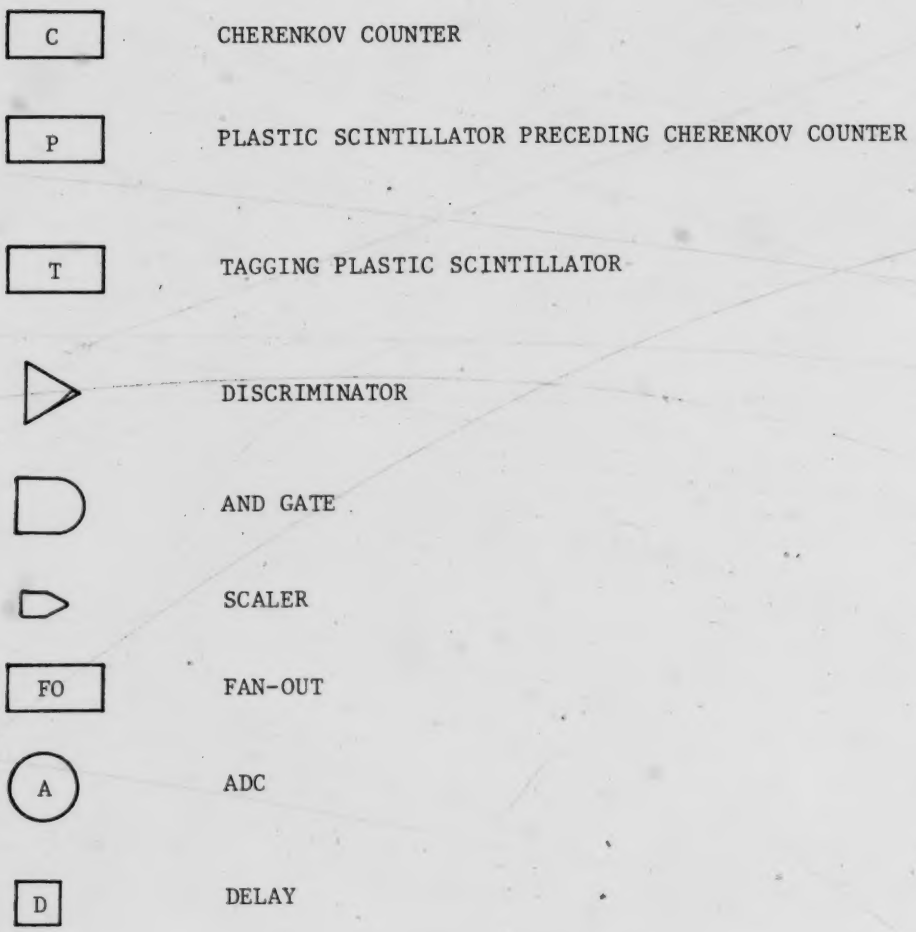

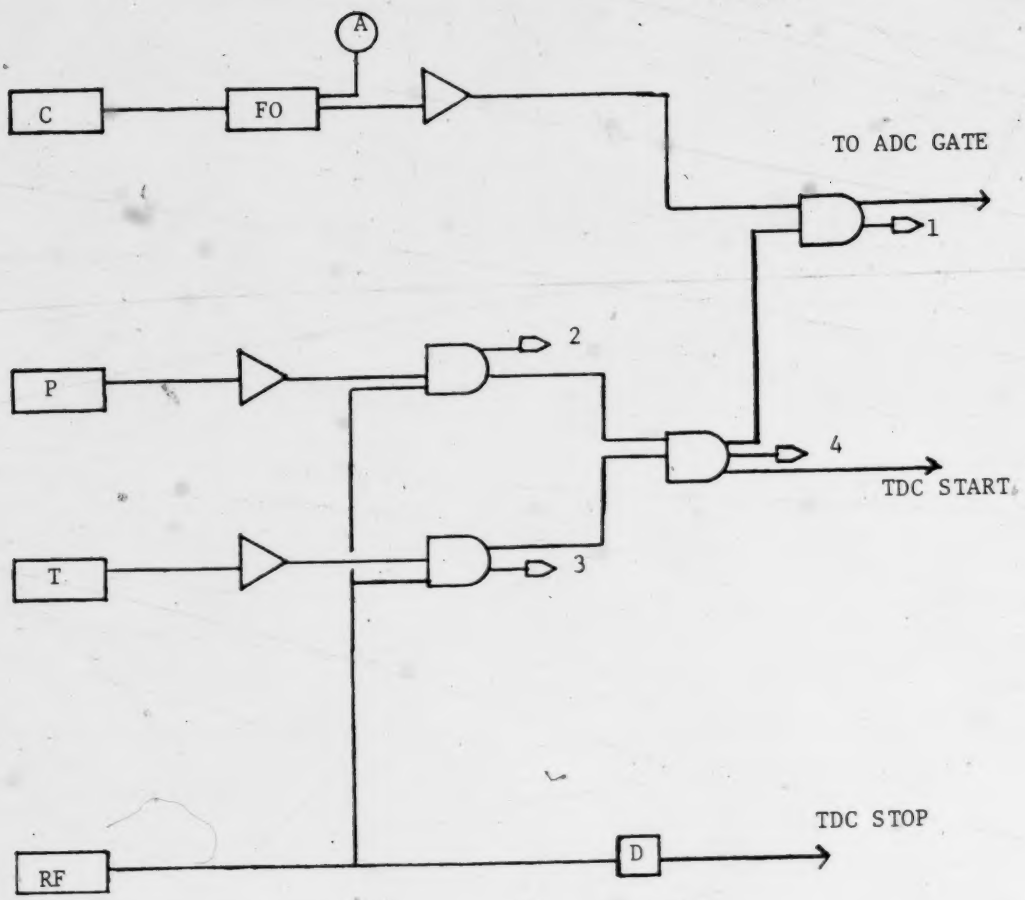
A
C
FO
TO ADC GATE
1
2
P
4
TDC START
T
3
TDC STOP
RF
D

the mode $\pi^+ \rightarrow \mu^+ \upsilon$. The produced μ^+ underwent decay in the mode $\mu^+ \rightarrow e^+ \upsilon\bar{\upsilon}$. Typical values of the fluxes of π^+, μ^+ and e^+ for a 1 μA proton beam of 500 MeV at 1AT2 are 10^6/s, 4×10^4/s and 5×10^5/s respectively. A set of dipoles and quadupoles provided momentum selection up to 17.5 MeV/c with a resolution of 5%. The Cherenkov counter detected π^+, μ^+ and e^+, but e^+ events were separated from the rest of the events by the TOF measured between the RF of the cyclotron and a counter in the beam. RF provided the timing required.

C.2 THE EXPERIMENTAL DETAILS

The purpose of the experiment was to find the efficiency of the Cherenkov counter for detecting e^+ of momenta varying from 12 MeV/c to 175 MeV/c. The response of the counter for e beam incident at various positions across the face of the detector was also measured. The latter measurement was necessary to get an idea of the shower loss at the edges of the counter.

Fig. C.1 gives the electronics used in the experiment. C represents the Cherenkov counter, 5" diameter x 7" long (corresponds to 7.5 radiadion lengths for lead glass), P is the plastic scintillator, 6" x 6", T is the tagging plastic scintillator, 1" x 1". Looking along the direction of the beam, C was preceded by P which was preceded by T. The distance between C and P was 1 1/2", that between P and T was 3". The level of the discriminator attached to C was adjusted using an attenuator in the anode circuit such that at 17 db attenuation, the count rate from an Americium

source noted by a rate meter (ORTEC 441) was half of the count rate at 0 db. This discriminator level was the one present during the $PT \rightarrow \alpha\gamma$ experiment. The ratio of SCALER 3 to SCALER 2 represented the beam focussing quality. The ratio of SCALER 1 and SCALER 4 represented the Cherenkov counter efficiency.

The experiment was performed at electron momenta 12, 15, 25, 37, 50, 100 and 175 MeV/c. The measurements were made with the beam incident at distances 0, 2, 4, 6 and 8 cm from the center of the Cherenkov counter face.

C.3 THE RESULTS

The central efficiency was 13% at 12 MeV/c (e^+ momentum) which increased rapidly to 56% at 15 MeV/c, 95% at 25 MeV/c and remained at 100% at and beyond 50 MeV/c. Positional response was such that for a 100 MeV/c e beam incident at 8 cm from the center, the efficiency was 45%; for 6 cm, 75%; for 4 cm, 91%; and for 1 cm, 100%. Fall-off of the efficiency with respect to distance from the center was more rapid for decreasing energy (Hut-80). An empirical expression for the Cherenkov counter efficiency as a function of e momentum was found to be (Ste-80)

$$E = 1 - e^{-m} \qquad \text{(C.3.1)}$$

where $m = 0.591 \left(\frac{P}{15}\right)^{3.871}$.

E is the efficiency; p the e momentum in MeV/c.

C.4 MONTE-CARLO CALCULATION FOR PHOTON DETECTION EFFICIENCY

The photon entering the lead glass triggers a long series of interactions resulting in a flux of electrons, positrons and photons, known as an electromagnetic cascade shower. It is easier to explain this phenomenon through a simulation program than mathematically, hence the need for a Monte-Carlo calculation.

Photon interactions with matter may be classified into three categories. The interaction of a photon with an atom as a whole leads to a photoelectric effect where the electron is knocked out of the atom. This means that the photon energy has to be at least the same as the electron binding energy. The interaction of the photon with a free electron leads to the Compton effect where most of the photon energy is handed over to the electron. The photon energy is reduced by the kinetic energy of the recoil electron. The interaction of the photon with the coulomb field of the nucleus is known as pair production where the photon disappears giving rise to an electron and positron. Obviously, the threshold condition is that the photon energy should exceed the sum of rest energies of the electron and positron. The excess energy appears as kinetic energy of the electron and positron. The recoil nucleus accounts for the momentum balance. At γ energies of interest to us (100's of MeV), only the Compton effect and pair production are important. Again, as the energy increases, the Compton effect becomes less important and pair production becomes more dominant.

The charged particles, ie. e^+ and e^- produced in the lead glass

by pair production as well as Compton scattered are ultrarelativistic. That is, they travel in the medium with a velocity greater than the velocity of light in the medium. This generates radiation along a conical wavefront known as Cherenkov radiation. The angle of emission of the radiation, θ, is given in terms of the refractive index of the medium 'n' and 'β' of the particle in the following way:

$$\cos \theta = \frac{1}{\beta n} \qquad \text{(C.4.1)}$$

For the lead glass which constituted the material of the Cherenkov counters, $n = 1.67$. The value of $\beta \simeq 1$ which gives $\theta \simeq 53°$.

The number of Cherenkov photons, N, emitted per unit length of the radiator is denoted by $\frac{dN}{dx}$.

$$\frac{dN}{dx} = \frac{2\pi\alpha Z^2}{c}\left(1 - \frac{1}{n^2\beta^2}\right) \qquad \text{(C.4.2)}$$

where α is the fine structure constant, 1/137, Z is the atomic number of the material through which the charged particle traverses.

The charged particle generated in the pair production process gets deflected in the coulomb field of the nucleus and hence experiences acceleration $\frac{Z}{M}$, where Z is the atomic number of the nucleus and M the electron mass. According to classical

electrodynamics, the resulting radiation, known as bremsstrahlung radiation, has an intensity proportional to $\frac{Z^2}{M^2}$. An electron of kinetic energy T generates a photon of any energy up to T.

In general, we have the following situation triggered by an incoming energetic photon in lead glass. It may either pair produce or Compton scatter. If pair production takes place, the generated e^+ and e^- produce bremsstrahlung photons which can start a new chain of interaction. If Compton scattering takes place, (i) the recoil electron will produce a photon by bremsstrahlung and (ii) the Compton scattered photon, if energetic enough, will start a new chain of interaction. The photon generated in process (i) can also trigger yet another chain of interactions. This results in an electromagnetic cascade shower, the flux depending upon the radiation length traversed. The Cherenkov light produced is proportional to the total path traversed by both e^+ and e^-, known as track length, which in turn is proportional to the energy of the primary photon. This means that the total Cherenkov light collected is proportional to the energy of the primary photon, provided, of course, that the entire shower is contained in the counter material.

A typical cascade simulation program will concern itself with things like the distribution of energies in the pair production, the distribution of energies of photon and electrons in the Compton scattering and bremsstrahlung, and assign these values arbitrarily from the interaction probabilities known from the energies of the

particles involved and the mass number and atomic number of the radiator material elements (Lon-75). Moreover, it will take into account the shower loss which is a function of the geometry, the term geometry standing for the shape and size of the radiator material as well as the positioning of the counter with respect to the target. The shower fluctuations from track length fluctuations generated by the geometry could cause poor resolution in the photon energy detected. Since at large shower depths, there are relatively large numbers of low energy electron, collision loss is more dominant than radiation loss. Multiple coulomb scattering of the electrons by atoms as well as the Compton process gives rise to lateral spread of the shower. The simulation program could also try to give an estimate of the lateral spreading.

The Monte Carlo simulation program, written to calculate the photon efficiency of the counters used in the experiment $PT \rightarrow \alpha\gamma$, is described in (Ste-80). This program is in the spirit of the calculations done by D.I. Sober (Sob-73). A brief explanation of (Sob-73) is warranted.

Sober takes pair production and Compton scattering as the interactions which the photon undergoes. The probabilities are summed over the lead, silicon and oxygen atoms in the lead glass. The detection probability of a photon of energy k having traversed a distance t is expressed as the product of probability of interaction and probability of detecting one or more 'e' produced in the interaction:

$$e_\gamma (k,t) = (1 - e^{-\mu(k)t}) \bar{E} (k,t) \qquad (C.4.3)$$

where the first factor is the probability that the photon has interacted in the counter before reaching 't'. The second factor is the average efficiency for detecting one or more electrons. This factor was obtained from the Monte-Carlo calculation with the following assumptions: (i) the electron detection efficiency is independent of its position within the counter, (ii) the position of interaction of the photon and distribution of final-state energies are assigned by the Monte-Carlo technique, (iii) the Compton scattered photon is allowed to propagate further provided the energy is greater than 2 MeV, and (iv) after a pair event, the shower is not propagated further. The efficiency of detecting the electron was taken from the electron calibration data.

The calculations described in (Ste-80) took the empirical expression C.3.1 for the electron detection efficiency. Again only Compton scattering and pair production were considered. An event was terminated at pair production. Compton scattering was followed up. The event was terminated if the secondary photon pair produced left the detector or attained the subthreshold energies.

As may be seen, the loss of the electrons and positrons were still to be accounted for. This was done in (Hu-80) where the track length traversed was calculated as a function of the solid angle subtended at the target by various annular regions of the Cherenkov

counter face. The radiation length to be traversed by the electron in order to produce enough light to be seen by the photomultiplier was calculated, taking into account the discriminator level, and the loss of electrons at the edges of the detector was estimated.

The results of the calculations after taking into account both the photon losses and electron losses are tabulated in Table C.1. Values of the efficiency for different γ energies and different detector distances are plotted in fig. C.2.

TABLE C.1

PHOTON DETECTION EFFICIENCY OF LEAD-GLASS CHERENKOV COUNTER

E_γ (MeV)	EFFICIENCY (%) AT THE DISTANCES (cm)		
	50	75	100
100	81	85	89
200	83	87	91
300	85	89	93
400	86	90	94

FIGURE C.2

CHRENKOV COUNTER EFICIENCIES AT VARIOUS COUNTER DISTANCES

AND VARIOUS γ ENERGIES

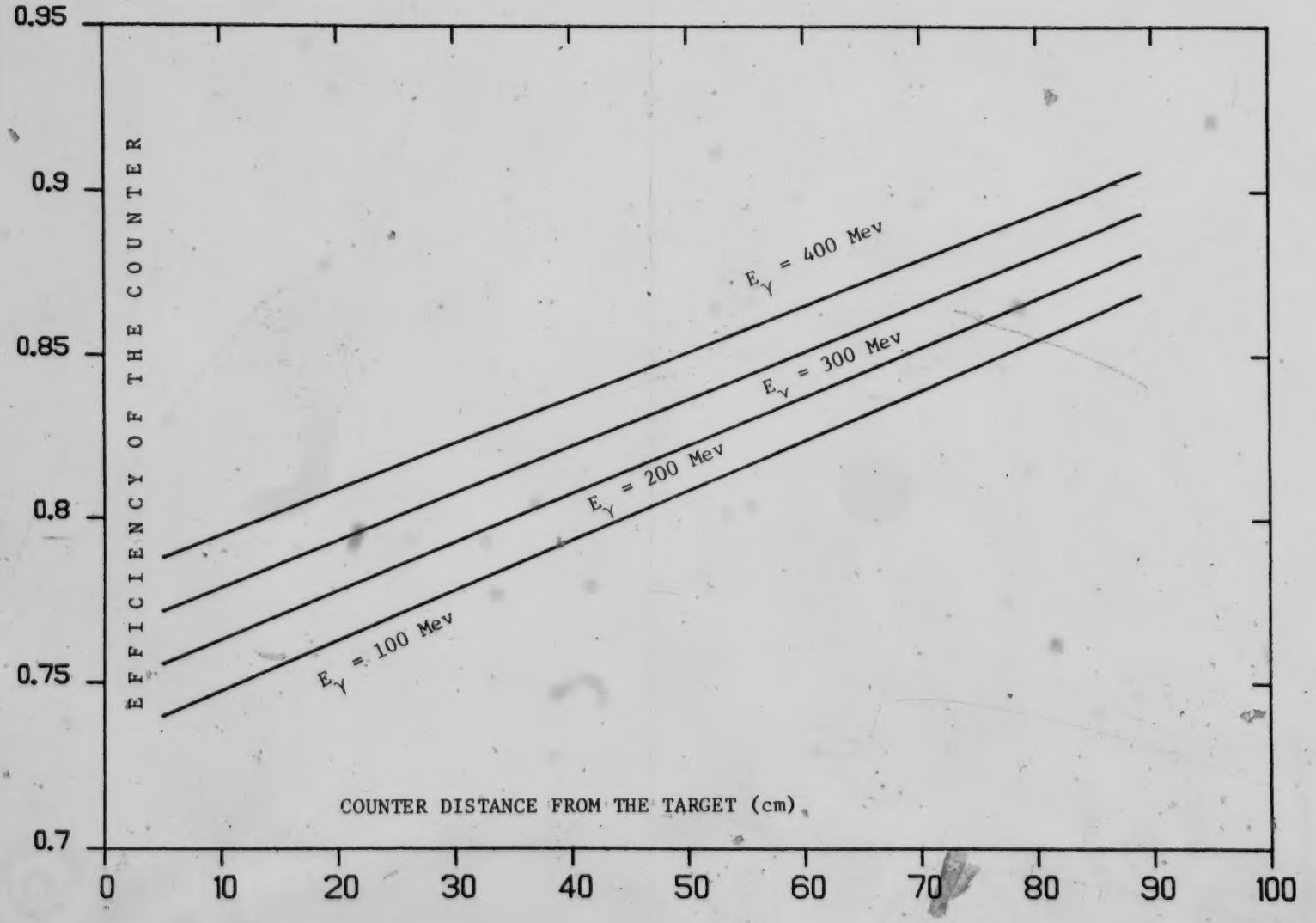
0.95
0.9
0.85
0.8
0.75
0.7
EFFICIENCY OF THE COUNTER
E_γ = 400 Mev
E_γ = 300 Mev
E_γ = 200 Mev
E_γ = 100 Mev
COUNTER DISTANCE FROM THE TARGET (cm)
0
10
20
30
40
50
60
70
80
90
100

APPENDIX D

STUDY OF THE REACTION $p + d \rightarrow {}^3He + \gamma$

The motivation for looking at this reaction is described in section 2.2. The reaction had been studied thoroughly earlier (Cam-82, Cam-83) and therefore provided a means to check the functioning of the experimental set up by measuring the cross section and comparing the result against the previously measured value. Furthermore, as mentioned in section 3.4.3, it provided a way to calculate the Cherenkov counter efficiency as a function of the pulse height cut, by providing a well-defined Cherenkov pulse height spectrum with good statistics.

D.1 THE EXPERIMENTAL SET-UP

The same experimental set-up was used as for $P + T \rightarrow \alpha + \gamma$ (Chapter 2). A deuterated polyethylene (CD_2) target of 75.3 mg/cm^2 thickness was used. The beam energy was maintained at 300 MeV. The recoil particle (^3He) detector assembly was situated at 14° on either side of the beamline. The distance was 45" from the target. This detector assembly identified ^3He's of energies 75 MeV, 100 MeV and 125 MeV. The γ-detectors (veto-Cherenkov counter assembly) were kept at angles 49°, 75° and 107° at distances of 24", 20" and 20" respectively from the target on either side of the beam line. These viewed γ's of energies 224 MeV, 199 MeV and 173 MeV. The above angles corresponded to θ_γ^{CM} = 62°, 90° and 120°. Distances were adjusted such that the Cherenkov counter image fell totally within

the wire planes, which meant that the solid angle was determined by the Cherenkov counter. The total collected charge was 36 μc. The differential cross section and the analyzing power were measured at the above three points.

D.2 THE DATA ANALYSIS

Data for this run did not need to be rewritten because there was no problem of ^{3}He stopping in the front plastic and so LEFT and RIGHT DCR tests were unambiguous. The analysis procedure was the same as described in Chapter 3. The Cherenkov efficiencies were about 88%, the wire chamber efficiency 72%, and the system live-time 76%. Fig. D.1 gives the plot of recoil particle energy versus recoil angle. The distinct peak due to (p,γ) may be seen. The carbon subtraction was done by describing a box (of the same size as for (p,γ) events) in the general background region of the spectrum and subtracting those counts from (p,γ) counts. A typical Cherenkov spectrum is shown in fig. 3.8.

D.3 THE RESULTS

The cross section and the analyzing power were determined for $\theta_\gamma^{CM} = 62°$ and $90°$. Part of the Cherenkov image for the angle $\theta_\gamma^{CM} = 120°$ fell outside the wire chamber frame and that point was omitted. However, analyzing powers were calculated for $\theta_\gamma = 120°$. Table D.1 gives the run summary. The cross section and the standard deviation were calculated using equations 3.5.9.3 and 3.6.1, where the variables were replaced by those for the CD_2 run. The analyzing power and the error were evaluated using equations 3.7.1 and 3.7.3.

FIGURE D.1

LOCUS SPECTRUM FOR THE REACTION $p + d \rightarrow {}^3He + \gamma$

$T_p = 300$ MEV

$\theta_\gamma^{CM} = 60°$

TARGET: CD_2

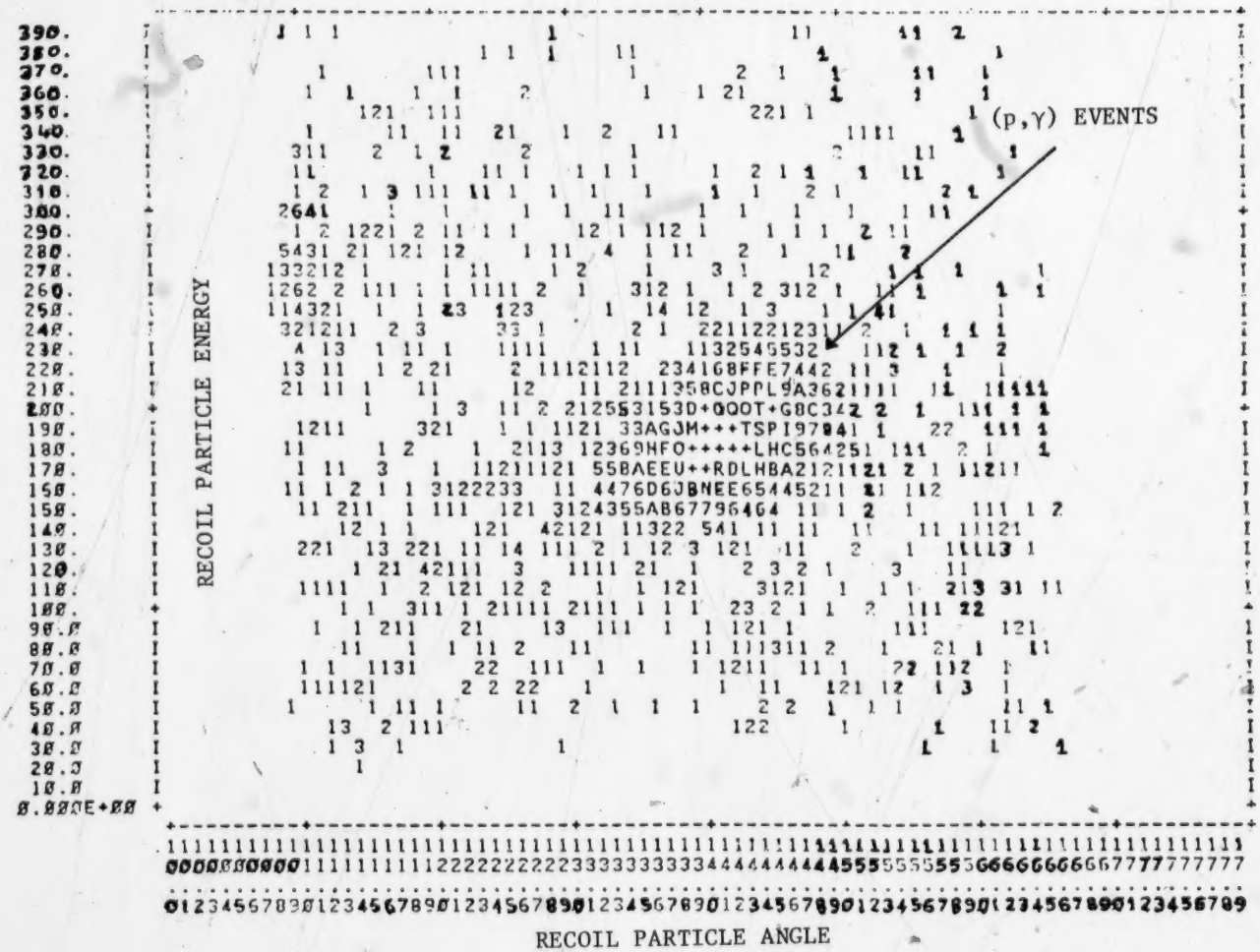
(p,γ) EVENTS
RECOIL PARTICLE ENERGY
390.
380.
370.
360.
350.
340.
330.
320.
310.
300.
290.
280.
270.
260.
250.
240.
230.
220.
210.
200.
190.
180.
170.
160.
150.
140.
130.
120.
110.
100.
90.0
80.0
70.0
60.0
50.0
40.0
30.0
20.0
10.0
0.000E+00
0123456789012345678901234567890123456789012345678901234567890123456789012345678901234567890
RECOIL PARTICLE ANGLE

TABLE D.1

P + d → ^{3}He + γ DATA SUMMARY, (P,γ) EVENTS

LEFT

L1 (θ_γ^{CM} = 62°)			L2 (θ_γ^{CM} = 90°)		
SPIN UP	SPIN DOWN	SPIN OFF	SPIN UP	SPIN DOWN	SPIN OFF
697 ± 26	792 ± 28	312 ± 18	634 ± 25	671 ± 26	263 ± 16

RIGHT

R1 (θ_γ^{CM} = 62°)			R2 (θ_γ^{CM} = 90°)		
SPIN UP	SPIN DOWN	SPIN OFF	SPIN UP	SPIN DOWN	SPIN OFF
779 ± 28	689 ± 26	270 ± 16	576 ± 24	581 ± 24	213 ± 15

Table D.2 summarizes results obtained after the accidentals subtraction. Fig. D.2 plots the cross section values along with the existing values (Cam-83). Fig. D.3 gives the plot of the analyzing power. The results (fig. D.2) may be seen to be consistent with the previously existing data.

FIGURE D.2

ANGULAR DISTRIBUTION OF THE CROSS SECTION FOR THE

REACTION $p + d \rightarrow {}^{3}He + \gamma$

TARGET: CD_2

T_p = 300 MEV

■ PRESENT WORK

▲ EXISTING VALUES (CAM-83)

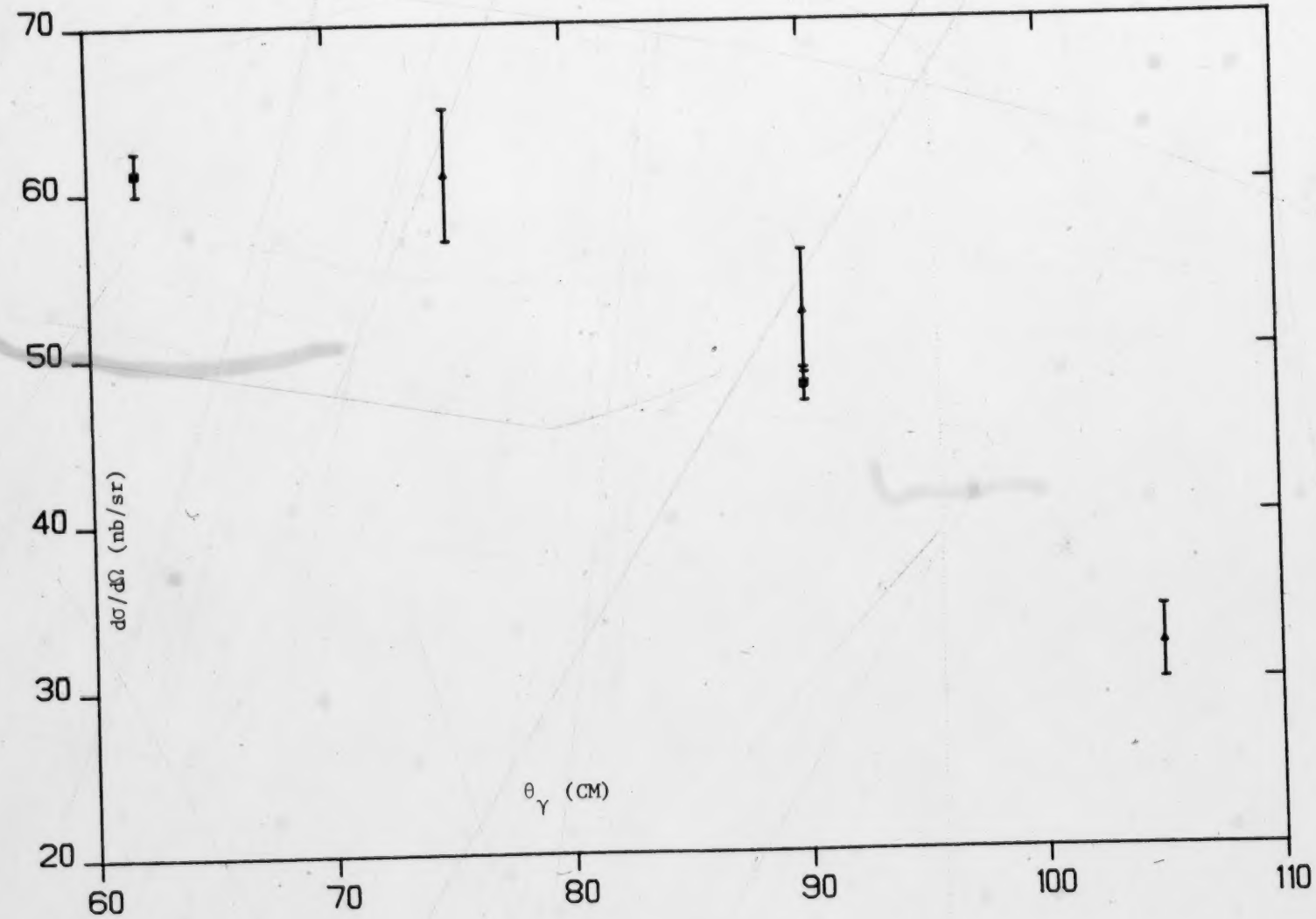
70
60
50
40
30
20
60
70
80
90
100
110
dσ/dΩ (nb/sr)
θγ (CM)

FIGURE D.3

ANGULAR DISTRIBUTION OF THE ANALYZING POWER FOR THE

REACTION $p + d \rightarrow {}^{3}He + \gamma$

TARGET: CD_2

T_p = 300 MEV

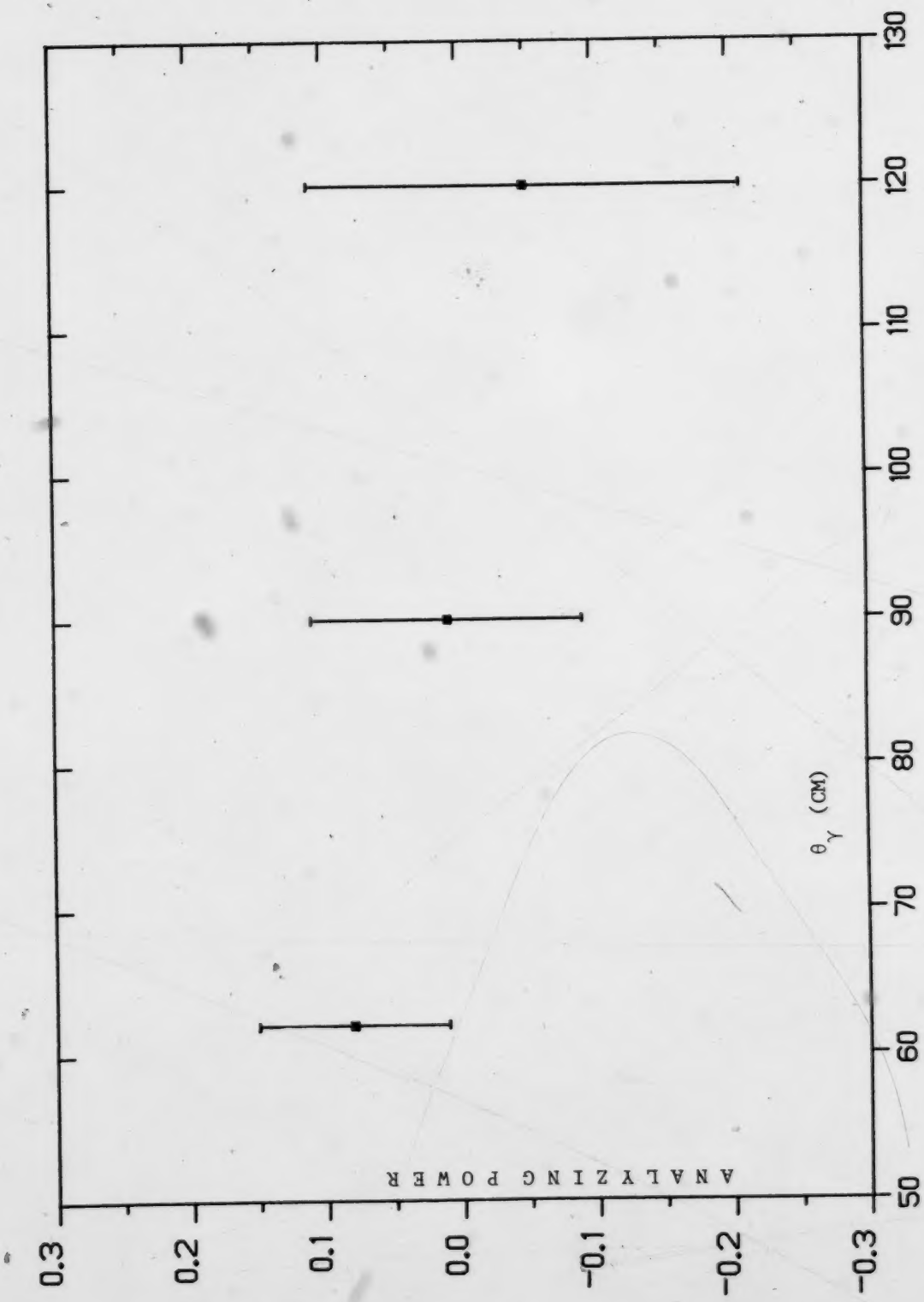
ANALYZING POWER
0.3
0.2
0.1
0.0
-0.1
-0.2
-0.3
50
60
70
80
90
100
110
120
130
θγ (CM)

TABLE D.2

CROSS SECTION AND ANALYZING POWER FOR THE REACTION P + d → ^{3}He + γ

AT T_p = 300 MeV.

θ_γ^{CM}	Cross Section (nb/sr)	Analyzing Power
62°	61.2 ± 1.3	0.08 ± 0.07
90°	48.0 ± 1.0	0.01 ± 0.10
120°	—	-0.05 ± 0.16